Master's thesis

NTNU
Norwegian University of Science and Technology
Faculty of Engineering
Department of Marine Technology

Kaushik Shiva Manjeri Ramakrishnan

Numerical Analysis of Mooring Systems for Floating Wind Turbines

Comparison of Concepts for South Korea

Master's thesis in Marine Technology
Supervisor: Adjunct Professor Kjell Larsen
June 2022

NTNU
Norwegian University of
Science and Technology

Kaushik Shiva Manjeri Ramakrishnan

Numerical Analysis of Mooring Systems for Floating Wind Turbines

Comparison of Concepts for South Korea

Master's thesis in Marine Technology
Supervisor: Adjunct Professor Kjell Larsen
June 2022

Norwegian University of Science and Technology
Faculty of Engineering
Department of Marine Technology

NTNU
Norwegian University of
Science and Technology

NTNU Trondheim
Norges teknisk-naturvitenskapelige universitet
Institutt for marin teknikk

MASTER THESIS SPRING 2022

for

Stud. tech. Kaushik Shiva Manjeri Ramakrishnan

Numerical Analysis of Mooring Systems for Floating Wind Turbines – comparison of concepts for South Korea

Numerisk analyse av forankringssystemer for flytende vindturbiner

Background

In recent years, the wind industry has seen a very fast development, moving from onshore to offshore, and from bottom-fixed shallow water to deep water floating solutions. Many of the floating wind turbine (FWT) concepts have been proposed for water depths larger than 100m. So far, the costs of energy for floating wind turbines is quite high as compared to bottom-fixed turbines, and they are significantly larger than onshore turbines. Therefore, the reduction of cost of the turbines is one of the main challenges for the floating wind turbines. An important contribution to the cost of FWTs is the mooring system.

During the recent development of FWTs for utilizing the offshore wind resource, various technologies from the offshore oil and gas industry have been adopted, including mooring system solutions. The purpose of the mooring system is to keep the floating wind turbine safely at a required position. Today, standard practice is that the mooring system of a single FWT consists of 3-9 mooring lines of chain, chain/steel wire rope or chain/synthetic rope. FWTs are considerably smaller than floating O&G structures. The external loads are characterized with large mean loads (due to the rotor thrust) in moderate wave conditions and high wave motions in extreme wave conditions. In deep water, the mooring system can be particularly expensive and novel solutions are needed.

The importance of the mooring system for a FWT is crucial. The moorings must be reliable enough to prevent any free drift where power cable rupture and collisions are typical consequences. The cost of mooring must be as low as possible to make such developments profitable. Design and optimization of the mooring system is therefore an important task.

The overall objective of this thesis is to perform a detailed assessment of the mooring system for a floating wind turbine. The work shall comprise a description of the status of floating wind turbines, an overview of rules and regulations and a deep dive into design methods and numerical analysis. Both state-of-art mooring systems and novel solutions shall be assessed and compared.

One of the frontrunners for piloting FWTs is South Korea. The site off the east coast of South Korea shall therefore serve as basis for the assessment.

Scope of Work

1) Review relevant literature regarding floating wind turbine concepts and mooring system design. This includes:
- Give a brief description of the status of floating wind turbines concepts.
- Describe different types of mooring systems in general and what types that could be attractive for floating wind turbines in particular. Focus on station keeping principles and main hardware components.

2) Give an overview of some of the design standards for floating wind turbines. Consider IEC 61400, DNV-ST-0437 and DNV-ST-0119. Based on the Design Load Cases (DLCs) given in the rules, propose and discuss relevant cases for ULS design of mooring systems for FWTs.

3) Describe the mooring design process and how numerical mooring analysis can be performed for a FWT. Environmental loads and FWT motions to be included. Different approaches using time-domain analysis methods shall be considered. Topics like how characteristic extreme values is estimated and models for mechanical behavior (tension-elongation) of synthetic ropes shall be described. Theory to be based on the SIMO/SIMA software suite and respective theory and user manuals and other sources. A separate section on aerodynamics shall also be included.

4) Further develop a SIMA model of a 12MW FWT; the 12MW “INO WINDMOOR” model. Describe the model and the different QA checks that is performed. Establish a “base case” mooring system based on chain only to comply with the design requirements outlined in task 2) and operating in South Korea (Donghae location) in 100m water depth.

5) Perform a numerical simulation comparison study of different mooring concepts and design methods. The numerical simulations shall focus on the use of both a coupled approach based on the use of SIMO and RIFLEX and checks using a quasi-static, un-coupled approach based on SIMO only. Propose, based on results from numerical analysis, alternative and novel mooring systems based on use of synthetic ropes. Such systems may also include clump weight components and buoys, often called “hybrid” solutions. The extent of this task shall be agreed with supervisor.

6) Conclusions and recommendations for further work.

General information

All necessary input data for the simulation case is assumed to be provided by NTNU/Equinor.
The work scope may prove to be larger than initially anticipated. Subject to approval from the supervisor, topics may be reduced in extent.
In the project, the candidate shall present his personal contribution to the resolution of problems within the scope of work.
Theories and conclusions should be based on mathematical derivations and/or logic reasoning identifying the various steps in the deduction.
The candidate should utilise the existing possibilities for obtaining relevant literature.

Report/Delivery
The project report should be organised in a rational manner to give a clear exposition of results, assessments, and conclusions. The text should be brief and to the point, with a clear language. Telegraphic language should be avoided.

The report shall be written in English and edited as a research report including literature survey, description of relevant mathematical models together with numerical simulation results, discussion, conclusions and proposal for further work. List of symbols and acronyms, references and (optional) appendices shall also be included. All figures, tables and equations shall be numerated.

The original contribution of the candidate and material taken from other sources shall be clearly defined. Work from other sources shall be properly referenced using an acknowledged referencing system.

Ownership
NTNU has according to the present rules the ownership of the project results. Any use of the project results has to be approved by NTNU (or external partner when this applies). The department has the right to use the results as if the work was carried out by a NTNU employee, if nothing else has been agreed in advance.

Thesis supervisor**:**
Adjunct Professor Kjell Larsen, NTNU/Equinor

Deadline: June 11th, 2022

Trondheim, January 28th, 2022

Kjell Larsen (sign)

Kaushik Shiva Manjeri Ramakrishnan (sign)

Preface

This master thesis was written as part of the requirements for a Master of Science in Marine Technology from the Department of Marine Technology at the Norwegian University of Science and Technology (NTNU) in Trondheim, Norway. This thesis was completed in the spring of 2022 as a continuation to the specialisation project completed in the autumn of 2021.

The aim of this thesis is to perform numerical analyses and evaluate various of mooring concepts for floating offshore wind turbines in the Donghae location, South Korea. The motivation to choose this topic for the master thesis is due to the relevance of floating wind turbines in the industry today. It is imperative that a thorough understanding of the mooring system of floating wind turbines is required to expand the horizon and make it feasible in deeper waters.

The reader is expected to have a basic understanding of marine hydrodynamics.

Trondheim, June 11, 2022

Kaushik Shiva

Kaushik Shiva Manjeri Ramakrishnan

Acknowledgements

Foremost, I would like to express my sincere gratitude to my supervisor Kjell Larsen for his encouragement, helpful insights and inspiration during this thesis. His enthusiasm for the subject has sparked my interest, and our discussions have given me valuable knowledge on the subject. Regular weekly meetings and guidance have been invaluable in keeping me on track during this thesis. Equinor is also acknowledged through Kjell Larsen for providing the metocean data for the Donghae location and the simulation set-up and procedure for the numerical analysis of fibre rope model in SIMA.

Besides my supervisor, I would like to thank Marit Kvittem and Petter Andreas Berthelsen of SINTEF Ocean for providing the WAMIT results of the INO WINDMOOR model. I would also like to thank Professor Erin Bachynski-Polić of the Department of Marine Technology, NTNU, for helping me with the TurbSim software. A special thanks is also given to PhD candidate Irene Rivera Arreba for her assistance with the SIMA software. I also would like to thank fellow student Mathias Tomren for our productive discussions during the work.

Finally, I would like to thank my fellow students at the Department of Marine Technology, as well as my friends and family, for their help and support throughout this master's program.

Abstract

The world is progressing rapidly towards sustainable forms of energy, and the share of electrical energy produced from wind will grow exponentially in the coming years. Subsequently, floating wind turbines are moving towards deeper water depths greater than 100 m. A significant challenge in deep water floating wind turbines is the increasing cost compared to bottom-fixed wind turbines. A vital contribution to the cost is that of the mooring system. Therefore novel solutions are required to design and optimise the mooring system to reduce its cost.

As a part of this thesis, different types of mooring systems for a floating wind turbine are studied. The design standards and various load cases relevant to the ultimate limit state design of the mooring system are also discussed.

A floating structure at sea is subjected to wind, wave, and current loads. These are discussed in detail with the equation of motion for a floating wind turbine. Different types of analysis performed on a mooring system are also discussed, emphasising the time-domain approach. Some dynamic instabilities observed in floating wind turbines are also discussed.

The INO WINDMOOR 12MW floating wind turbine with a semi-submersible substructure to be deployed at 100 m water depth off the coast of South Korea is analysed in this thesis. The analysis is carried out using the SIMA software package. The existing mooring system for the wind turbine designed by Inocean is replaced by a mooring system suitable for 100 m water depth with three mooring lines consisting of pure chain elements. A SIMO model with this mooring system serves as the base case system in this thesis. In addition to this, hybrid mooring systems such as Chain-Polyester-Chain system, Chain-Polyester-Chain system Clump Weights and Chain-Nylon-Chain systems are also analysed using a coupled SIMO-RIFLEX model to develop a cost-effective novel alternative for deep water mooring of floating wind turbine.

To document the model's behavior, identification tests such as constant wind tests, pull out and decay tests, and regular wave tests were performed. Furthermore, time-domain analysis was performed to ensure compliance with the ultimate limit state design for the various mooring concepts. According to the time-domain analysis, the hybrid mooring system shows great promise and can be used for floating offshore wind turbines. Finally, a summary of the thesis and suggestions for future research are provided.

Contents

Preface v

Acknowledgements vii

Abstract ix

List of Tables xix

List of Figures xxviii

Nomenclature xxix

1 Introduction 1

- 1.1 Background and Motivation 1
- 1.2 Scope of Work 4
  - 1.2.1 Approach 5
- 1.3 Structure of the Report 6

2 Mooring and Station keeping Systems for FWT 7

- 2.1 Floating Wind Turbines Concepts 7

2.2 Mooring and Station Keeping Systems 9
2.2.1 Components of a Mooring System 9
2.2.2 Mooring Systems for FWT 12
2.2.3 Review of Mooring System for Pilot Parks 13
2.3 Station Keeping Principles 14
2.3.1 Geometric Stiffness 16
2.3.2 Elastic Stiffness 18
2.3.3 System Restoring Force 19
2.4 Static Equilibrium of Mooring Lines 21
2.4.1 Solutions of Inelastic Cable Line (Catenary) Equations . . 22
2.4.2 Line Characteristics with Line elasticity included 23
2.5 Synthetic Ropes 24
2.5.1 Axial Stiffness of Synthetic Ropes 24
2.5.2 Procedure for Estimating total tension 28

3 Design Standards and Regulations 29
3.1 Rules and Standards for a Floating Wind Turbine 29
3.1.1 IEC 61400 29
3.1.2 DNV Standard 30
3.2 Design Requirements for Mooring Lines 30
3.2.1 Limit States 30
3.2.2 ULS and ALS Design Criteria 30
3.2.3 Discussion on Design Load Cases for ULS Design 32
3.3 Fatigue Design 34
3.4 Design Requirements for Anchors 35

4 Theoretical Background 37

4.1 Forces and Motion 37
  4.1.1 Equation of Motion 37
4.2 Excitation Forces 38
  4.2.1 Wave Loads 38
  4.2.2 Wind Loads 41
  4.2.3 Current Loads 48
4.3 Dynamic Instabilities in an FWT 49

5 SIMA Software and Theory **53**

5.1 SIMA Software Package 53
5.2 SIMO 53
  5.2.1 Solution by Convolution Integral 54
  5.2.2 Separation of Motions 54
5.3 RIFLEX 56
5.4 Coupled and Uncoupled Analysis 57
5.5 Estimation of Extreme Response from Time Domain Simulations . 58

6 12MW Floating Wind Turbine Model **61**

6.1 Modelling of FWT in SIMA 61
6.2 Description of INO WINDMOOR Floating Substructure 62
  6.2.1 Coordinate System 63
  6.2.2 Main Particulars 63
  6.2.3 Mass Matrix 64
  6.2.4 Infinite Frequency Added Mass Matrix 65
  6.2.5 Linear Damping Matrix 65
  6.2.6 Hydrostatic Stiffness 65
  6.2.7 Force Transfer Functions 65

6.2.8 Motion Transfer Functions 67
6.2.9 Slender Elements 67
6.2.10 Mooring System 69
6.2.11 Coupled SIMO-RIFLEX Model 70

7 Mooring Concepts 73
7.1 Pure Chain System 73
7.2 Chain - Polyester - Chain System 75
7.2.1 Non-Linear Stiffness model for Polyester Mooring Line . 76
7.3 Chain - Polyester - Chain System with Clump Weights 77
7.4 Chain - Nylon - Chain System 78
7.4.1 Non-Linear Stiffness model for Nylon Mooring Line . . . 80
7.5 Summary of Mooring Concepts 82

8 Numerical Simulations 83
8.1 Identification Tests 83
8.1.1 Constant Wind Test 83
8.1.2 Decay Test 85
8.1.3 Regular Wave Test 86
8.2 Convergence Study 87
8.3 Design Load Cases for Mooring System 88
8.3.1 Environmental Conditions 88
8.3.2 Environmental Condition for DLC 1.1 90
8.3.3 Environmental Condition for DLC 1.6 91
8.3.4 Environmental Condition for DLC 6.1 91

9 Results and Discussion 93
9.1 Constant Wind Test 93

9.2 Decay Test 94
9.2.1 Pure Chain System in SIMO 94
9.2.2 Pure Chain System in SIMO-RIFLEX 95
9.2.3 Chain - Polyester - Chain System 97
9.2.4 Chain - Polyester - Chain System with Clump Weight . . . 98
9.2.5 Chain - Nylon - Chain System 99
9.3 Pull Out Test 99
9.4 Regular Wave Test 101
9.5 Convergence Study 104
9.6 Time Domain Analysis 107
9.6.1 Base Case Mooring System in SIMO 107
9.6.2 Comparison of Base Case Mooring System in SIMO and SIMO-RIFLEX Coupled Model 116
9.6.3 Comparison Study of Various Mooring Concepts 118

10 Conclusion and Recommendations for Future Work **129**
10.1 Summary and Conclusion 129
10.2 Recommendations for Future Work 131

Appendices **137**

A First-Order Wave Force Transfer Functions **139**

B Response Amplitude Operators **143**

C Comparison of Constant Wind Test from SIMA and OpenFAST **147**

D Decay Test Plots **149**

E Results for DLC 6.1.1 in In-between Collinear Condition **153**

F Results for DLC 1.6 **155**

G Results for DLC 1.1 **159**

List of Tables

1.1 Pros and Cons of Offshore Wind Turbine compared to Onshore [1] 3

2.1 The typical natural time period in different DoF for an FWT . . . 15
2.2 Parameters used for Static elastic stiffness [2] 26
2.3 Parameters used for Dynamic elastic stiffness [2] 27

3.1 Load factor requirements for the design of mooring lines [3] . . . 32
3.2 Design load cases for station keeping system [4] 33
3.3 DFF for mooring chain [3] 35
3.4 Material factors for different types of anchors [3] 36

6.1 Main Particulars for INO WINDMOOR FWT [5] 64
6.2 Mass properties for Semi and Tower from SIMO model 64
6.3 Fairlead and Anchor Coordinates of existing Mooring System [5] . 69
6.4 FWT rigid-body natural periods [5] 69

7.1 Constant Parameters for all concepts 73
7.2 Properties of Mooring Chain 75
7.3 Properties of Mooring Chain and Polyester Segments 76

7.4 Properties of Mooring Chain and Nylon Segments 80
7.5 Summary of all mooring concepts 82

8.1 SIMA settings for constant wind test 84
8.2 SIMA settings for decay test 85
8.3 Simulation parameters for decay test 86
8.4 SIMA settings for regular wave test 87
8.5 Simulation parameters for regular wave test 87
8.6 SIMA settings for convergence test 88
8.7 Simulation parameters for convergence test 88
8.8 Environmental parameters for DLC 1.1 91
8.9 Environmental parameters for DLC 1.6 91
8.10 Environmental parameters for DLC 6.1 92

9.1 Calculated rigid-body time periods for all mooring concepts . . . 95
9.2 Mean offset, MPM and standard deviation in Surge, Heave and Pitch for Base Case Mooring System 108
9.3 Line tension for ML 1 in base case mooring system 113
9.4 ULS check of windward line for DLC 6.1.1 in-line collinear condition for all mooring concepts 123

E.1 ULS check of leeward line for DLC 6.1.1 in-between collinear condition for all mooring concepts 153

F.1 ULS check of windward line for DLC 1.6 in-line collinear condition for all mooring concepts 157
F.2 ULS check of leeward line for DLC 1.6 in-between collinear condition for all mooring concepts 157

G.1 ULS check of windward line for DLC 1.1 in-line collinear condition for all mooring concepts 161

G.2 ULS check of leeward line for DLC 1.1 in-between collinear condition for all mooring concepts 161

List of Figures

1.1 World grid-connected electricity generation by power station type [6] . . . 1

1.2 Proposed floating wind farms pilot parks in Europe [7] . . . 2

1.3 Water depth in various regions . . . 3

1.4 Cost break-up for typical bottom-fixed turbines and FWT [8] . . . 4

2.1 Common floater types for FWT [3] . . . 8

2.2 Platform designs under development stages toward commercial scale [9] . . . 8

2.3 Main Mooring Line Components [10] . . . 9

2.4 Stud-link and Studless Chain [10] . . . 10

2.5 Steel Wire Rope [10] . . . 10

2.6 Synthetic Fibre Rope [10] . . . 11

2.7 Anchor Types . . . 11

2.8 Buoy [11] . . . 12

2.9 Clump Weights [11] . . . 12

2.10 Typical Arrangement of Mooring Systems . . . 13

2.11 Mooring layout and types used for FWTs [8] . . . 13

2.12 The average number of moorings per turbine [8] 14
2.13 Rigid body motion modes for an FWT [3] 15
2.14 Excitation Time Scales [10] 16
2.15 Geometric Stiffness of Catenary System 17
2.16 Elastic Stiffness of a Taut system 18
2.17 Total Restoring Stiffness 19
2.18 System restoring force due to both windward and leeward lines [10] 20
2.19 Spread Mooring Arrangement 20
2.20 Mooring system restoring forces [10] 21
2.21 A 2D mooring line with forces acting on it [10] 21
2.22 Illustration of notations defining line characteristics [10] 23
2.23 A synthetic rope segment under tension 24
2.24 A typical tension strain curve 25
2.25 Principle tension-strain curves observed and adapted from testing [2] 25
2.26 Static Stiffness (Working Curve) for polyester and nylon ropes . . 27
2.27 Linearised Dynamic Stiffness for polyester and nylon ropes 28

3.1 Variation of wind force on an FWT w.r.t the wind velocity at the hub 33
3.2 Variation of significant wave height w.r.t the wind velocity at the hub 34

4.1 Environmental loads acting on an FWT [11] 38
4.2 Wave body interaction problem [12] 39
4.3 Vertical Wind Shear [1] 42
4.4 Wind speed spectrum over a broad range of frequencies [1] 42
4.5 Components of Wind Velocity [10] 43
4.6 One-dimensional actuator disk rotor model [13] 44
4.7 Velocity and forces acting on an airfoil cross-section [13] 46

4.8 Mean wind speed v/s thrust force for INO WINDMOOR turbine . 47
4.9 Bird's eye view of the FWT with wind force acting on it 50
4.10 Principle curve showing moments acting on the FWT 50
4.11 Moment due to motion and thrust force 52

5.1 Program modules in SIMO [14] 53
5.2 Retardation function Surge-Surge from INO WINDMOOR model 55
5.3 Program modules in RIFLEX [15] 56
5.4 Separated Analysis [16] 57
5.5 Coupled Analysis [16] 58
5.6 Illustration of Peak and Maxima Distribution [17] 59

6.1 Concept of WINDMOOR 12 MW FWT [5] 62
6.2 Coordinate System [5] 63
6.3 First-order wave force transfer function in Surge, Heave and Pitch 66
6.4 Wave drift force in Surge 66
6.5 RAOs in Surge, Heave and Pitch at the waterplane for 0° wave heading 67
6.6 Rectangle with thin splitter plate - Case 2 in Table E-1 [18] 68
6.7 Ellipse - Case 14 in Table E-1 [18] 68
6.8 SIMO model with base case mooring system 70
6.9 Modelling Slender System in RIFLEX [15] 71
6.10 Coupled SIMO-RIFLEX model with base case mooring system . . 71

7.1 Top view of a typical mooring system in SIMO-RIFLEX Coupled model 74
7.2 Static configuration of ML 1 in X-Z plane for Pure Chain System . 75
7.3 Static configuration of ML 1 in X-Z plane for CPC System 76
7.4 Working curve for polyester line with MBL 23544 kN 77

7.5 Static configuration of ML 1 in X-Z plane for CPC System with Clump Weight . . . 78

7.6 Extrapolation of rope diameter for required MBL . . . 79

7.7 Extrapolation of weight per unit for calculated rope diameter . . . 79

7.8 Static configuration of ML 1 in X-Z plane for CNC System . . . 80

7.9 Working curve for nylon line with MBL 16000 kN . . . 81

7.10 Comparison of working curves for polyester and nylon mooring lines 81

8.1 Comparison of RPM of the INO WINDMOOR turbine at 4 m/s and 12 m/s . . . 84

8.2 Example of decay force with ramp force and constant force in Surge 85

8.3 Collinear Environment . . . 89

8.4 Non-Collinear (or) Spread Environment . . . 90

8.5 Contour lines of H_s and T_p for representative of the 1, 10, 50 and 500-year return periods for omni-directional waves at Donghae Location [19] . . . 92

9.1 Results from constant wind test . . . 93

9.2 Decay test result from SIMO model for pure chain system [20] . . . 95

9.3 Decay test result from SIMO-RIFLEX coupled model for pure chain system . . . 96

9.4 Decay test result from SIMO-RIFLEX coupled model for the CPC system . . . 97

9.5 Decay test result from SIMO-RIFLEX coupled model for the CPC system with Clump weight . . . 98

9.6 Decay test result from SIMO-RIFLEX coupled model for the CNC system . . . 99

9.7 Pull out test result for in-line direction . . . 100

9.8 Pull out test result for in-between direction . . . 100

9.9 Surge RAO Comparison for $\beta = 180°$ . . . 102

9.10 Heave RAO Comparison for $\beta = 180°$ 102

9.11 Pitch RAO Comparison for $\beta = 180°$ 103

9.12 Sway RAO Comparison for $\beta = 90°$ 103

9.13 Roll RAO Comparison for $\beta = 90°$ 104

9.14 Yaw RAO Comparison for $\beta = 90°$ 104

9.15 DLC 1.6 Extreme value distribution of various number of seeds . . 105

9.16 DLC 1.6 Convergence plot of MPM value 106

9.17 DLC 6.1 Extreme value distribution of various number of seeds . . 106

9.18 DLC 6.1 Convergence plot of MPM value 107

9.19 Comparison of surge time series for base case mooring system in DLC 1.1 and 1.6 in-line collinear case 109

9.20 Comparison of power spectra in surge for base case mooring system in DLC 1.1 and 1.6 in-line collinear case 109

9.21 Power spectrum for heave in DLC 1.1 in-line collinear case 110

9.22 Comparison of power spectra in surge for base case mooring system in DLC 1.1 and 6.1.1 in-line collinear case 111

9.23 Power spectra in heave for base case mooring system in DLC 6.1.1 in-line collinear case 111

9.24 Yaw time series for DLC 6.1.1 Inline Collinear Case 112

9.25 Time series of line tension of windward line for DLC 6.1.1 base case mooring system 114

9.26 Power spectrum of line tension of windward line for DLC 6.1.1 base case mooring system 115

9.27 Time series of line tension for DLC 6.1.1 base case mooring system 115

9.28 Comparison of mean offset and MPM for surge, heave and pitch in SIMO and SIMO-RIFLEX Coupled model 116

9.29 Comparison of line tension for SIMO and SIMO-RIFLEX Coupled model 117

9.30 Line tension vs Offset in SIMO and SIMO-RIFLEX Coupled model 117

9.31 Comparison of platform motions for all mooring concepts 118

9.32 Power spectra of heave for all mooring systems 119

9.33 Time series of surge for CPC and CNC systems 120

9.34 Power spectra of surge for CPC and CNC systems 120

9.35 Power spectra of surge for CPC system with and without clump weights 121

9.36 Power spectra of pitch for all mooring systems 121

9.37 Comparison of yaw motion for all mooring concepts 122

9.38 Comparison of line tension in the windward line for all mooring concepts 123

9.39 Time series comparison of line tension in the windward line for pure chain and CPC systems 124

9.40 Comparison of the power spectrum of line tension in the windward line for pure chain and CPC systems 124

9.41 Time series comparison of line tension in the windward line for CPC systems with and without clump weights 125

9.42 Power spectra comparison of line tension in the windward line for CPC systems with and without clump weights 125

9.43 Time series comparison of line tension in the windward line for CPC and CNC systems 126

9.44 Time series comparison of line tension in the windward and leeward line for the CPC system 127

9.45 Time series comparison of line tension in the windward and leeward line for CPC system with Clump Weight 127

9.46 Time series comparison of line tension in the windward and leeward line for CNC system 127

A.1 First-order wave force transfer function in Surge 139

A.2 First-order wave force transfer function in Sway 140

A.3 First-order wave force transfer function in Heave 140

A.4 First-order wave force transfer function in Roll 141
A.5 First-order wave force transfer function in Pitch 141
A.6 First-order wave force transfer function in Yaw 142

B.1 RAO in Surge 143
B.2 RAO in Sway 144
B.3 RAO in Heave 144
B.4 RAO in Roll 145
B.5 RAO in Pitch 145
B.6 RAO in Yaw 146

C.1 Constant wind test result comparison with OpenFAST result for INO WINDMOOR 12 MW turbine 147

D.1 Surge Decay with Turning Points 149
D.2 Sway Decay with Turning Points 150
D.3 Heave Decay with Turning Points 150
D.4 Roll Decay with Turning Points 151
D.5 Pitch Decay with Turning Points 151
D.6 Yaw Decay with Turning Points 152

E.1 Yaw Time Series Comparison DLC 6.1.1 In-between collinear Condition 154

F.1 DLC 1.6 In-line collinear motions 155
F.2 DLC 1.6 In-between collinear motions 156
F.3 DLC 1.6 In-line collinear tension 156
F.4 DLC 1.6 In-between collinear tension 157

G.1 DLC 1.1 In-line collinear motions 159

G.2 DLC 1.1 In-between collinear motions 160
G.3 DLC 1.1 In-line collinear tension 160
G.4 DLC 1.1 In-between collinear tension 161

Nomenclature

List of abbreviation

1-D	One Dimensional
ABS	American Bureau of Shipping
ALS	Accidental Limit State
BEM	Blade Element Momentum
BV	Bureau Veritas
CAPEX	Capital Expenditure
CNC	Chain-Nylon-Chain
CoG	Centre of Gravity
CPC	Chain-Polyester-Chain
DLC	Design Load Case
DNV	Det Norske Veritas
DoF	Degree of Freedom
ECM	Extreme Current Model

ESS	Extreme Sea State
EWLR	Extreme Water Level Range
EWM	Extreme Wind speed Model
FEM	Finite Element Method
FLS	Fatigue Limit State
FWT	Floating Wind Turbine
IEC	International Electrotechnical Commission
JONSWAP	Joint North Sea Wave Observation Project
LF	Low Frequency
MBL	Minimum Braking Load
ML 1	Mooring Line 1
ML 2	Mooring Line 2
ML 3	Mooring Line 3
MPM	Most Probable Maximum
MSL	Mean Sea Level
MW	Mega Watt
NCM	Normal Current Model
NSS	Normal Sea State
NTM	Normal Turbulence Model
OPEX	Operational Expenditure
PDF	Probability Density Function

QA	Quality Assurance
QTF	Quadratic force Transfer Functions
RAO	Response Amplitude Operator
RNA	Rotor Nacelle Assembly
RP	Return Period
SSS	Severe Sea State
TDP	Touch Down Point
TLP	Tension Leg Platform
ULS	Ultimate Limit State
UN	United Nations
w.r.t	with respect to
WAFO	Wave Analysis for Fatigue and Oceanography
WF	Wave Frequency

List of commonly applied symbols

β	Wave Heading
Δx	Distance moved by the floater
$\overline{U}$	Mean Wind Velocity
ρ	Density of Water
ρ_{air}	Density of Air
ρ_{Steel}	Density of Steel
ε	Strain

$A(\omega)$	Frequency dependent Added Mass
$C(\omega)$	Frequency dependent Potential Damping
C_D	Drag Coefficient
C_T	Thrust Coefficient
D	Water Depth
D_l	Linear Damping
D_q	Quadratic Damping
EA	Axial Stiffness
H_s	Significant Wave Height
$K(x)$	Non-linear stiffness
K_E	Elastic Stiffness
K_G	Geometric Stiffness
K_T	Total Stiffness
M	Mass (or) Mass Matrix
Q	Excitation Force
S_C	Design Resistance or Characteristic Capacity
T	Thrust Tension
T_d	Design Tension
T_p	Peak Period
$T_{c,dyn}$	Characteristic Dynamic Tension
$T_{c,mean}$	Characteristic Mean Tension

V_{hub}	Wind Velocity at the hub
V_{hub}^{*}	Rated Wind Velocity at the hub
w	Submerged weight of mooring line
y	Water Depth

Chapter 1

Introduction

1.1 Background and Motivation

One of the seventeen sustainable development objectives set forward by the United Nations (UN) is to ensure access to affordable and clean energy. By 2030, the UN intends to achieve this aim by significantly expanding the amount of renewable energy in the global mix and ensuring universal access to affordable, reliable, and modern energy services [21]. The demand for electrification is currently more significant than ever to establish a sustainable future. By 2050, it is expected that the share of electricity in total world energy demand will have doubled, from 19 percent to 38 percent [6]. Offshore Floating Wind Turbines (FWT) have the potential to help achieve these objectives, as shown in Figure 1.1.

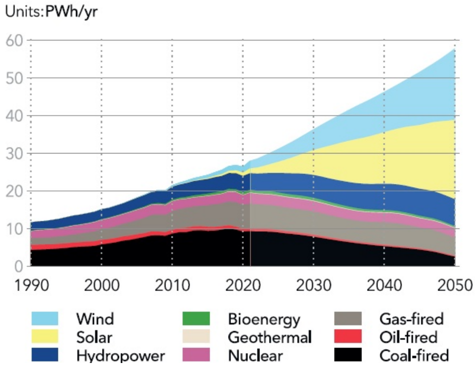

Figure 1.1: World grid-connected electricity generation by power station type [6]

Following such sustainable development aims, the wind sector has seen rapid growth in recent years, transitioning from onshore to offshore and from bottom-fixed shallow water to deep water floating solutions. For water depths more than 100 m, many of the FWT designs have been proposed. This is due to the availability of reliable wind resources at greater depths and the depletion of near-shore areas, respectively [7].

Figure 1.2 shows the list of wind farm pilot parks which will be commissioned by 2022.

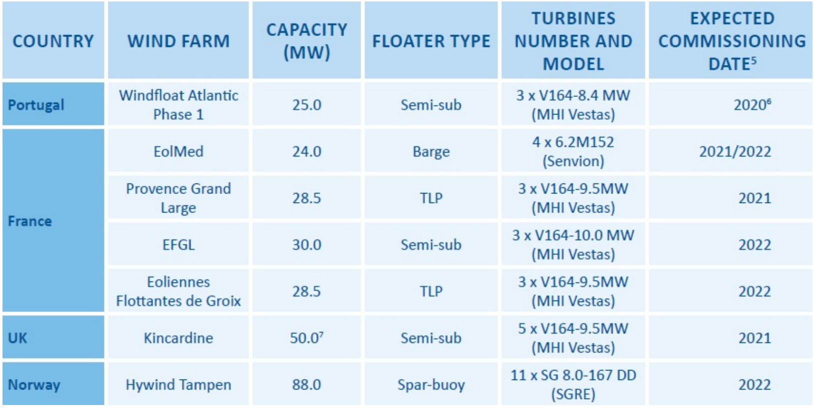

COUNTRY	WIND FARM	CAPACITY (MW)	FLOATER TYPE	TURBINES NUMBER AND MODEL	EXPECTED COMMISSIONING DATE[5]
Portugal	Windfloat Atlantic Phase 1	25.0	Semi-sub	3 x V164-8.4 MW (MHI Vestas)	2020[6]
France	EolMed	24.0	Barge	4 x 6.2M152 (Senvion)	2021/2022
	Provence Grand Large	28.5	TLP	3 x V164-9.5MW (MHI Vestas)	2021
	EFGL	30.0	Semi-sub	3 x V164-10.0 MW (MHI Vestas)	2022
	Eoliennes Flottantes de Groix	28.5	TLP	3 x V164-9.5MW (MHI Vestas)	2022
UK	Kincardine	50.0[7]	Semi-sub	5 x V164-9.5MW (MHI Vestas)	2021
Norway	Hywind Tampen	88.0	Spar-buoy	11 x SG 8.0-167 DD (SGRE)	2022

Figure 1.2: Proposed floating wind farms pilot parks in Europe [7]

Moving wind turbines from onshore to offshore has several benefits and drawbacks. One of the major advantages of offshore wind turbines is that they have a capacity factor of 30-60%, which is higher than onshore wind turbines [1]. A higher capacity factor implies that the average power output from offshore turbines will be higher. Furthermore, large regions are available for installing offshore wind turbines at a minimal cost. Offshore floating wind turbines have additional advantages, such as the ability to be towed out to the energy production site, which allows assembly in port and the ability to be situated further from shore, which reduces visibility and noise impacts [22]. Another significant advantage of moving wind turbines offshore is that the wind velocities are, in general, higher compared to land as there is no interference due to trees and buildings. In addition to this, the wind is less turbulent [1]. This is important because turbulent wind causes fatigue damage to the structure. However, the downside of offshore wind turbines would be the corrosive environment. It will also be challenging to access for carrying out any maintenance of the turbines. The capital expenditure (CAPEX) and operating expenditure (OPEX) are also higher for offshore wind turbines as the substructure and installation are more expensive than onshore turbines. Similarly, the OPEX increases as bad weather can lead to downtime. The following table summarises some of the benefits and drawbacks of offshore wind turbines.

Table 1.1: Pros and Cons of Offshore Wind Turbine compared to Onshore [1]

Advantages	**Disadvantages**
Extensive regions are available at a low price.	Wet and Corrosive Environment.
No noise or visual impacts.	Difficult to access for installation and maintenance.
Higher wind velocities and less turbulent winds.	Higher CAPEX and OPEX.
Ease of transportation and installation.	

Offshore wind turbines can be further classified as bottom-fixed wind turbines and floating wind turbines. Bottom-fixed wind turbines are viable in water depths up to 40-50 m, whereas floating wind turbines can be used in deeper waters beyond 50 m water depth [23]. Some of the potential locations such as Norway, Japan and the west coast of the US lack shallow water, making it more cost-effective to deploy FWT in deeper waters than bottom-fixed wind turbines [1]. Figure 1.3(a) shows the water depth around regions in Europe, and Figure 1.3(b) shows the map offshore South Korea, in the Sea of Japan, which is the location considered in this thesis. The water depth in this region is between 100-150 m [19].

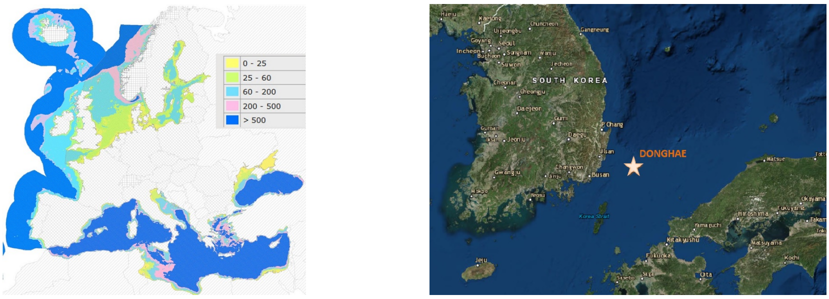

(a) Water depth in Europe [1] **(b)** Location offshore South Korea, DONGHAE [19]

Figure 1.3: Water depth in various regions

For an FWT, the mooring system is critical since it ensures that the structure does not drift and remains in place. Figure 1.4 shows the cost break-up for a typical bottom-fixed and floating wind turbine.

From Figure 1.4 it can be observed that mooring systems take up more than 10% of the total CAPEX, which is absent for bottom-fixed turbines. According to further

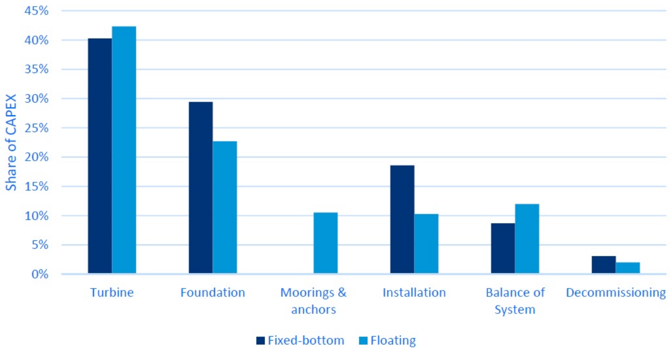

Figure 1.4: Cost break-up for typical bottom-fixed turbines and FWT [8]

discussions with supervisor Kjell Larsen, it was understood that the mooring system, including the accompanying maritime operations, might account for nearly 25% of the entire cost of FWT. So, to make offshore FWT feasible, the cost mooring system of FWT must be reduced.

The usage of 3–9 mooring lines per FWT is the standard practice in the industry. As a result, optimising the mooring system for the FWT is critical to reducing mooring system costs. Existing technologies from the oil and gas industry can be used when designing the mooring system for an FWT. However, because FWT structures are smaller than oil and gas structures, it is vital to build on these technologies to find new and better solutions.

1.2 Scope of Work

The overall goal of this thesis is to examine the mooring system for a floating wind turbine in detail. A description of the current state of FWTs, an overview of rules and regulations, and a deep dive into design methodologies and numerical analysis shall be included in the work. State-of-the-art mooring systems, as well as new alternatives, shall be evaluated and compared.

The objectives are stated as follows:

1. To review relevant literature on FWT concepts and mooring system design, emphasising the status of FWT concepts and different types of mooring systems applicable to an FWT with station-keeping principles and main hardware components.
2. To provide an overview of the design rules and standards for floating wind turbines. Based on the Design Load Cases (DLCs) given in the rules, discuss

relevant cases for the Ultimate Limit State (ULS) design of mooring systems for FWTs.

3. To describe the mooring design process and how numerical mooring analysis can be performed for an FWT, emphasising different approaches using time-domain analysis methods. To describe the environmental loads, FWT motions, estimation of the characteristic extreme values and models for mechanical behaviour (tension-elongation) of synthetic ropes. A separate section on aerodynamics shall also be included.
4. To develop a SIMA model of a 12MW FWT, the 12MW "INO WINDMOOR" model. To describe the model and different Quality Assurance (QA) checks performed on the model. To establish a "base case" mooring system based on chain only components to comply with the design requirements outlined in task 2) and operate in South Korea (Donghae location) in 100 m water depth.
5. To perform numerical simulations and comparison study of different mooring concepts and design methods. The numerical simulations shall focus on the use of both a coupled approach based on the use of SIMO and RIFLEX and checks using a quasi-static, uncoupled approach based on SIMO only. To propose an alternative and novel mooring system using synthetic ropes based on results from numerical analysis. The system may include clump weight components and buoys, often called as "hybrid" solutions.
6. Conclusions and recommendations for further work.

1.2.1 Approach

This master thesis is a continuation of TMR4520 Specialisation Project **Design and Numerical Analysis of Mooring Systems for Floating Wind Turbines** carried out in Autumn 2021. Hence, a significant part of the literature study has been carried out in the project thesis.

The first three tasks stated in Section 1.2 are achieved by reviewing appropriate literature and extracting relevant theory. The part concerning SIMA theory and calculations is based on the SIMO and RIFLEX manuals provided by SINTEF Ocean. The SIMO model with a mooring system consisting of pure chain segments used in the specialisation project is used for the "base case" study in task 4. The mooring line is modified to meet the design criteria based on the numerical analysis. To understand the difference between the coupled approach and the quasi-static uncoupled approach mentioned in task 5, a comparative study is additionally performed for the base case system using the SIMO model and a SIMO-RIFLEX coupled model. In addition to this, to propose an alternative novel mooring system using synthetic ropes, as mentioned in task 5, numerical simulations are carried out using a coupled SIMO-RIFLEX model. Various mooring concepts such as Chain-Polyester-Chain system, Chain-Polyester-Chain system with clump weights and Chain-Nylon-Chain system are evaluated using the coupled model.

1.3 Structure of the Report

This report is divided into ten chapters and is organized as follows:

Chapter 1 focuses on the background and motivation for the project and provides an outline of the scope of work.

Chapter 2 discusses various FWT concepts and typical mooring systems employed for an FWT. The hardware components in a mooring system and station keeping principles are also described.

Chapter 3 provides an overview of design standards and regulations applicable for the mooring design of an FWT with an emphasis on ULS criteria. Relevant load cases are also discussed.

Chapter 4 discusses the equation of motion and excitation forces acting on an FWT. The wind turbine aerodynamics and wind spectra are briefly discussed. In addition to this, some dynamic instabilities in an FWT are also described.

Chapter 5 describes the SIMA software package focusing on both SIMO and RIFLEX modules. In addition to this, a section on estimating response from a time-domain simulation is also described.

Chapter 6 describes various options available for modelling an FWT in SIMA with their advantages and disadvantages, along with a detailed description of the INO WINDMOOR 12 MW FWT model.

Chapter 7 provide the details of various mooring concepts evaluated in this thesis.

Chapter 8 explains the numerical simulations carried out in SIMA to verify the model and validate the mooring system for the environmental conditions in Donghae location, South Korea.

Chapter 9 presents the results and explanations of the numerical simulations carried out using both the SIMO model and coupled SIMO-RIFLEX model.

Chapter 10 presents the summary & conclusions of this thesis work. Recommendations for future work are also described.

Chapter 2

Mooring and Station keeping Systems for FWT

2.1 Floating Wind Turbines Concepts

There are four basic floater types for an FWT, as explained below.

1. **Semi-submersible Platform:** This is a column stabilised platform which floats on the ocean surface while anchored to the seabed through catenary mooring lines [8]. The turbine may be placed on top of one of the columns or at the geometric centre of the columns [11]. Kincardine floating offshore wind farm in the UK uses a semi-submersible substructure for mounting the wind turbines [7].

2. **Spar buoy:** This consists of a cylindrical hull structure that is ballast stabilised [8]. The stability is attained by maintaining the centre of gravity lower than the centre of buoyancy. Hywind Scotland and Hywind Tampen use a spar substructure to mount the wind turbine [7].

3. **Tension Leg Platform (TLP):** The floating platform is held in position by pre-tensioned tethers, which provide stability to the platform. The tethers may be anchored to the seabed using suction piles, driven piles, or a template foundation [11]. Provence Grand Large wind farm in France uses a TLP substructure to mount the wind turbines [7].

4. **Barge:** A barge type hull can also be used as a floating foundation for a wind turbine. EolMed floating wind farm pilot project in France uses a Barge type floater to mount the wind turbines [7].

Figure 2.1 shows different floater concepts available for FWTs.

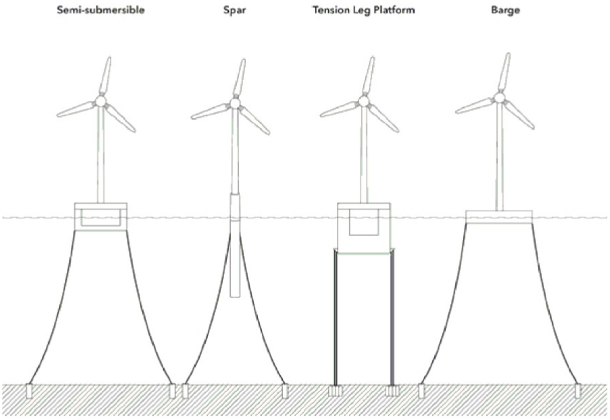

Figure 2.1: Common floater types for FWT [3]

As of 2020, there are nearly 25 floating platforms in development stages toward commercial-scale worldwide. Around 44% of this are semi-submersibles, followed by spar buoys and TLPs at 24% each and barge at 8% [9]. Figure 2.2 shows the list of active platform designs around the world.

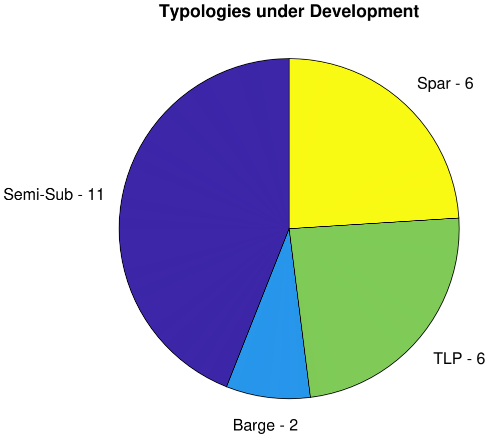

Figure 2.2: Platform designs under development stages toward commercial scale [9]

2.2 Mooring and Station Keeping Systems

Mooring and Station keeping systems are essential components of a floating offshore structure which ensures that the structure limits its horizontal motion and maintains its position. An FWT must maintain its position as the failure of mooring lines will lead to power line breakage and collision with surrounding floating structures or ships. Therefore, a reliable mooring system must be installed for a floating offshore structure.

2.2.1 Components of a Mooring System

A typical mooring system consists of the following components [10, 24]:

- Chain, Steel-wire rope or Synthetic Fibre ropes or their combination.
- Anchors or Piles
- Fairleads, Bending shoes or Padeyes
- Winches, Chain jacks or Windlasses
- Buoys or Clump weights
- Connecting Links

The main hardware components are depicted in Figure 2.3 and are described in detail below:

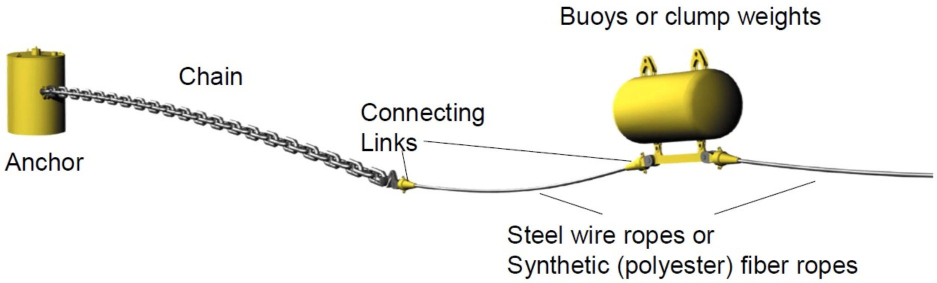

Figure 2.3: Main Mooring Line Components [10]

Chain:

The chain makes up the strength member of the mooring system [24]. Chains could either be studless or stud-link as shown in Figure 2.4. Chains have a large weight which provides them with high geometric stiffness. Chains have good abrasion characteristics and are commonly used in the top and bottom end of mooring lines. With the requirement to operate in deeper waters, the suspended weight of the chain becomes a limiting factor and hence is less attractive for greater water depths [24].

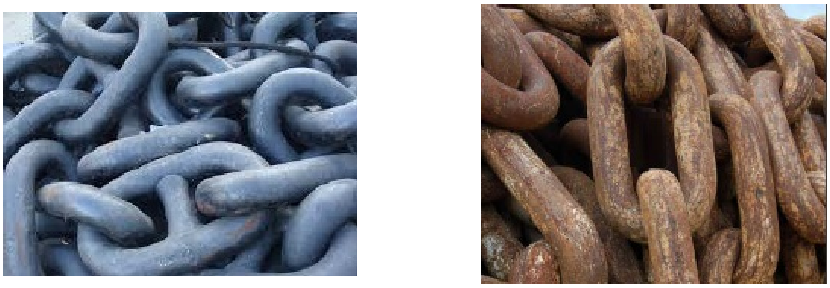

(a) Stud-link Chain

(b) Studless Chain

Figure 2.4: Stud-link and Studless Chain [10]

Steel Wire Rope:

These are either made of the spiral strand, which is covered with a plastic sheath as shown in Figure 2.5(a), or six-strand/multi-strand, which is uncovered as shown in Figure 2.5(b). These have lighter weight and higher elasticity than chains of the same breaking load [11]. Wire ropes are generally used in the water span.

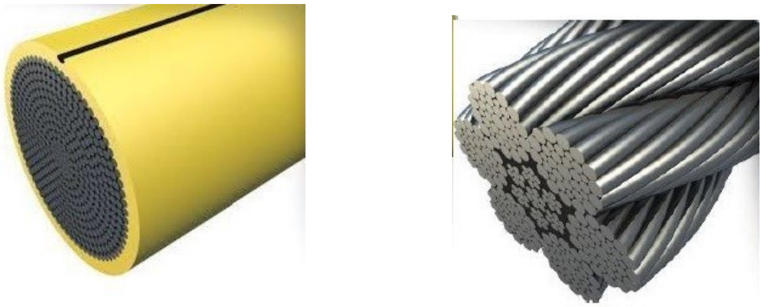

(a) Spiral strand wire rope

(b) Six-strand wire rope

Figure 2.5: Steel Wire Rope [10]

Synthetic Fibre Rope:

These are made of synthetic fibre materials such as Polyester, Aramids, HMPEs, or Nylon. However, synthetic fibre ropes made of polyester are most common and dominant in the market. They weigh less in water than steel wire ropes and have higher elasticity. An example of synthetic fibre rope with its different parts is shown in Figure 2.6.

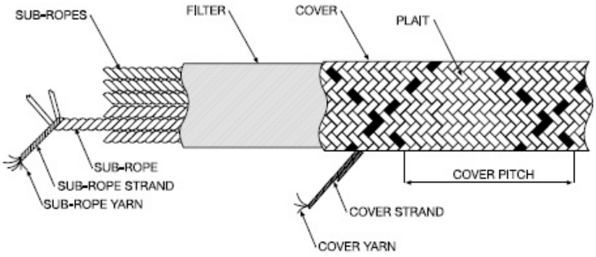
SUB-ROPES
FILTER
COVER
PLAIT
SUB-ROPE
SUB-ROPE STRAND
SUB-ROPE YARN
COVER PITCH
COVER STRAND
COVER YARN

Figure 2.6: Synthetic Fibre Rope [10]

Connectors or Connecting Links:

These are used to join sections of chain to one another or to connect a chain to a steel wire or synthetic fibre rope. These are designed to take the full breaking strength of the chain or wire rope. However, their fatigue strength must be carefully assessed [24].

Anchors:

Anchors can be broadly divided into two types [24]:

1. Relying on Self Weight
2. Suction Anchors

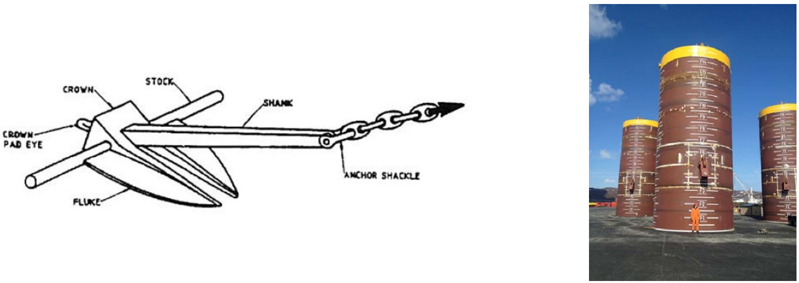
CROWN
STOCK
SHANK
CROWN PAD EYE
ANCHOR SHACKLE
FLUKE

(a) Drag Anchor [24]

(b) Suction Anchor [25]

Figure 2.7: Anchor Types

Traditional embedment anchors as shown in Figure 2.7(a) are not designed for vertical force components [24]. Their holding power depends on the seabed type and anchor weight. Suction anchors as shown in Figure 2.7(b) allow vertical anchor loads. Piles can be used as an alternative to anchors. However, they require large crane vessels with piling capabilities for installation [24].

Buoys and Clump Weights:

The purpose of adding buoys or clump weights to a mooring line is to improve the mooring performance by reducing the platform offset and reducing the weight of mooring lines that the platform must support. The additional weight provided by these clump weights increase the mooring system's restoring force [11]. Figures 2.8 and 2.9 shows the images of a buoy and clump weights respectively.

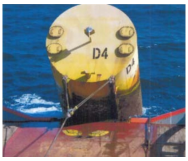

Figure 2.8: Buoy [11]

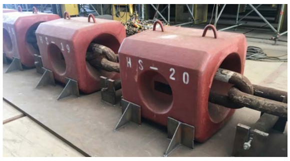

Figure 2.9: Clump Weights [11]

2.2.2 Mooring Systems for FWT

The most commonly used mooring system configurations for FWTs are taut leg mooring systems and catenary mooring systems. It is also possible to have a semi-taut mooring system which is a hybrid of catenary and taut-leg mooring systems.

Taut-leg Mooring System: In a taut leg mooring system, pre-tensioned mooring lines are used, making an angle between 30 - 40 degrees with the seabed as shown in Figure 2.10(a). Synthetic fibre or steel wire rope are used for such types of mooring systems, and the restoring forces are generated by the elasticity of the mooring lines. An advantage of this system is that it will have a small footprint on the seabed. It is suitable for deeper waters.

In the case of TLPs, tension leg mooring systems are used, which is different from taut leg mooring systems. The tension leg consists of tubular steel members called tendons that go vertically down to the seabed. Due to the high tension in these tendons, the horizontal offset is limited, and the heave, roll, and pitch motions are negligible due to high axial stiffness.

Catenary Mooring System: It consists of long steel chains or wires forming a catenary shape as shown in Figure 2.10(b). When the surface platform is displaced, the mooring lines lift-off or settle down on the seabed, causing an increase or decrease in line tension to produce a restoring force. It is most suited for shallow and medium water depths. However, it will have a large footprint on the seabed.

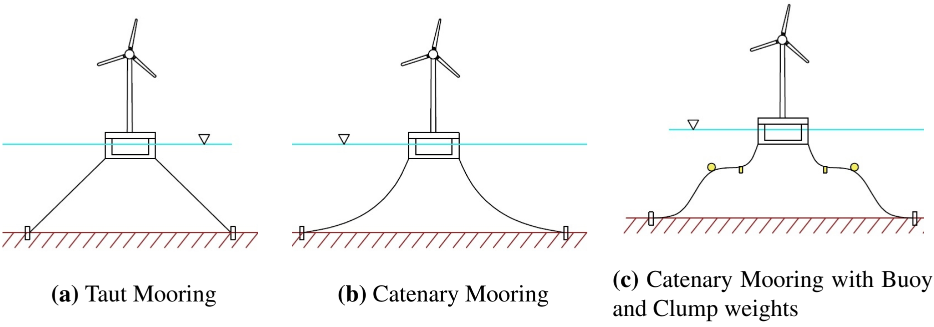
(**a**) Taut Mooring

(**b**) Catenary Mooring

(**c**) Catenary Mooring with Buoys and Clump weights

Figure 2.10: Typical Arrangement of Mooring Systems

2.2.3 Review of Mooring System for Pilot Parks

Various pilot parks have either been deployed or are under development, as shown in Figure 1.2. Each of these has a different type of substructure and mooring arrangement. Catenary mooring systems are most commonly used to secure the substructure of an FWT, as shown in Figure 2.11 [8].

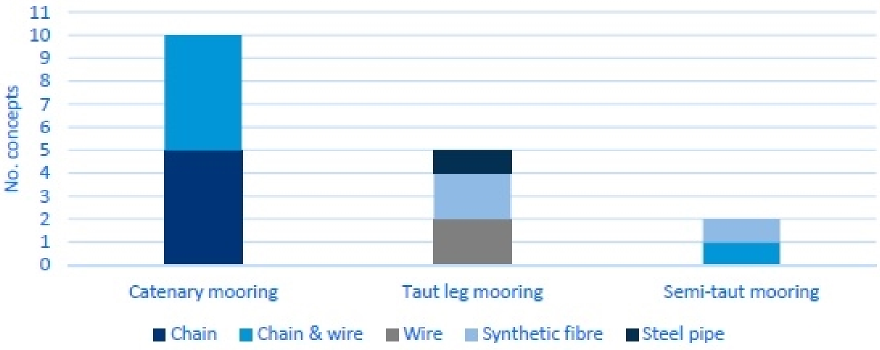

Figure 2.11: Mooring layout and types used for FWTs [8]

Most floating concepts call for at least three mooring lines to ensure adequate load distribution, motion control, and mooring system redundancy in the event of a failure; however, multi/hybrid solutions can utilise fewer anchors per turbine due to economies of scale [8]. TLP concepts, on the other hand, necessitate more mooring lines than other concepts, owing to the necessity to distribute the load evenly across the structure and dissipate high forces between more mooring lines and anchors [8]. The average number of mooring lines used per turbine is shown in Figure 2.12.

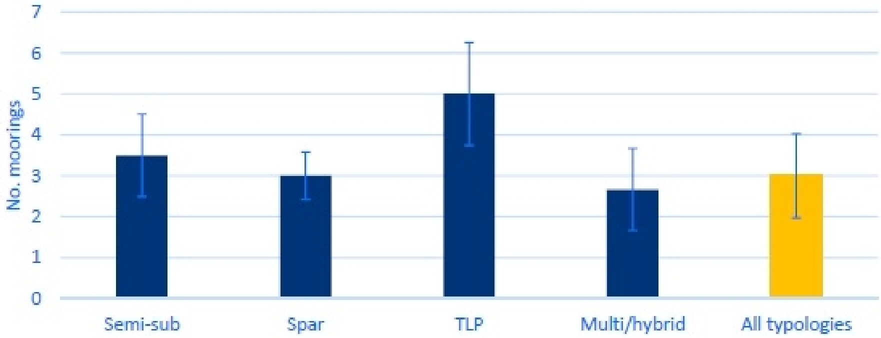

Figure 2.12: The average number of moorings per turbine [8]

Windfloat Atlantic has a triangular-shaped semi-submersible floater with the wind turbine mounted on one of the columns. It consists of three hybrid catenary mooring lines comprised of synthetic rope and chain connected to drag embedded anchors [8, 26].

Hywind Scotland and Hywind Tampen both have a spar buoy substructure with three hybrid catenary mooring lines connected to the seabed by suction anchors. The mooring lines comprise chain segments at the top and bottom and steel wire rope in the water column [10].

GICON-SOF is an FWT pilot project deployed in Germany with a TLP substructure anchored to the seabed with four vertical taut-leg mooring lines and an additional four support mooring lines to provide added stability which the designers anticipate to be equivalent to conventional fixed-bottom foundations [8]. Similarly, TLPWind is a concept developed by Iberdrola, which has a substructure made up of a central cylindrical column and four pontoons symmetrically distributed on its bottom. Two tendons are attached per pontoon which provides redundancy against potential tendon failure [8].

2.3 Station Keeping Principles

There are six Degrees of Freedom (DoFs) for a rigid body - three translations and three rotations. The three translational DoFs in x, y, and z directions are called Surge, Sway and Heave, respectively, and the three rotational DoFs in x, y, and z directions are called Roll, Pitch, and Yaw, respectively. These are shown in Figure 2.13 for an FWT.

Each DoF, when excited, oscillates at a different natural period. For a semi-

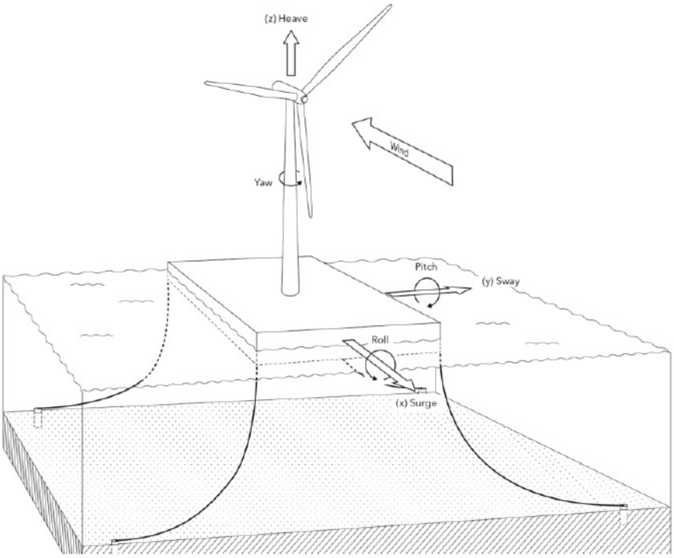

Figure 2.13: Rigid body motion modes for an FWT [3]

submersible, the typical values of natural periods in each of these DoFs are shown in Table 2.1.

Table 2.1: The typical natural time period in different DoF for an FWT

DoF	Surge	Sway	Heave	Roll	Pitch	Yaw
T_n [s]	$\approx> 50$	$\approx> 50$	15-30	25-30	25-30	$\approx> 80$

For an FWT, these DoFs can primarily be excited by waves, wind, and current. However, each of these phenomena would occur at different time periods, as shown in Figure 2.14, and hence can excite different DoF of the structure. Figure 2.14 show the forces that are relevant for an FWT in red.

A mooring system maintains the position of the structure by absorbing the Wave Frequency (WF) motions and controlling the mean offset and Low Frequency (LF) motions.

Equation of Motion

When the hydrodynamic forces on the structure are defined, the equation of motion of the structure can be written as shown in Equation (2.1).

$$(M + A(\omega)) \cdot \ddot{r} + C(\omega) \cdot \dot{r} + D_l \cdot \dot{r} + D_q \cdot \dot{r} \mid \dot{r} \mid + K(r) \cdot r = Q(t, r, \dot{r}) \tag{2.1}$$

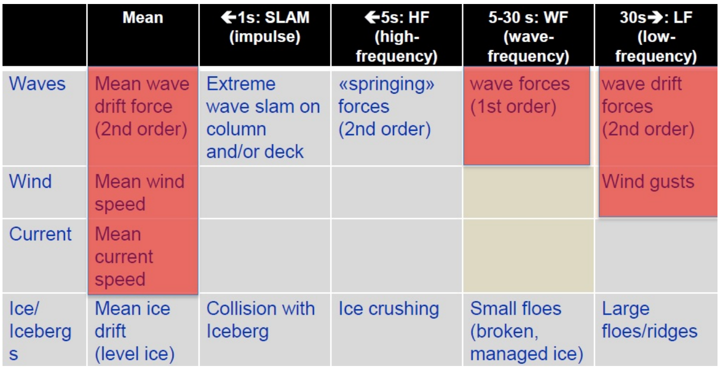

	Mean	←1s: SLAM (impulse)	←5s: HF (high-frequency)	5-30 s: WF (wave-frequency)	30s→: LF (low-frequency)
Waves	Mean wave drift force (2nd order)	Extreme wave slam on column and/or deck	«springing» forces (2nd order)	wave forces (1st order)	wave drift forces (2nd order)
Wind	Mean wind speed				Wind gusts
Current	Mean current speed				
Ice/ Icebergs	Mean ice drift (level ice)	Collision with Iceberg	Ice crushing	Small floes (broken, managed ice)	Large floes/ridges

Figure 2.14: Excitation Time Scales [10]

where,

M	mass matrix
$A(\omega)$	frequency dependent added mass matrix
r	position vector
$C(\omega)$	frequency dependent potential damping matrix
D_l	linear damping matrix
D_q	quadratic damping matrix
$K(r)$	stiffness matrix (non-linear)
$Q(t, r, \dot{r})$	excitation force vector :

The equation of motion is explained in detail in Section 4.1.1.

Considering the equation of motion in surge, the equation can be simplified as shown in Equation (2.2).

$$(M + A_{11}(\omega)) \cdot \ddot{x} + (C_{11}(\omega) + D(\dot{x})) \cdot \dot{x} + K(x) \cdot x = Q(t, x, \dot{x}) \tag{2.2}$$

The quadratic damping provided by the mooring lines reduces the LF motion, and the stiffness provided by the mooring lines controls the mean offset and LF motions. The restoring force is generated by the geometric and elastic stiffness of the mooring lines.

2.3.1 Geometric Stiffness

The physical interpretation of geometric stiffness can be explained as follows.

The geometric stiffness of the mooring line is due to the submerged weight of mooring lines in the water. In the equilibrium position of the mooring line, the moment due to the submerged weight of the mooring line is balanced by the moment due to horizontal force from the mooring line.

$$F_h \cdot D = W_w \cdot a \tag{2.3}$$

where,

F_h	Horizontal force from the mooring line
D	Water Depth
W_w	Submerged weight of mooring lines in water
a	Arm of submerged weight from the top end of the mooring line

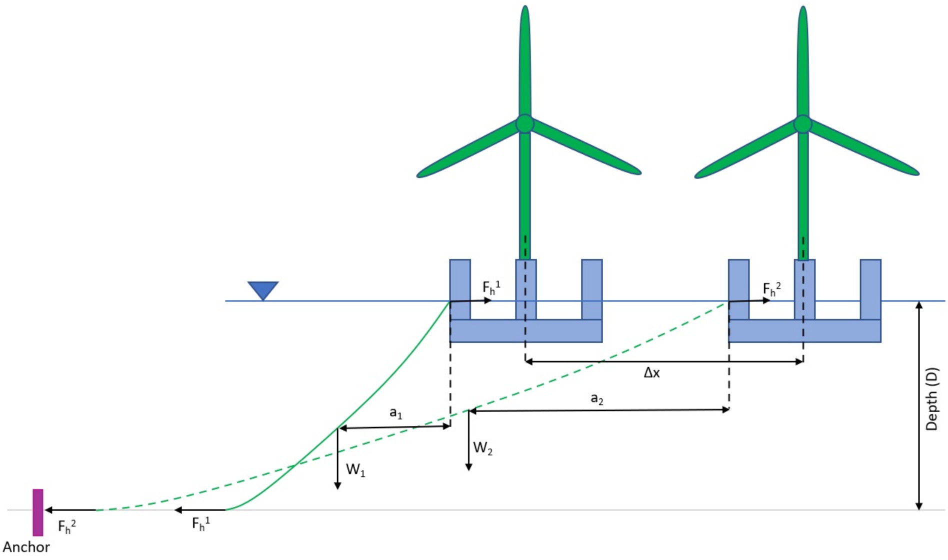

Figure 2.15: Geometric Stiffness of Catenary System

When the configuration of the mooring line changes due to the movement of the floating structure, the submerged weight and its moment change, which results in a different horizontal force. The difference in horizontal forces divided by the distance moved by the structure gives the geometric stiffness of the mooring line. This is illustrated in Figure 2.15.

$$K_G = \frac{F_h^2 - F_h^1}{\Delta x} \tag{2.4}$$

where,

K_G	Geometric stiffness of the mooring line
F_h^2	Horizontal force due to change in configuration of mooring line
F_h^1	Initial Horizontal force
Δx	Distance moved by the platform

For catenary chain/steel wire rope, geometric stiffness is important.

2.3.2 Elastic Stiffness

The elastic stiffness is provided by the axial stretch or elongation of the mooring line. This is illustrated in Figure 2.16.

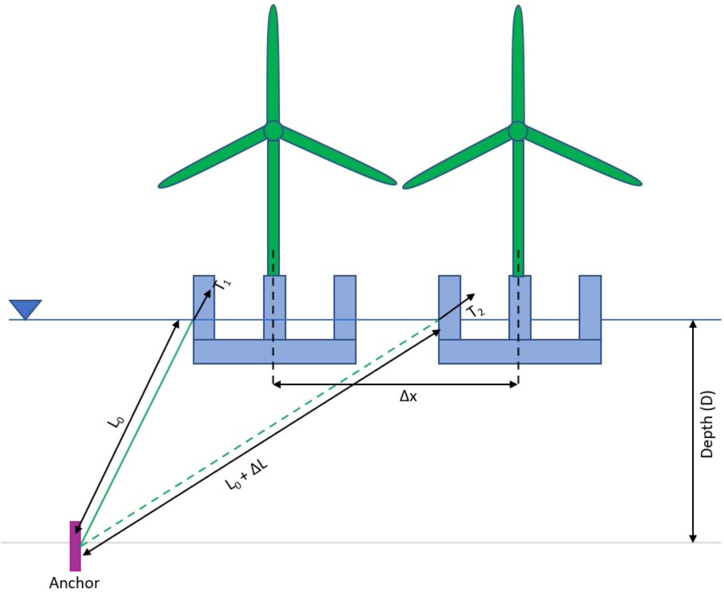

Figure 2.16: Elastic Stiffness of a Taut system

The elastic stiffness can be estimated as:

$$\Delta T = T_2 - T_1 = \frac{EA \cdot \Delta L}{L_0} \qquad \text{where } K_E = \frac{EA}{L_0} \tag{2.5}$$

where,

K_E	Elastic Stiffness of the mooring line

EA	Axial Stiffness of the line
L_0	Length of the rope in its mean configuration
ΔL	Length elongated by the rope
T_1 & T_2	Tension in the line in two positions

For polyester rope, elastic stiffness is dominating. The stiffness of a synthetic rope is further explained in Section 2.5.

Total Restoring Stiffness

The total restoring stiffness is the combination of both geometric and elastic stiffness as illustrated in Figure 2.17 and can be estimated as given in Equation (2.6).

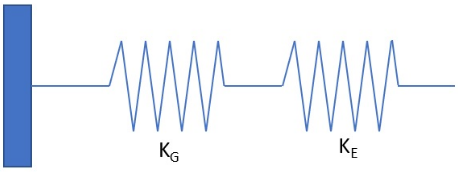

Figure 2.17: Total Restoring Stiffness

$$\frac{1}{K_T} = \frac{1}{K_G} + \frac{1}{K_E} \tag{2.6}$$

where,

K_T	Total Line stiffness

K_T is analytically calculated using catenary equations. This is explained in Section 2.4.

2.3.3 System Restoring Force

Three mooring lines are often utilised for an FWT. When the platform moves, the horizontal tension in the windward line increases, and the leeward line decreases due to the external force. The difference in horizontal tension between the windward and leeward lines can be used to estimate the total system restoring force, as shown in Figure 2.18.

An example of a spread mooring system with three lines and nine lines for an FWT is shown in Figure 2.19. A spread mooring system's restoring force in surge, sway and yaw can be expressed as given in Equations (2.7a)–(2.7c) respectively.

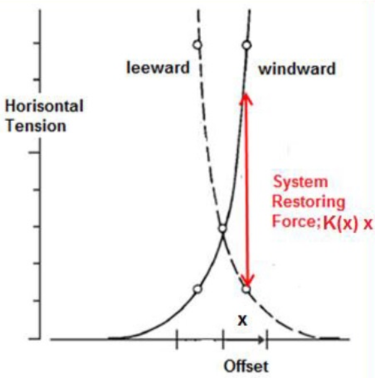

Figure 2.18: System restoring force due to both windward and leeward lines [10]

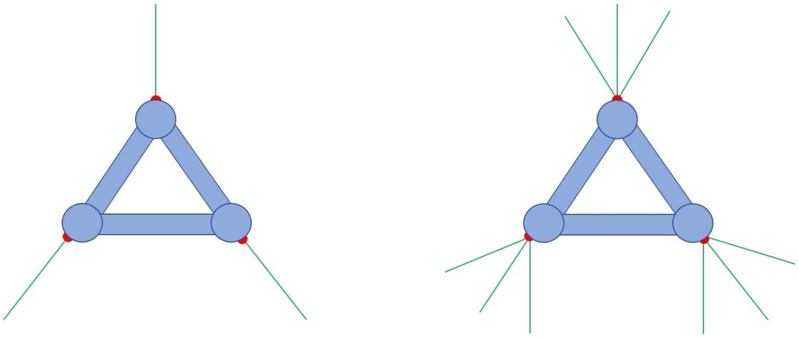

(a) Spread mooring with three mooring lines **(b)** Spread mooring with nine mooring lines

Figure 2.19: Spread Mooring Arrangement

$$F_x = \sum_{i=1}^{n} T_{xi} \cdot cos\psi_i \tag{2.7a}$$

$$F_y = \sum_{i=1}^{n} T_{xi} \cdot sin\psi_i \tag{2.7b}$$

$$M_r = \sum_{i=1}^{n} T_{xi} \cdot [x_i \cdot sin\psi_i - y_i \cdot cos\psi_i] \tag{2.7c}$$

Here T_{xi} is the horizontal force from anchor line number i. Its direction is from the attachment point of the anchor line, i.e., from fairlead to anchor. x_i and y_i represent the $x-$ and $y-$coordinate of the attachment point of the anchor line to the vessel. ψ_i is the angle between the anchor line and the x-axis as shown in Figure 2.20.

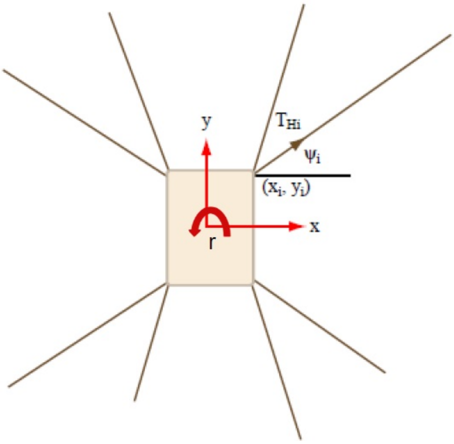
y
T_{Hi}
ψ_i
(x_i, y_i)
x
r

Figure 2.20: Mooring system restoring forces [10]

2.4 Static Equilibrium of Mooring Lines

This section is based on [10, 27]. Consider a two-dimensional mooring line with zero bending stiffness as shown in Figure 2.21.

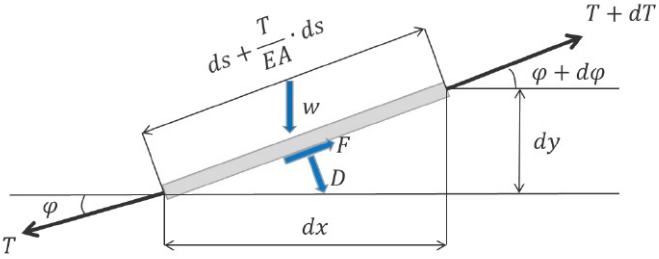
$ds + \frac{T}{EA} \cdot ds$
$T + dT$
$\varphi + d\varphi$
w
F
D
dy
φ
T
dx

Figure 2.21: A 2D mooring line with forces acting on it [10]

From the figure, the following notations can be defined:

- D, F - External forces due to current on the line in radial and tangential directions, respectively.
- w - Submerged weight per unit length of the mooring line.

- EA - Axial stiffness of the mooring line per unit length, where A is the cross-sectional area and E is the elastic modulus.
- ds - The length of the segment of the mooring line under consideration.
- T - Tension of the mooring line.
- φ - Angle between the mooring line and horizontal plane.

The bending stiffness is neglected, which is a good approximation for chains and wires with a large radius of curvature [27]. The dynamic effects in line are also neglected. The static equilibrium of the segment of length ds in tangential and normal directions can then be expressed as:

Tangential direction:

$$dT = \left[w \cdot sin(\varphi) - F\left(1 + \frac{T}{EA}\right)\right] \cdot ds \tag{2.8}$$

Normal direction:

$$T \cdot d\varphi = \left[w \cdot cos(\varphi) + D\left(1 + \frac{T}{EA}\right)\right] \cdot ds \tag{2.9}$$

These equations can be referred to as catenary equations. These are non-linear, and in general, it is not possible to find an explicit solution. For typical mooring line components, the tension is much less than the axial stiffness, and hence it can conveniently be assumed that $\frac{T}{EA} << 1$. Therefore this term can be neglected, and it simplifies the analysis.

2.4.1 Solutions of Inelastic Cable Line (Catenary) Equations

It is possible to solve for the submerged length of the mooring line, s, distance to the Touch Down Point (TDP), x, and the vertical component of tension in the mooring line, T_y, using the pretension of the mooring line, T_0, the submerged weight of the mooring line, w, and water depth, y.

The so-called line characteristics, which is a relationship between the top tension of the mooring line and the offset of the floater, are of particular interest [10].

Figure 2.22 shows the notations used for defining line characteristics.

When the top end of the line moves, the TDP moves considerably. Hence, choosing the anchor point as an earth-fixed reference point for the calculation is convenient.

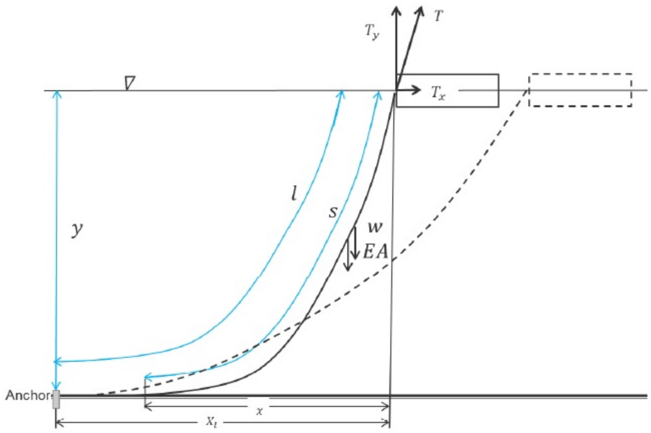

Figure 2.22: Illustration of notations defining line characteristics [10]

The distance to anchor, X_l, is often known, and hence it is of interest to calculate the horizontal tension at the top of the line. Using the Catenary Equations (2.8) and (2.9) and combining several equations, the following relation can be derived for a line with no elasticity:

$$X_l = l + \frac{T_x}{w} \cdot cosh^{-1}\left(1 + \frac{w \cdot y}{T_x}\right) - \sqrt{y \cdot \left(y + \frac{2T_x}{w}\right)} \qquad (2.10)$$

where,

l	Length of mooring line
T_x	Horizontal Tension at the top of the line

Equation (2.10) is referred to as the line characteristics.

2.4.2 Line Characteristics with Line elasticity included

The elasticity must be accounted for in the mooring lines, either if the lines are long or if the tension levels are high or if the line contains multiple elastic segments. Equations (2.11) and (2.12) shows the line characteristics considering line elasticity.

$$T_x = EA \cdot \left[\sqrt{\left(\frac{T}{EA} + 1\right)^2 - \frac{2wy}{EA}} - 1\right] \qquad (2.11)$$

$$x = \frac{T_x}{w} \cdot sinh^{-1}\left(\frac{T_y}{T_x}\right) + \frac{T_x \cdot T_y}{w \cdot EA} \qquad (2.12)$$

2.5 Synthetic Ropes

A typical mooring line configuration usually comprises of hybrid mooring lines with chain segments in the upper and lower section and synthetic or steel wire rope in the water span. The use of synthetic ropes in the water span is gaining more popularity due to its properties and also the fact that it can reduce the cost of the overall mooring system [28].

As described in Section 2.3, the total stiffness of the mooring line is a combination of geometric stiffness given by the chain and elastic stiffness provided by the synthetic ropes. For mooring systems with synthetic line segments, the axial, elastic properties of the synthetic rope determine the resulting line stiffness [2].

2.5.1 Axial Stiffness of Synthetic Ropes

This section is based on the reference provided from Equinor on the engineering models that are used to estimate the axial stiffness of synthetic mooring lines [2].

A linear stiffness model has traditionally been used to represent the axial, elastic stiffness of synthetic ropes.

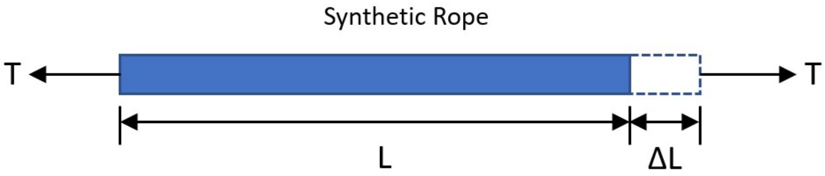

Figure 2.23: A synthetic rope segment under tension

Consider a segment of a synthetic rope as shown Figure 2.23. The length of the segment is L. An axial tension T is applied on either side of the rope, due to which the rope elongates by the length ΔL. The strain on the segment can be expressed as

$$\varepsilon = \frac{\Delta L}{L} \tag{2.13}$$

The relation between tension (T), axial stiffness (EA) and strain (ε) can be expressed as

$$T = EA \cdot \varepsilon \tag{2.14}$$

Based on Equation (2.14), a typical tension strain curve can be represented as shown below.

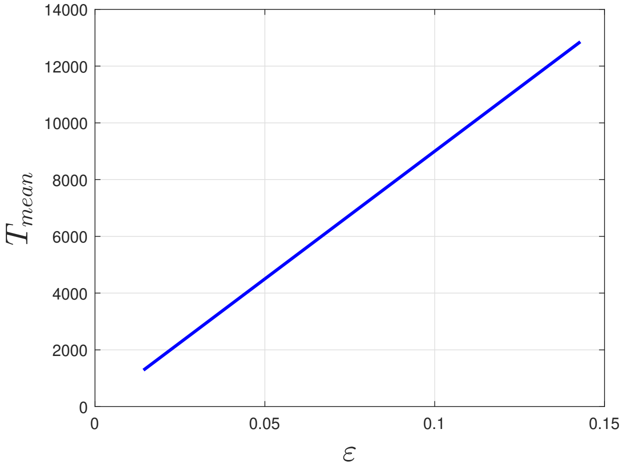

Figure 2.24: A typical tension strain curve

However, based on full-scale testing of synthetic ropes, it has been determined that the synthetic fibre ropes have a visco-elastic change in length characteristics, and hence, when the tension on the rope changes, the corresponding change-in-length response has a non-linear trend [29]. This is shown in Figure 2.25.

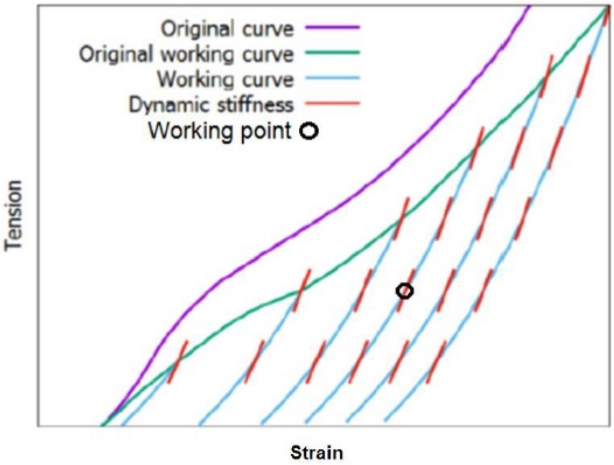

Figure 2.25: Principle tension-strain curves observed and adapted from testing [2]

The original curve shown in the figure represents the tension versus strain plot, which is obtained during the first quick loading of a new rope. When the rope is held at a given tension for a period of time, the rope elongates further, resulting in an original working curve. So, the original working curve represents the stationary working point if the rope is at its highest tension and permanent strain is taken out after some time [2]. The working curve represents the path through which the rope returns to its mean configuration when the tension is released. The working curve describes a non-linear relation between the mean tension and mean strain and determines the static elastic stiffness of a synthetic rope, which is used to estimate the offset due to mean wind, wave and current loads [2].

The static working curve can be represented using the following equation:

$$\frac{T_{mean}}{MBL} = \frac{f}{g \cdot 100} \cdot [exp(g \cdot 100 \cdot \varepsilon_{mean}) - 1] \tag{2.15}$$

where,

T_{mean}	Mean tension
MBL	Minimum breaking strength of the rope
ε_{mean}	Mean strain

f and g are constants estimated from full-scaling testing. The values of these constants for polyester and nylon ropes are given in Table 2.2.

Table 2.2: Parameters used for Static elastic stiffness [2]

Synthetic fibre type	Parameters for STATIC stiffness (working curve)	
	Parameter f	Parameter g
Polyester	3.0	0.6
Nylon	0.2	0.26

The static working stiffness curve for polyester and nylon ropes is shown in Figure 2.26.

The dynamic stiffness shown in Figure 2.25 is a linear curve which increases slightly with mean tension. Dynamic stiffness is used for calculating the response due to WF and LF excitations [2].

The dynamic tension model is similar to the static stiffness model and can be represented by the following equation:

$$T_{dyn} = EA_d \cdot \varepsilon_{dyn} = (b \cdot 100 \cdot T_{mean} + a \cdot MBL) \cdot \varepsilon_{dyn} \tag{2.16}$$

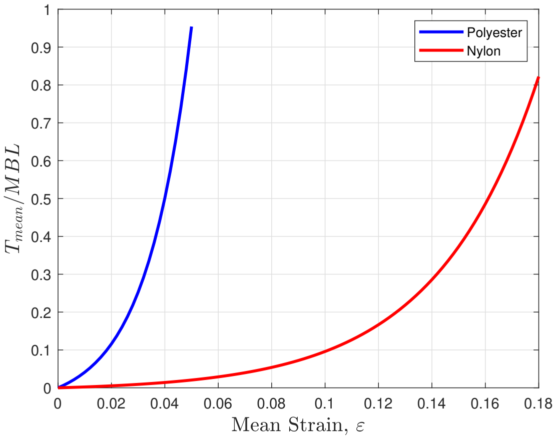

Figure 2.26: Static Stiffness (Working Curve) for polyester and nylon ropes

Equation (2.16) can be re-written as follows:

$$\frac{EA_d}{MBL} = b \cdot 100 \cdot \frac{T_{mean}}{MBL} + a \tag{2.17}$$

where,

T_{dyn}	Dynamic tension
ε_{dyn}	Dynamic strain
EA_d	Dynamic stiffness

a and *b* are constants estimated from full-scale testing. The values of these constants for polyester and nylon ropes are given in Table 2.3.

Table 2.3: Parameters used for Dynamic elastic stiffness [2]

Synthetic fibre type	Parameters for DYNAMIC stiffness	
	Parameter *a*	Parameter *b*
Polyester	20	0.25
Nylon	1	0.4

The linearised dynamic stiffness curve for polyester and nylon ropes is shown in Figure 2.27.

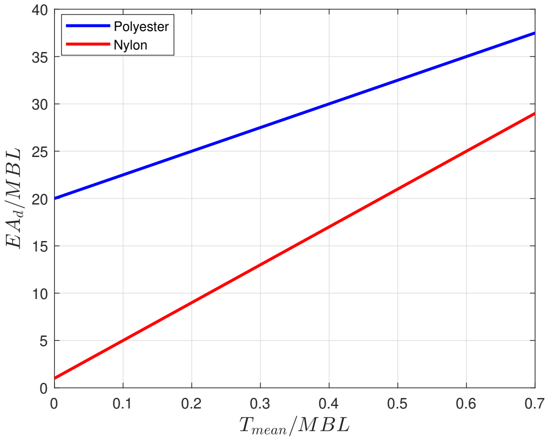

Figure 2.27: Linearised Dynamic Stiffness for polyester and nylon ropes

2.5.2 Procedure for Estimating total tension

The total tension can be estimated through the following steps:

- The mean tension, T_{mean}, is estimated using the non-linear working curve.
- The dynamic tension, T_{dyn}, is estimated using the linear dynamic stiffness, where the linear dynamic stiffness is obtained corresponding to T_{mean} estimated above.
- Total Tension is the sum of mean and dynamic tensions.

$$T_{tot} = T_{mean} + T_{dyn}$$

Chapter 3

Design Standards and Regulations

3.1 Rules and Standards for a Floating Wind Turbine

FWT is a relatively new concept, and the industry is transitioning from pilot projects to commercial projects. To assist in the segment's expansion, various international classification societies such as Det Norske Veritas (DNV) Maritime, Bureau Veritas (BV) Marine & Offshore, American Bureau of Shipping (ABS) and international organisations such as the International Electrotechnical Commission (IEC) have come up with rules and regulations applicable for floating offshore wind turbines. This chapter gives an overview of different rules and regulations that govern the design of the station-keeping system for an FWT.

3.1.1 IEC 61400

This is an international standard published by the IEC regarding wind turbines. This standard specifies the rules and regulations for wind turbines' proper engineering to prevent damage from dangers over their expected lifetime [30].

IEC 61400 series consists of various parts, out of which IEC 61400-3-2 deals with the FWT and provides the design requirements for station keeping systems for an FWT. As per IEC 61400-3-2, the station-keeping system for FWT shall be designed following ISO 19001-7, and it provides the design situations and load cases for station keeping systems. An overview of these load cases is included in the DNV rules and is discussed in the subsequent sections.

3.1.2 DNV Standard

DNV, formerly known as DNV-GL, is a classification society that provides a set of rules and regulations for ships and offshore structures called Class Rules. DNV has issued standards for floating offshore wind turbines such as DNVGL-ST-0437 and DNVGL-ST-0119.

DNVGL-ST-0437 provide principles, technical requirements, and guidance for loads and site conditions of wind turbines. DNVGL-ST-0119 provide regulations, technical requirements, and guidance for the design, construction, and in-service inspection of floating wind turbine structures and station-keeping systems for floating wind turbines. Furthermore, DNVGL-RP-C205 is used to define the environmental conditions and loads. In this thesis, the DNV standards are followed to design the station keeping system and are discussed in detail in the subsequent sections.

3.2 Design Requirements for Mooring Lines

The design requirements for mooring lines are given based on Chapter 8 of DNVGL-ST-0119 [3].

3.2.1 Limit States

A limit state is a condition beyond which a structure or component will no longer satisfy the design requirement. The following limit states are relevant for the design of a mooring system:

- Ultimate Limit State (ULS): It corresponds to the maximum load-carrying resistance.
- Fatigue Limit State (FLS): It corresponds to the failure due to the effect of cyclic loading.
- Accidental Limit State (ALS): It corresponds to survival conditions in a damaged condition or in the presence of abnormal environmental conditions.

3.2.2 ULS and ALS Design Criteria

To design the mooring and station keeping system for an FWT, the limit states of the mooring system shall be checked and verified. The ULS check is carried out to ensure that an intact mooring system shall withstand all known loads with a sufficient margin in extreme weather conditions [10]. The ALS check is performed on a damaged mooring system to ensure that an accident shall not develop into a progressive collapse of the structure in extreme weather conditions [10]. The design of a mooring system against overload for ULS and ALS shall be checked as follows:

$$Design\ load \leq Design\ Resistance$$

Design Criterion

As per DNVGL-ST-0119 [3], the design criterion for ULS or ALS is calculated as shown in Equation (3.1).

$$S_C > T_d \tag{3.1}$$

where S_C is defined as the body's characteristic capacity and T_d is the design tension.

Characteristic Capacity

The design resistance or characteristic capacity of the body of the mooring line is calculated as:

$$S_C = \mu_S \cdot (1 - COV_S \cdot (3 - 6 \cdot COV_S)); \quad COV_S < 0.10 \tag{3.2}$$

where,

μ_S	The mean value of the breaking strength of the component
COV_S	The coefficient of variation of the breaking strength of the component

This formulation applies to mooring lines consisting of chain, steel wire rope, and synthetic fibre rope [3]. The characteristic capacity of the body of the mooring line can also be obtained from the minimum breaking strength, S_{mbs}, of new components as [3]:

$$S_C = 0.95 \cdot S_{mbs} \tag{3.3}$$

Design Tension

The total of two factored characteristic tension components, characteristic mean tension, $T_{c,\,mean}$, and characteristic dynamic tension, $T_{c,\,dyn}$, determines the design tension, T_d, of a mooring line and can be calculated as shown in Equation (3.4).

$$T_d = \gamma_{mean} \cdot T_{c,mean} + \gamma_{dyn} \cdot T_{c,dyn} \tag{3.4}$$

where γ_{mean} and γ_{dyn} are the load factors. These are given in Table 3.1 for both ULS and ALS cases.

The characteristic mean tension, $T_{c,\,mean}$, can be defined as the mean part of the 50-year value of the line tension and is caused by pretension and mean environmental loads from static wind, current and wave drift, whereas the characteristic

Table 3.1: Load factor requirements for the design of mooring lines [3]

Limit State	Load factor	Consequence class	
		1[a)]	2[a)]
ULS	γ_{mean}	1.30	1.50
ULS	γ_{dyn}	1.75	2.20
ALS	γ_{mean}	1.00	1.00
ALS	γ_{dyn}	1.10	1.25

[a)] Consequence class 1 = where failure is unlikely to lead to unacceptable consequences such as loss of life, collision with an adjacent structure, and environmental impacts. Consequence class 2 = where failure may lead to unacceptable consequences of these types.

dynamic tension, $T_{c,\,dyn}$, is the dynamic part of the 50-year value of the line tension and is caused by oscillatory LF and WF effects [31].

To estimate $T_{c,\,mean}$ and $T_{c,\,dyn}$ using stochastic wind fields and/or irregular sea states, a simulation of 1-hour duration shall be performed for multiple realisations with different seeds [4]. The $T_{c,\,mean}$ shall be estimated as the mean of means of line tension and $T_{c,\,dyn}$ shall be the Most Probable Maximum (MPM) value of line tension from these simulations. Further details on how to determine the extreme response from a time series is explained in Section 5.5.

3.2.3 Discussion on Design Load Cases for ULS Design

The governing ULS cases for mooring design are found in environmental conditions with a 50-year Return Period (RP) and a parked turbine. The 50-year value of line tension, on the other hand, may not necessarily occur during a sea state in this two-dimensional contour because sustained wind speeds at the rated wind speed, where the operational thrust is maximum, may generate the most drift and the most loads in the mooring system [31]. Therefore, conditions with maximum turbine thrust are equally important and must be checked [31]. Figure 3.1 shows a typical curve with the variation of total wind force acting on the FWT with respect to (w.r.t) the wind velocity at the hub.

Table 3.2 shows the list of DLCs applicable for ULS design check of mooring lines.

Both DLCs 1.1 and 1.6 shall be examined during the power production condition. For DLC 1.6, the wind condition shall have a Normal Turbulence Model (NTM), and wind velocity at the hub, V_{hub}, shall be equal to the rated wind speed, V_{hub}^{*}. The significant wave height, H_s, in this condition shall be corresponding to the H_s at Severe Sea State (SSS). This condition will be the most critical during power production. However, from the metocean data [19], it can also be seen that as V_{hub}

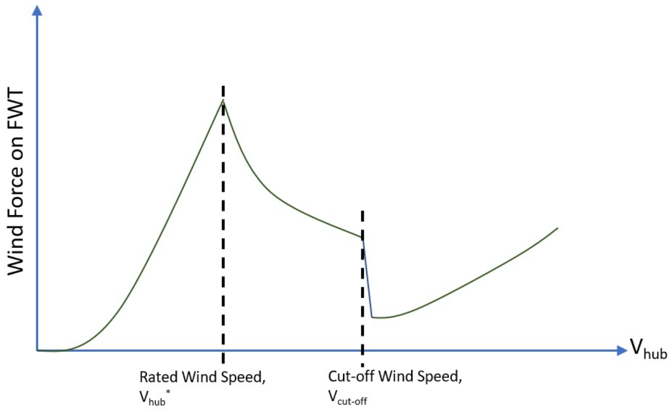

Figure 3.1: Variation of wind force on an FWT w.r.t the wind velocity at the hub

Table 3.2: Design load cases for station keeping system [4]

Design situation	DLC	Wind condition	Marine Condition			
			Waves	Wind and wave directionality	Sea Currents	Water Level
Power Production	1.1	NTM $V_{in} < V_{hub} < V_{out}$	NSS $H_s = \mathrm{E}[H_s \mid V_{hub}]$	COD, UNI	NCM	MSL
	1.6	NTM $V_{in} < V_{hub} < V_{out}$	SSS $H_s = H_{s,sss}$	COD, UNI	NCM	NWLR
Parked (standing still or idling)	6.1	EWM $V_{hub} = V_{ref}$	ESS $H_s = H_{s,50}$	MIS, MUL	ECM $U = U_{50}$	EWLR

NTM = Normal Turbulence Model
NCM = Normal Current Model
EWM = Extreme Wind Model
ECM = Extreme Curent Model
NWLR = Normal Water Level Range
COD = Co-Directional
MIS = Misaligned

NSS = Normal Sea State
SSS = Severe Sea State
ESS = Extreme Sea State
MSL = Mean Sea Level
EWLR = Extreme Water Level Range
UNI = Uni-Directional
MUL = Multi-Directional

increases, the H_s also increases exponentially. This is shown in Figure 3.2. Hence, at the cut-off velocity, $V_{cut-off}$, the H_s will be higher than at the rated condition. Hence, DLC 1.1 also has to be evaluated with NTM where $V_{hub} = V_{cut-off}$ at Normal Sea State (NSS) where H_s is equal to the expected value of H_s at $V_{cut-off}$.

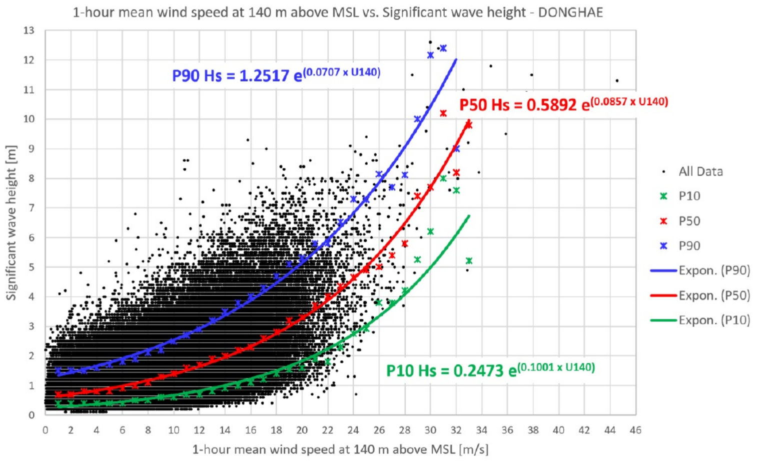

Figure 3.2: Variation of significant wave height w.r.t the wind velocity at the hub

For DLC 6.1, the turbine shall be in parked condition, i.e., standing still or idling. Extreme Wind Model (EWM) and Extreme Sea State (ESS) shall be applied, both of which correspond to the wind speed and significant wave height at 50-year condition. The 50-year ESS used for DLC 6.1 as per DNV-ST-0437 is associated with a 50-year current. This is quite conservative regarding mooring design, as there is typically a low correlation between current and the values of wind and waves. Hence, the RP of current shall be reduced to 5 years [31]. While performing this reduction, it may be required to also demonstrate an additional load case with a current equivalent to 50-year RP and wind and wave with 5-year RP. However, as the 50-year data for currents is not available in the metocean data, this condition is not checked.

3.3 Fatigue Design

The mooring lines also have to be designed against fatigue failure. The design cumulative fatigue damage for mooring lines can be estimated by [3]:

$$D_D = DFF \cdot D_C \tag{3.5}$$

where,

DFF	The design fatigue factor. It varies based on the consequence class as shown in Table 3.3
D_C	The characteristic cumulative fatigue damage caused by the stress history in the mooring line over the design life and can be estimated by Miner's Rule.

Table 3.3: DFF for mooring chain [3]

Consequence Class	DFF
1	5
2	10

The fatigue design criterion is:

$$D_D \leq 1.0 \tag{3.6}$$

3.4 Design Requirements for Anchors

The design requirements for anchors are given based on Chapter 9 of DNVGL-ST-0119 [3].

The design force, T_d, operating on the anchor and arising from line tension in a mooring line connected to the anchor is equal to the design line tension in the mooring at the interface between the mooring line and the anchor [3]. When more than one mooring line is connected to the anchor, the design force, T_d, operating on the anchor must be computed considering all mooring line contributions.

The design anchor resistance, R_d, can be calculated as:

$$R_d = \frac{R_c}{\gamma_m} \tag{3.7}$$

where,

R_c	The characteristic geotechnical anchor resistance
γ_m	Material factor as defined in Table 2.3

Table 3.4: Material factors for different types of anchors [3]

Anchor Type	Material factors γ_m	
	ULS	ALS
Pile Anchor	1.30	1.00
Gravity Anchor	1.30	1.00
Free-fall Anchor	1.30	1.00
Suction Anchor	1.20	1.00 (1) 1.20 (2)
Fluke Anchor	1.30	1.00 (1) 1.30 (2)
Plate Anchor	1.40	1.00 (1) 1.30 (2)

(1) Consequence class 1

(2) Consequence class 2

The design criterion for anchors is given by:

$$T_d \leq R_d \tag{3.8}$$

Chapter 4

Theoretical Background

4.1 Forces and Motion

A floating structure in the sea is subjected to various environmental loads. These environmental loads induce a motion to the floater and mooring system. The horizontal and vertical motions at the top end of the mooring line are important to be quantified when designing the mooring system [10].

The motions of a mooring system can be classified as static or mean and dynamic. The mean offset causes static motions, while WF and LF motions cause dynamic motions. The mean offset is caused by mean forces such as second-order mean wave drift force, mean wind speed, and mean current speed, as shown in Figure 2.14. Dynamic forces result in WF and LF motions. First-order wave forces cause the WF motions and the LF motions are caused by second-order wave drift forces and wind gusts.

4.1.1 Equation of Motion

The equation of motion in 6 DoFs can be expressed as shown below.

$$(M + A(\omega)) \cdot \ddot{r} + C(\omega) \cdot \dot{r} + D_l \cdot \dot{r} + D_q \cdot \dot{r}|\dot{r}| + K(r) = Q(t, r, \dot{r}) \tag{4.1}$$

The first term on the left-hand side of Equation (4.1) represents the inertia force. The subsequent three terms represent the damping force due to frequency-dependent potential damping, linear damping and quadratic damping respectively, and the last term represents the restoring force. The term on the right-hand side represents the excitation force.

The excitation force can be further expressed as shown in Equation (4.2).

$$Q(t, r, \dot{r}) = q_{wa}^{1} + q_{wa}^{2} + q_{wi} + q_{cu} + T \tag{4.2}$$

where,

q_{wa}^{1}	First-order wave force
q_{wa}^{2}	Second-order wave force
q_{wi}	Wind drag on the floater and tower
q_{cu}	Current force (Viscous force)
T	Thrust force generated by the turbine

These forces are explained in the Section 4.2.

4.2 Excitation Forces

A wind turbine in the sea will encounter environmental loads due to wind, waves and current. The mooring system shall be designed to withstand these loads and maintain the floating structure in its position. The environmental loads acting on an FWT is shown in Figure 4.1 and are described in the subsequent sections.

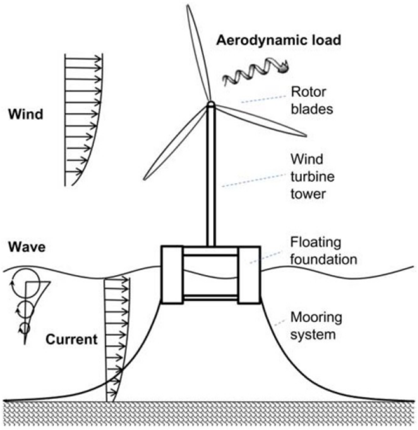
Aerodynamic load
Rotor blades
Wind
Wind turbine tower
Wave
Floating foundation
Mooring system
Current

Figure 4.1: Environmental loads acting on an FWT [11]

4.2.1 Wave Loads

The wave forces acting on an FWT can be categorised as first-order wave forces and higher-order wave forces. The first-order loads are, in general, larger than the higher-order loads.

First-Order Wave Loads

The first-order wave forces are proportional to the wave amplitude and are calculated using the linear potential flow theory by solving the velocity potential, ϕ, up to the first order. In order to solve the velocity potential, the wave body interaction problem is divided into a diffraction problem where the body is fixed with incoming waves and a radiation problem where the body is forced to oscillate without any incident waves, as shown in Figure 4.2.

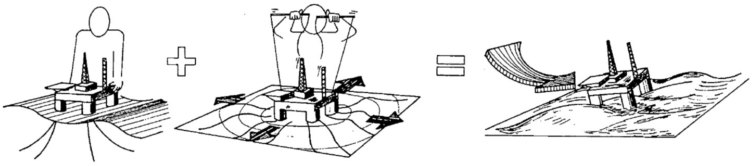

Figure 4.2: Wave body interaction problem [12]

In the diffraction problem, a fixed body interacts with incident waves. As a result, the body experiences excitation force due to the linear dynamic pressure of the incident wave, which is called the Froude-Kriloff loads and the linear dynamic pressure of the diffracted waves generated by the body, as it is impermeable, which is known as the diffracted loads [27]. There is no incident wave in the radiation problem, and the body is forced to oscillate in each of the 6 DoFs. This results in added mass and damping loads which are 180° out of phase with the body acceleration and velocity, respectively [27]. It also results in restoring loads which are caused due to the change of buoyancy and is 180° out of phase with the body motion [27]. These are estimated using numerical tools based on potential theory such as WAMIT, Hydrostar etc.

These loads have zero mean value and oscillate with the frequency of incident waves [12]. These typically act in periods ranging from 5 to 30 seconds. As shown in Figure 2.14, these result in WF motions of the platform. The WF motions create cyclic tensions that cause maximum tensions and fatigue damage accumulation in the mooring lines [11]. These loads are defined by force transfer functions.

As the INO WINDMOOR FWT substructure is modelled using slender elements as described in Chapter 6, to determine the loads on a slender structure, Morison's equation is used, which is a long wave viscous approximation. It assumes that the waves that are interacting with the structure are long relative to the cross-sectional dimension of the body [12]. For an elemental length, dz, Morison's equation can be expressed as shown in Equation (4.3).

$$dF = \underbrace{\rho C_M \frac{\pi D^2}{4} a_1 dz}_{\textit{Mass Force}} + \underbrace{\frac{\rho}{2} C_D D u|u| dz}_{\textit{Drag Force}} \tag{4.3}$$

where ρ is the density of seawater, D is the diameter of the slender element, C_M and C_D are the mass and drag coefficients respectively, a_1 is the acceleration in the direction of inflow estimated at the geometric centre of the cross-section, and u is the velocity of inflow in the direction of force at the geometric centre.

As described in Section 6.2.7, first-order force transfer functions are calculated using WAMIT for the 12MW FWT model and are included in SIMA. These force transfer functions obtained from WAMIT include the Diffracted and Froude Kriloff loads. These, however, do not include the viscous effects as it is estimated using solvers based on potential theory. As a result, the mass force from Morison's equation is included in force transfer functions from WAMIT, and only the drag force is calculated using Morison's equation. The drag force can be combined with the current loads and can be calculated as viscous loads. This is explained in Section 4.2.3.

Second-Order Wave Loads due to Potential Theory

Among the higher-order, second-order wave forces are important as they are relevant for designing a mooring system [27]. Second-order wave forces are caused by mean and LF wave drift forces. Viscous drag forces combined with current will also result in higher-order excitation forces. As shown in Figure 2.14, the LF wave drift forces have a period greater than 30 s and can typically excite the mooring system at its natural periods in surge, sway and yaw. Second-order mean wave drift forces are generally much smaller than the first-order wave forces and are more difficult to estimate both numerically and experimentally. The wave drift loads are defined by Quadratic force Transfer Functions (QTF).

Description of Waves

Ocean waves consist of irregular waves, which can be expressed as the sum or superposition of regular long-crested waves, each having a different amplitude, frequency and phase angle [32]. The time series for an irregular sea state can be expressed by linear wave theory and creating different regular waves with random phases as shown in Equation (4.4).

$$\zeta(t) = \sum_{j=1}^{N} A_j \sin(\omega_j t + \varepsilon_j) \tag{4.4}$$

where A_j, ω_j and ε_j are the amplitude, frequency and phase angle of the regular wave. The amplitude can be estimated from a wave spectrum, $S(\omega)$.

$$A_j = \sqrt{2S(\omega_j)\Delta\omega} \tag{4.5}$$

Each irregular sea state can be represented by a wave spectrum. A wave spectrum is a function of significant wave height (H_s) and peak period (T_p). Several standardised wave spectra exist, but the Pierson - Moskowitz Spectrum and Joint North Sea Wave Observation Project (JONSWAP) [32] spectrum are the most commonly used. JONSWAP spectrum is used to define the sea state in this thesis, and the spectrum may be expressed by the frequency, f, on the form:

$$S(f) = \alpha g^2 (2\pi)^{-4} f^{-5} \mathrm{exp}\left[-\frac{5}{4}\left(\frac{f}{f_p}\right)^{-4}\right] \gamma^{\mathrm{exp}\left[-\frac{(\frac{f}{f_p}-1)^2}{2\sigma^2}\right]} \tag{4.6}$$

where,

α	Spectral parameter
f_p	Peak wave frequency
γ	Peakedness parameter
σ	Spectral parameter

4.2.2 Wind Loads

The total wind force acting on an FWT can be divided into two parts, namely a mean thrust force acting on the rotor and a mean and LF component acting on the floater and tower. To address the wind loads, as with waves, it is fundamental to understand how the wind can be defined.

Description of Winds

This section is based on [1]. The short term description of the wind can be divided into three parts:

1. **Mean Spatial Variation:** This is the part of wind that does not vary in time. An example of mean spatial variation can be the vertical wind shear which is related to the boundary layer of the earth and results in lower wind speeds closer to the ground and increasing wind speeds higher up. This is shown in Figure 4.3. This is usually described by a power profile or a log profile. It is also worth noting that the wind shear may not just be vertical [1]. Other types of wind shear include directional shear, speed shear or a combination of both. The shear profile also depends on atmospheric stability [1].

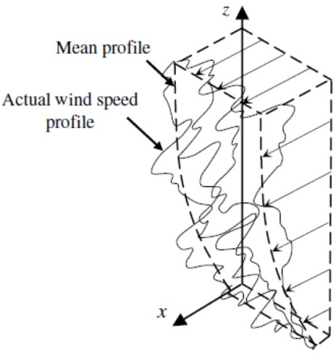

Figure 4.3: Vertical Wind Shear [1]

2. **Temporal Variation at a Point:** This refers to the wind variation at a point in space. Short-term variations are of the greatest interest for an offshore wind turbine [1]. This is usually described using a wind spectrum as shown in Figure 4.4. The most commonly used wind spectrum for atmospheric wind is the Kaimal spectrum. Von-Karman spectrum is commonly used for wind tunnels [1].

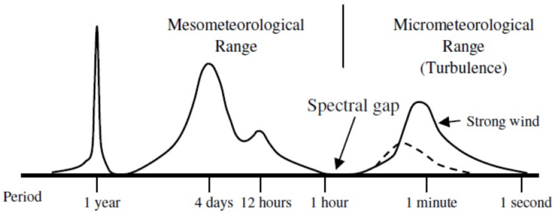

Figure 4.4: Wind speed spectrum over a broad range of frequencies [1]

3. **Spatial Coherence:** Spatial coherence means that two points, such as the two tips of the wind turbine blades, which are far apart and that experience the same spectrum and may experience the low frequency component of the wind at the same time, but the high frequency part may have no relation with each other. As the distance between the points decreases, the high frequency component will be more related and vice-versa. This feature of wind is of importance for wind turbines with large rotor diameters. Typically Kaimal or Mann spatial coherence models are used to describe this.

Wind Drag on Floater and Tower

The wind velocity consists of two components as shown in Figure 4.5.

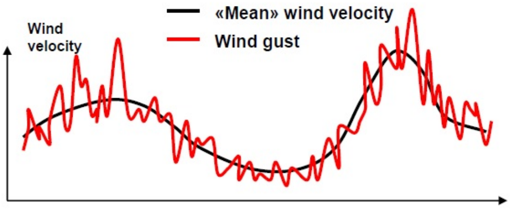

Figure 4.5: Components of Wind Velocity [10]

The wind force acting on the floater and tower can be divided into two components; a static load which is caused by the mean wind speed component, and the LF dynamic force due to wind gusts. The wind gusts have significant energy at surge, sway and yaw natural periods and can excite LF motions of the moored floating structure [10].

The wind force acting on an elemental strip of length dz on the floater or tower can be expressed as shown in Equation (4.7). The total force shall be obtained by integrating the elemental force throughout the length of the tower and floater, respectively.

$$dq_{wi} = \frac{\rho_{air}}{2} \cdot C_D \cdot A \cdot (U(t) - \dot{x}(z))^2 dz \tag{4.7}$$

where

ρ_{air}	Density of air
C_D	Drag coefficient of the structure
A	Projected area of the structure
$U(t)$	Wind Velocity
$\dot{x}(z)$	Horizontal Velocity of the structure at vertical location z

The wind velocity, $U(t)$, can be expressed as the sum of mean wind speed, $\overline{U}$, and dynamic wind gust, $u(t)$ as shown in the equation below.

$$U(t) = \overline{U} + u(t) \tag{4.8}$$

The total wind force on the tower or floater can then be approximated as follows:

$$q_{wi}(t) \approx \frac{\rho_{air}}{2} \cdot C_D \cdot A \cdot \overline{U}^2 + \rho_{air} \cdot A \cdot \overline{U} \cdot u(t) - \rho_{air} \cdot C_D \cdot A \cdot \overline{U} \cdot \dot{x} \tag{4.9}$$

The first term on the right hand side of Equation (4.9) represents the static load imposed by mean wind speed, while the second and third terms represent the LF excitation and damping force, respectively.

Thrust Force

This section is based on [13].

In addition to the loads on the floater and tower, the rotation of the wind turbine blades creates a circular region at the top of the tower, resulting in an abrupt drop in air pressure, which in turn creates a force in the direction of the wind called the thrust force [33]. This thrust force is required to slow down the wind speeds to extract the kinetic energy from the wind. To understand how the thrust and power can be derived from a wind turbine, it is fundamental to understand the concepts of aerodynamics explained below.

One Dimensional Momentum Theory

One dimensional (1-D) momentum theory serves as the basis for determining the thrust and power from an ideal turbine. The term "ideal wind turbine" refers to a wind turbine that does not lose energy when converting wind to electricity. This theory approximates the turbine as an actuator disk placed inside a control volume as shown in Figure 4.6.

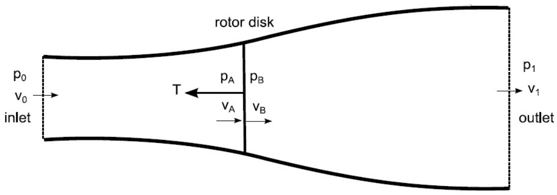

Figure 4.6: One-dimensional actuator disk rotor model [13]

The assumptions for an ideal wind turbine are:

1. Homogeneous, incompressible and steady-state flow
2. No frictional drag
3. Infinite number of blades and uniform thrust over the disk
4. Non-rotating wake
5. Pressure jump at the rotor disk with continuous velocity across the rotor disk

6. Pressure is equal to the ambient pressure far from the disk

The governing equations for 1-D momentum theory are the conservation of mass, the conservation of momentum and Bernoulli's equation. Using these equations, the velocity at the rotor disk can be expressed as the average of the wind velocities at the inlet and outlet of the control volume as shown in Equation (4.10).

$$v_a = 0.5 \cdot (v_0 + v_1) \tag{4.10}$$

where,

v_a	Wind velocity at the disk
v_0	Inlet Wind Velocity
v_1	Outlet Wind Velocity

This method also introduces an axial induction factor, a, which is the fractional decrease of the velocity in the stream tube.

$$a = \frac{v_0 - v_a}{v_0} \tag{4.11}$$

Using the axial induction factor, an expression for outlet velocity can be derived as follows:

$$v_1 = v_0(1 - 2a) \tag{4.12}$$

Combining Equation (4.12) with the governing equations, expression for thrust, T, and power, P, can be derived as shown in Equations (4.13) and (4.14) respectively.

$$T = 0.5 \cdot \rho_{air} \cdot A \cdot (v_0^2 - (v_0(1 - 2a))^2) \tag{4.13}$$

$$P = 0.5 \cdot \rho_{air} \cdot A \cdot v_0^3 \cdot 4a(1 - a)^2 \tag{4.14}$$

where ρ_{air}, A and v_0 are the density of air, rotor area and incoming wind velocity, respectively.

The power extracted by the rotor disk is a function of the air density, rotor area and the power coefficient, C_P. The power coefficient should be maximum to maximise extracted power. With the axial induction factor known, the maximum power extracted from the incoming wind can be found when $C_P = 0.59$ and $a = 1/3$. This theoretical maximum is called the Betz Limit.

However, the actual power that can be extracted by a wind turbine is less than the theoretical Betz Limit [13]. This is because a wind turbine has a finite number of blades, and wake rotation occurs behind the turbine as the torque exerted by the blades will cause the flow to rotate in the opposite direction. Hence the assumptions considered in the 1-D momentum theory are not valid for an actual wind turbine.

Ideal Turbine with Wake Rotation

To consider the effect of wake rotation for an ideal turbine an additional coefficient called the angular induction factor, a', must be introduced. The angular induction factor is a function of the rotor's angular velocity, Ω, and angular velocity imparted to the free stream, ω. As the control volume rotates with the blades, annular sections must be considered. With ω and Ω known, the pressure difference over the rotor disk can be calculated and integrating this over the annulus gives us the incremental thrust, dT, and the rate of change of angular momentum gives us the torque on an incremental annular area element, dQ. The resulting expression for a' to obtain maximum extracted power is given below.

$$a' = \frac{1-3a}{4a-1} \tag{4.15}$$

Blade Element Momentum Theory

An actual wind turbine consists of blades made out of airfoil cross-sections. An airfoil subjected to incoming flow generates lift and drag forces as shown in Figure 4.7. These forces vary depending on the angle of attack, ϕ.

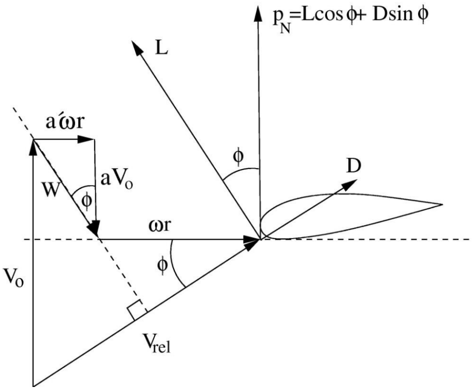

Figure 4.7: Velocity and forces acting on an airfoil cross-section [13]

Airfoil theory combined with an ideal wind turbine with a rotating wake forms the basis for the Blade Element Momentum (BEM) theory. The inflow velocity, V_{rel}, includes the incoming wind, the velocity of the blade due to rotor rotation, the induced axial velocity, and the induced tangential velocity. The typical solution procedure for BEM is described below [13]:

- Guess starting values for a and a'.
- Calculate the flow angle, angle of attack and determine the lift and drag coefficients.
- Update the values of a and a'.
- Check for convergence of the values of a and a' and if they have not converged, repeat the process using the current values of a and a'.

The thrust, power extracted and loads experienced by the blades are all calculated automatically as a result of this technique. However, many engineering corrections are applied to this method, such as Prandtl correction, Glauert Correction, Dynamic Wake and Dynamic Stall, to account for the assumptions and physical effects [13]. The thrust force is proportional to changes in wind speed and can be either dynamic or static. As a result, if the wind speed varies, the thrust force is composed of both static and dynamic forces [33].

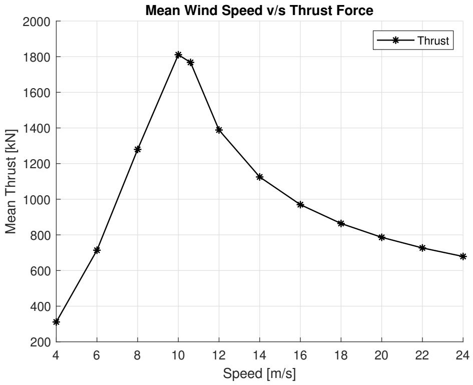

Figure 4.8: Mean wind speed v/s thrust force for INO WINDMOOR turbine

The thrust force as a function of mean wind speed for the 12MW INO WINDMOOR turbine is shown in Figure 4.8. An FWT will experience a mean offset in surge and pitch DoFs due to the mean thrust force, which is critical for the design of the mooring system.

4.2.3 Current Loads

Current velocity is a combination of wind-generated currents and tidal currents. The effects of currents should be considered for the design of offshore structures as they can cause large steady excursions and slow drift motions of moored platforms [18]. Ocean currents induce drag force on the floating structure proportional to the square of the current velocity [11]. The current velocity varies with water depth, and the total current velocity at a given location should be taken as the vector sum of each current component present [18].

For the motion response of the floating structures, the current velocity at the surface is important, and the velocity profile is assumed to be constant over the water depth. The current force can be calculated as shown in Equation (4.16).

$$q_{cu}(t) = \frac{\rho}{2} \cdot C_D \cdot A \cdot |\overline{V} - \dot{x}| \cdot (\overline{V} - \dot{x}) \tag{4.16}$$

where ρ, C_D, A and $\dot{x}$ are the density of water, drag coefficient, projected area and LF velocity of the structure, respectively. $\overline{V}$ is the mean current velocity.

If $\overline{V} > \dot{x}$, then current force can be approximated as:

$$q_{cu}(t) \approx \frac{\rho}{2} \cdot C_D \cdot A \cdot \overline{V}^2 - \rho \cdot C_D \cdot A \cdot \overline{V} \cdot \dot{x} \tag{4.17}$$

The first term on the right hand side of Equation (4.17) represents the mean force due to current and the second term represents LF damping force.

Viscous Loads

The presence of even a low magnitude current along with waves can result in viscous drift loads because of the viscous effect of the combined velocity of waves and currents [34]. As the wave-current interaction effects result in a flow field of viscous origin, the non-linear viscous drag term of the Morison equation is used to compute the viscous drift loads [34].

The viscous load per unit length in presence of current can be expressed as follows:

$$f_D = \frac{\rho}{2} C_D D |\overline{V} + u| (\overline{V} + u) \tag{4.18}$$

where u is the wave-particle velocity. In the case of floating structures, the structure itself will oscillate with a horizontal velocity, $\dot{x}$. Hence the relative velocity of the structure w.r.t to the incoming wave-particle velocity shall be considered to calculate the viscous drift loads on the structure, and Equation (4.18) can be modified as shown below:

$$f_D = \frac{\rho}{2} C_D D |\overline{V} + u - \dot{x}| (\overline{V} + u - \dot{x}) \tag{4.19}$$

4.3 Dynamic Instabilities in an FWT

The purpose of this section is to provide an overview of various dynamic instabilities that have been observed in an FWT. Some of these instabilities are observed for a long time, while some others are recent. These are listed below.

1. **Pitch motion instability above rated wind speed due to negative feedback [35]**

   This type of stability problem occurs when a turbine with low natural frequencies is used in conjunction with a traditional pitch controller [35]. This is observed at wind speeds higher than the rated wind speed and when the tower's natural frequency is less than the natural frequency of the pitch controller. The reason for this instability is the effect of thrust force on tower motion, as it directly contributes to damping [35]. For turbines mounted offshore, the 1^{st} tower frequencies reduce considerably and become less frequent than the pitch action. This results in the thrust gradient following a negative slope of the quasi-static thrust curve, thereby leading to negatively damped tower motion [35].

2. **Mathieu Instability**

   This instability is relevant for spar type of platforms [36]. This instability occurs when there is a harmonic variation in the pitch restoring coefficients produced by substantial heave motion and the period of the heave motion is half of the pitch natural period [37]. When heave resonance occurs at half the pitch natural period, a type of lock-in event occurs due to Mathieu instability, considerably increasing pitch motion [37].

3. **Yaw misalignment in Idling or Parked Condition and Extreme Sea state**

   This relatively new instability is observed when the turbine is parked or idling in extreme sea states. When an FWT is subjected to wind loads, as shown in Figure 4.9, the FWT rotates in yaw through an angle, α, and experiences a moment, M, in yaw. This is caused due to the wind force acting on the semi, tower and the rotor nacelle assembly (RNA).

   The wind force on the semi forces it to rotate in yaw, but the mooring system attached to the semi provides a restoring moment and thus tries to bring the semi back to its actual position, thereby providing a positive stiffness. However, the force due to wind on the tower tends to push it further away from its mean position until it reaches 90°. Similarly, the wind force on the RNA also tends to rotate it away from its mean position. As both tower and RNA do not have a restoring effect and tend to move away from their mean

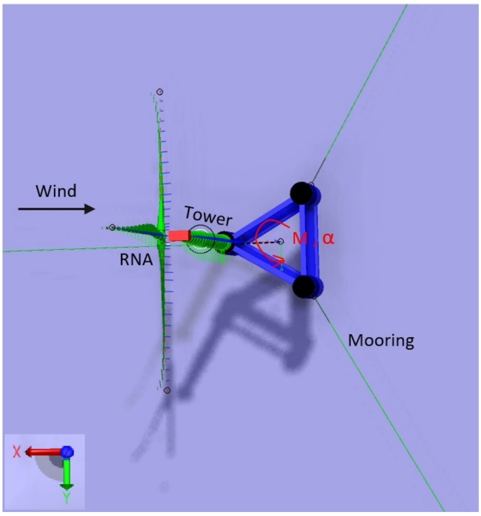
Wind
Tower
RNA
M
α
Mooring
X
Y

Figure 4.9: Bird's eye view of the FWT with wind force acting on it

position, both these contribute to a negative stiffness. The net stiffness in yaw will be a sum of all these stiffness contributions, and the typical curves will be as shown in Figure 4.10.

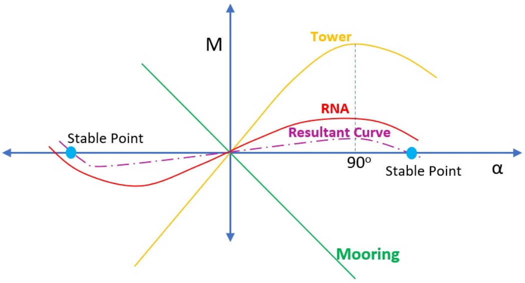
M
Tower
RNA
Resultant Curve
Stable Point
90°
Stable Point
α
Mooring

Figure 4.10: Principle curve showing moments acting on the FWT

The resultant curve intersects the x-axis at relatively far away points from the mean position of 0°. The FWT will be stable at these points, and in between, where the resultant curve is relatively flat to the x-axis, the turbine will oscillate in yaw. If the pretension in the mooring line is increased, then the resultant curve can be modified such that the wind turbine will remain stable near 0°. According to discussions with supervisor Kjell Larsen, the actual shape of these curves is still an area of research in the industry.

4. **Aerodynamic Roll - Yaw Instability**

   This is based on the paper written by Haslum, H. et al. [38].

   This is a relatively new instability phenomenon observed for FWTs. The instability is induced by the turbine thrust force causing anti-symmetric coupling terms in roll and yaw. These coupling forces could cause rigid body roll and yaw oscillations in floaters with a short separation between the uncoupled roll and yaw natural periods [38]. The root cause of this instability was discovered to be a purely aerodynamic phenomenon due to coupling between roll and yaw forces at large thrust force [38].

   To explain this instability, damping forces are required. The damping effects have been seen to reduce the stability margins due to the effect the damping forces have on the relative phase difference between roll and yaw motions [38].

   Aerodynamic stiffness coupling terms

   Considering that the turbine thrust force acts along the positive x-axis, it results in a moment about roll and yaw axes, which may be expressed as stiffness terms K_{46} and K_{64} in the equation of motion [38].

   The thrust force causes a moment in yaw when the FWT heels over in roll, as shown in Figure 4.11(a). This moment is given in the following equation.

   $$F_6 = -F_x \Delta y = F_t \cos(\eta_6) h \sin(\eta_4) \approx F_t h \eta_4 = -K_{64}\eta_4 \tag{4.20}$$

   where $F_x = F_t \cos(\eta_6)$ is the thrust force component in the global x-direction and $\Delta y = h\sin(\eta_4)$ is the moment arm about an earth-fixed z axis. $-K_{64} = F_t h$ is the yaw-roll stiffness term. Similarly, the moment in roll due to a rotation in yaw can be written as follows:

   $$F_4 = -F_y \Delta z = -F_t \sin(\eta_6) h \approx -F_t h \eta_6 = -K_{46}\eta_6 \tag{4.21}$$

   where, $F_y = F_t \sin(\eta_6)$ is the thrust force component in the global y-direction and h is the moment arm about roll axis. This results in roll-yaw coupling term $K_{46} = F_t h$. Thus, stiffness terms are anti-symmetric, which is a requirement for the observed instability.

   Analytical Stability Limit

   The analytical solution is developed for a 2 DoF system including roll and yaw components. It can be said that the system shall be stable if all eigenvalues have negative or zero real part and unstable if any eigenvalue has real

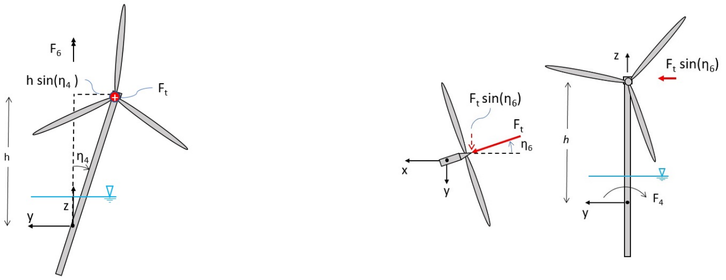

(a) Yaw moment due to roll motion and thrust **(b)** Roll moment due to yaw motion and thrust

Figure 4.11: Moment due to motion and thrust force

part larger than zero [38]. Omitting the damping terms, the eigenvalue for 2 DoF system can obtained as follows:

$$\lambda^2 = \frac{-1}{2}\left(\frac{K_{44}}{M_{44}} + \frac{K_{66}}{M_{66}} \pm \sqrt{\left(\frac{K_{44}}{M_{44}} - \frac{K_{66}}{M_{66}}\right)^2 - \frac{4K_{46}^2}{M_{66}M_{44}}}\right) \tag{4.22}$$

As the thrust force increases the term inside the square root eventually becomes negative, in which case λ^2 becomes a complex number [38]. This results in eigenvalue in the form $\pm(a \pm ib)$, resulting in one stable and one unstable node. Thus, stability requirement when damping forces are omitted is given as follows:

$$\left(\frac{K_{44}}{M_{44}} - \frac{K_{66}}{M_{66}}\right)^2 \geq \frac{4K_{46}^2}{M_{66}M_{44}} \tag{4.23}$$

For systems with lower natural frequency in roll compared to yaw, $\omega_{44} < \omega_{66}$, the stability criteria can be expressed as follows:

$$\frac{\omega_{66}}{\omega_{44}} = \sqrt{\frac{K_{66}M_{44}}{M_{66}K_{44}}} \geq \sqrt{1 + \frac{2h}{K_{44}}\sqrt{\frac{M_{44}}{M_{66}}}F_t} \tag{4.24}$$

This shows that yaw stiffness, K_{66}, will have a higher impact on stability margin than roll stiffness, K_{44} [38]. The requirement for yaw K_{66} can be derived from Equation (4.24) as follows:

$$K_{66} \geq \frac{K_{44}M_{66}}{M_{44}} + 2F_t h\sqrt{\frac{M_{66}}{M_{44}}} \tag{4.25}$$

According to discussions with supervisor Kjell Larsen, this effect is still being studied and is a topic of industry research.

Chapter 5

SIMA Software and Theory

5.1 SIMA Software Package

SIMA is a workbench that offers a complete solution for the simulation and analysis of marine operations [39]. This is developed and owned by SINTEF Ocean. SIMA version 4.1.0 is used for analysis in this thesis work. SIMA consists of two modules, SIMO and RIFLEX, which are explained below in the subsequent sections.

5.2 SIMO

SIMO, an abbreviation for Simulation of Marine Operations, is a time-domain simulation program for studying motions and station keeping of multibody systems. It contains five modules as shown in Figure 5.3.

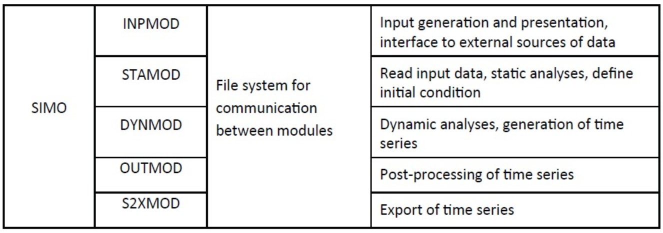

SIMO	INPMOD	File system for communication between modules	Input generation and presentation, interface to external sources of data
	STAMOD		Read input data, static analyses, define initial condition
	DYNMOD		Dynamic analyses, generation of time series
	OUTMOD		Post-processing of time series
	S2XMOD		Export of time series

Figure 5.1: Program modules in SIMO [14]

SIMO solves the equation of motion defined in Equation (4.1) in the time-domain. In order to do this, the frequency-dependent added mass and damping terms must be converted into the time-domain. SIMO performs this using two different methods as described below.

5.2.1 Solution by Convolution Integral

The equation of motion in x-direction can be written as below:

$$\begin{aligned}(m + A(\omega)) \cdot \ddot{x} + C(\omega) \cdot \dot{x} + D_l \cdot \dot{x} + D_q \cdot \dot{x}|\dot{x}| + K(x) \cdot x \\ = q_{cu} + q_{wi}(t) + q^1_{wa}(t) + q^2_{wa}(t) + T\end{aligned} \tag{5.1}$$

where,

$$\begin{aligned} A(\omega) &= A_\infty + a(\omega), \qquad \text{and} \qquad & C(\omega) &= C_\infty + c(\omega), \\ A_\infty &= A(\omega = \infty) & C_\infty &= C(\omega = \infty)\end{aligned} \tag{5.2}$$

The frequency-dependent coefficients, $A(\omega)$ and $C(\omega)$, from the dynamic equilibrium equation 5.1 are transformed from frequency-domain to time-domain using inverse Fourier transform, which results in a retardation function h(τ) as shown in Equation (5.3). The total motion, x, is then solved by numerical integration in the time-domain.

$$\begin{aligned}(m + A_\infty) \cdot \ddot{x} + D_l \cdot \dot{x} + D_q \cdot \dot{x}|\dot{x}| + K(x) \cdot x + \int_0^t h(t-\tau) \cdot \dot{x}\, d\tau \\ = q_{cu} + q_{wi}(t) + q^1_{wa}(t) + q^2_{wa}(t)\end{aligned} \tag{5.3}$$

where,

$$h(\tau) = -\frac{2}{\pi}\int_0^\infty \omega a(\omega) sin(\omega\tau) d\omega = \frac{2}{\pi}\int_0^\infty c(\omega) cos(\omega\tau) d\omega \tag{5.4}$$

The retardation function can be found either by the frequency-dependent added mass or potential damping coefficient. SIMA uses potential damping to estimate the retardation function [40]. A plot of retardation function in surge is shown in Figure 5.2. The frequency-dependent added mass and potential damping can be calculated from the retardation function using the Kramers-Kronig relations [40].

$$\begin{aligned} a(\omega) &= -\frac{1}{\omega}\int_0^\infty h(\tau) sin(\omega\tau) d\tau \\ c(\omega) &= \int_0^\infty h(\tau) cos(\omega\tau) d\tau \end{aligned} \tag{5.5}$$

5.2.2 Separation of Motions

The motions can be split into a high frequency and a low frequency part as an alternative to solving the complete differential equation in the time-domain using

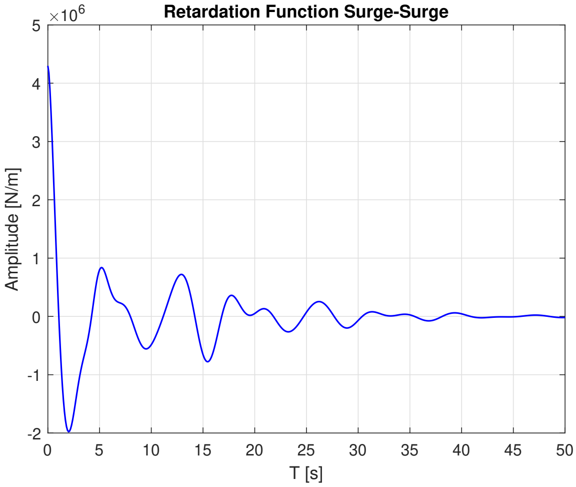

Figure 5.2: Retardation function Surge-Surge from INO WINDMOOR model

the retardation function. The high frequency or wave frequency part can be solved in the frequency-domain, and the low frequency part can be solved in the time-domain. In order to solve the wave frequency motions in the frequency-domain, the motions must be linear responses to the waves. Hence the quadratic damping D_q is to be set as zero and restoring coefficient K as constant.

Similarly, the excitation forces are separated into a high frequency part, $q^{(1)}$, and a low frequency part, $q^{(2)}$ as shown in Equation (5.6).

$$\begin{aligned} q(t, x, \dot{x}) &= q^{(1)} + q^{(2)} \\ q^{(1)} &= q_{WA}^{(1)} \\ q^{(2)} &= q_{WA}^{(2)} + q_{WI} + q_{CU} + q_{ext} \end{aligned} \tag{5.6}$$

The position vector is also separated as follows:

$$x = x_{HF} + x_{LF} \tag{5.7}$$

The WF motions are solved in the frequency-domain and are expressed as follows:

$$(m + A(\omega)) \cdot \ddot{x}_{HF} + (D_l + C(\omega)) \cdot \dot{x}_{HF} + K \cdot x_{HF} = q_{WA}^{(1)}(\omega) \tag{5.8}$$

The first-order wave forces can be described in the frequency-domain as a transfer function between wave elevation and force [41].

$$q_{WA}^{(1)}(\omega) = H^{(1)}(\omega)\tilde{\zeta}(\omega) \tag{5.9}$$

where $H^{(1)}(\omega)$ is the complex first-order transfer function and $\tilde{\zeta}(\omega)$ is the complex harmonic wave component. In the frequency-domain, using Equation (5.9), the first-order transfer function between motion and wave elevation, called as the motion Response Amplitude Operator (RAO), can be established as follows:

$$X_{HF}(\omega) = (-\omega^2(m + A(\omega)) + i\omega D_l + C(\omega) + K)^{-1} H_1(\omega)\tilde{\zeta}(\omega) \tag{5.10}$$

where H_1 is the first-order transfer function between excitation force and wave elevation. A detailed derivation is given in Section 8.1.3. The response spectrum $S_x(\omega)$ can be derived from the wave spectrum $S_\zeta(\omega)$ using the motion RAO as follows:

$$S_x(\omega) = X_{HF}^2(\omega) \cdot S_\zeta(\omega) \tag{5.11}$$

The LF motions are solved in time-domain and the dynamic equilibrium equation is expressed as follows:

$$\begin{split}(m + A(\omega = 0)) \cdot \ddot{x}_{LF} + (D_l + D_q \cdot |\dot{x}_{LF}|) \cdot \dot{x}_{LF} + K(x_{LF}) \cdot x_{LF} \\ = q_{WA}^{(2)} + q_{WI} + q_{CU} + q_{ext}\end{split} \tag{5.12}$$

5.3 RIFLEX

RIFLEX is a computer program used to analyse flexible risers and other slender structures, such as mooring lines, fish cage systems, pipelines, conventional steel risers etc., and implements a non-linear Finite Element Method (FEM) for analysing the slender structures [42]. RILFEX program system consists of four programs or modules communicating via the file system, as shown in the figure below [15].

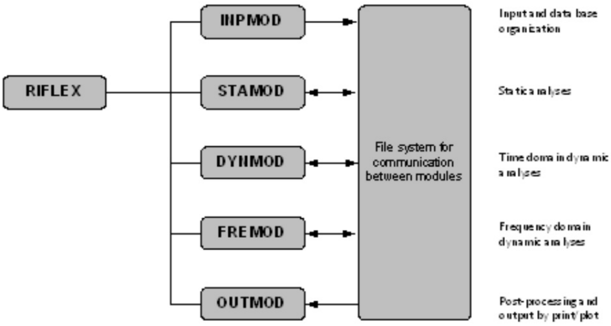
RIFLEX
INPMOD
STAMOD
DYNMOD
FREMOD
OUTMOD
File system for communication between modules
Input and data base organization
Static analyses
Time domain dynamic analyses
Frequency domain dynamic analyses
Post-processing and output by print/plot

Figure 5.3: Program modules in RIFLEX [15]

The time-domain analysis using a coupled SIMO-RIFLEX model for the mooring system can be carried out in two different ways, as explained in Section 5.4.

5.4 Coupled and Uncoupled Analysis

This section is based [16].

In SIMA, the FWT and mooring system simulations can be numerically estimated using two alternative methods. One approach is to do an uncoupled or separated analysis where the total motions of the large volume body is calculated in SIMO. In this approach, the stiffness $K(x)$ is obtained from the modelled catenary lines in SIMO, and additional damping from mooring lines is included in separate damping matrices [16]. The total motions and quasi-static line tensions are estimated in SIMO. The total motions from SIMO are exported as top end motion into RIFLEX, which then calculates the total line tensions using the slender FEM model and estimates the total dynamic line tensions. This approach is illustrated in Figure 5.4.

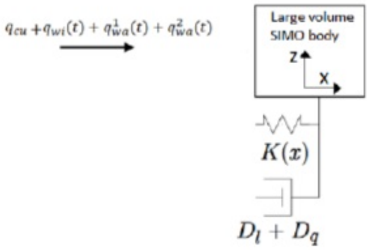

(a) Large volume SIMO body

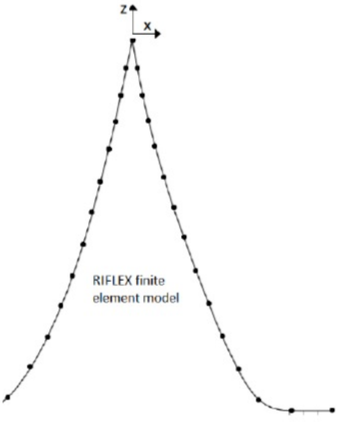

(b) Slender RIFLEX model

Figure 5.4: Separated Analysis [16]

The second approach is to perform a coupled analysis where the large volume SIMO body and slender RIFLEX model are solved simultaneously, as shown in Figure 5.5. In this approach, for each time step, the SIMO results are imported to RIFLEX, and the mooring line's responses and stresses are calculated. The stiffness matrix will also be updated for each time step. The total motion, x, can be solved only by numerical integration in the time-domain using retardation functions.

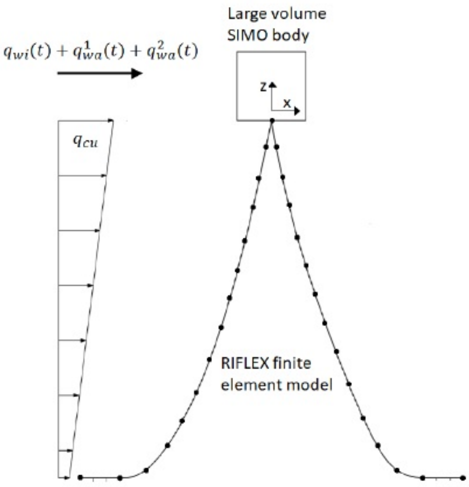

Figure 5.5: Coupled Analysis [16]

In this thesis, a coupled analysis is performed, and the complete equation of motion is solved by the method of convolution integral and retardation functions.

5.5 Estimation of Extreme Response from Time Domain Simulations

The results from time-domain simulations in SIMA are obtained as time series. The characteristic values of different responses are obtained from these time series using extreme value statistics. The Gumbel distribution is often well suited to model the extreme value distribution, and the extreme value shall be estimated as the MPM value of the extreme value distribution for the required response parameter.

For a wind turbine, the simulation for estimating extreme events using stochastic wind fields and/or irregular sea states requires a simulation time of 1 hour [4]. The MPM can be estimated from a time-domain analysis either through one long simulation and establishing a peak distribution from the same or by simulating several simulations of 1 hour duration and establishing an extreme value distribution from the individual maxima of each simulation. In the former method, the peak can be fitted into a Weibull distribution, while in the latter approach, the maxima can be fitted into a Gumbel distribution. These are shown in Figure 5.6.

The MPM value of the Gumbel distributions corresponds to the 37% percentile, i.e., 63% probability of exceedance [43].

The probability density function for the Gumbel distribution with location parameter μ and scale parameter σ is

$$y = f(x|\mu,\sigma) = \frac{1}{\sigma}\exp\left(-\frac{x-\mu}{\sigma}\right)\exp\left[-\exp\left(-\frac{x-\mu}{\sigma}\right)\right] \tag{5.13}$$

where x is the response of interest.

For mooring line tension, characteristic dynamic tension $T_{c,\,dyn}$ is equal to the MPM value from Gumbel distribution. The characteristic mean tension, $T_{c,\,mean}$ will be obtained as the mean of means.

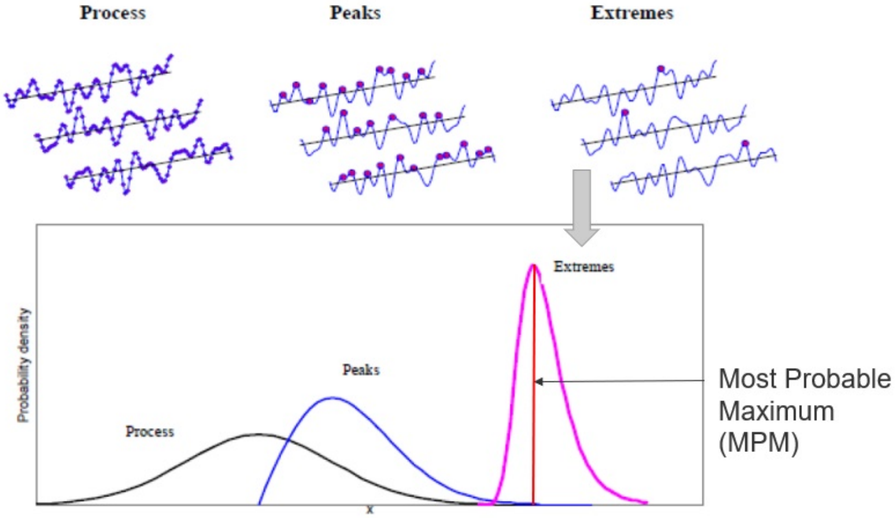

Figure 5.6: Illustration of Peak and Maxima Distribution [17]

Chapter 6

12MW Floating Wind Turbine Model

6.1 Modelling of FWT in SIMA

An FWT can be modelled in multiple ways in SIMA. Each approach has its advantages and disadvantages, as explained below.

1. **SIMO body for both the floater and RNA with Catenary Mooring Lines**

   In this model, the tower is defined using slender elements in SIMO, and the rotor and floater are connected using a stiff coupling. This model can obtain results from WAMIT as input and has multiple options available for force models. Only a quasi-static mooring analysis can be carried out using this model, and it underestimates the dynamic effects in the mooring lines.

2. **SIMO body for the floater with Drag Element in SIMO for RNA**

   This is a simplified version of the model described above. The difference between these two models is that instead of modelling the rotor as a SIMO body, a drag element from SIMO is used to model the RNA. The drag coefficients for the drag element in this model shall be calibrated w.r.t a fully modelled SIMO or RIFLEX RNA. This model is suitable when numerous simulations are to be carried out, mainly during fatigue calculations.

3. **Fully RIFLEX model**

   This is a fully dynamic finite element based RIFLEX model where the floater, tower, RNA and mooring lines are modelled in RIFLEX. It is an advanced model compared to the above two models. This model can calculate the total dynamic line tensions in the mooring lines and capture the dynamic effects better than the first model. However, in this model, the force options for the floater are limited to Morison formulation.

4. **Coupled SIMO-RIFLEX model with SIMO body for the floater and RIFLEX Mooring Lines**

   This is an advanced model, where a SIMO body is used for the floater, and a RIFLEX model is used for the tower, RNA and mooring lines. Multiple options for the force model come from the SIMO floater. A finite element-based formulation of the mooring lines can calculate the total dynamic line tensions in the mooring lines and capture the dynamic effects completely. This thesis uses a coupled model to analyse hybrid mooring lines.

6.2 Description of INO WINDMOOR Floating Substructure

This section is based on [5, 20].

INO WINDMOOR is a 4-year competence building project funded by the Research Council of Norway and the offshore wind industry [44]. It is a 12MW FWT with a semi-submersible substructure. The semi-submersible floating platform has three columns connected by pontoons and deck beams. The wind turbine is placed on top of one of the columns, as shown in Figure 6.1. This platform was jointly designed by Inocean and Equinor.

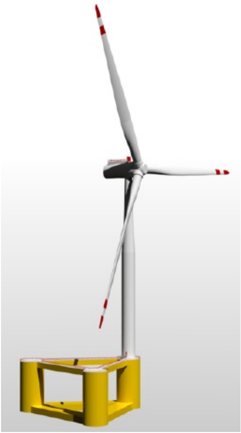

Figure 6.1: Concept of WINDMOOR 12 MW FWT [5]

As this thesis is a continuation of the specialisation project carried out in Autumn 2021, the same SIMO model has been used. All hydrodynamic analyses of the platform carried out using WAMIT had been provided as an input and were included in the SIMO Model. The motion RAOs were additionally provided by Petter Andreas Berthelsen of SINTEF Ocean. The SIMO model, various hydrodynamic coefficients and the force and motion transfer functions are described in the subsequent sections.

6.2.1 Coordinate System

An earth fixed global coordinate system and a body-fixed local coordinate system is defined for the model.

Global coordinate system

The global coordinate system has the X-Y plane coinciding with the mean water level. Z-axis is positive upwards. The direction of incident waves, wind, and currents are defined in negative X-direction. Global coordinate system is shown in Figure 6.2(a).

Local coordinate system

The platform has its local coordinate system located at its geometric centre on the mean water level. The local coordinate system is fixed to the body and moves along with the body. Local motions and response calculations are made w.r.t the local coordinate system. Local coordinate system is shown in Figure 6.2(b).

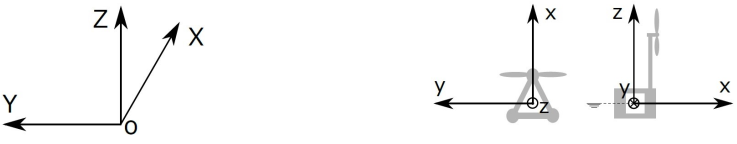

(a) Global coordinate system

(b) Local coordinate system

Figure 6.2: Coordinate System [5]

6.2.2 Main Particulars

The principal particulars of the hull and its inertia properties with ballast are defined in Table 6.1. The radii of gyration of the substructure refer to the hull Centre of Gravity (CoG) and the total radii of gyration refer to the FWT CoG, considering the turbine's CoG at the tower centre. The floating properties include the wind turbine.

Table 6.1: Main Particulars for INO WINDMOOR FWT [5]

Property	Unit	Value
Column Diameter	m	15.00
Column height	m	31
Pontoon width	m	10
Pontoon height	m	4
Center-center distance	m	61
Deck beam width	m	3.5
Deck beam height	m	3.5
Total substructure mass	t	11974
Total substructure CG_x	m	-5.91
Total substructure CG_z	m	-9.7
Total substructure R_{xx}	m	23.66
Total substructure R_{yy}	m	8.63
Total substructure R_{zz}	m	8.1
Displacement	t	14176.1
Draft	m	15.5
$CG_x^{1)}$	m	[-0.37,0.37]
$CG_y^{1)}$	m	[-0.37,0.37]
CG_z	m	4.23
R_{xx}	m	43.67
R_{yy}	m	44.18
R_{zz}	m	30.26

$^{1)}$ CG_x and CG_y are dependent on the nacelle orientation.

6.2.3 Mass Matrix

The mass matrix is provided in the SIMO model. This considers the structural mass of the semi-submersible and the tower. This is shown in Table 6.2. However, when modelling a coupled SIMO-RIFLEX model, the tower is modelled as a slender element, and hence the mass matrix is modified to include only the structural mass for the semi-submersible without the tower.

Table 6.2: Mass properties for Semi and Tower from SIMO model

Property	Unit	Value
Mass	kg	$1.3139 \cdot 10^7$
I_{xx}	kg m^2	$1.6741 \cdot 10^{10}$
I_{yy}	kg m^2	$1.7425 \cdot 10^{10}$
I_{zz}	kg m^2	$1.1323 \cdot 10^{10}$

6.2.4 Infinite Frequency Added Mass Matrix

The added mass at infinite frequency is estimated from WAMIT and is given as an input in the SIMO model. This matrix is shown below.

$$\begin{bmatrix} 5.41e+06 & 0.0 & -93.04 & 0.0 & -3.05e+07 & 0.0 \\ 0.0 & 5.41e+06 & 0.0 & 3.05e+07 & 0.0 & 646.97 \\ -24.95 & 0.0 & 1.98e+07 & 0.0 & 3137.8 & 0.0 \\ 0.0 & 3.05e+07 & 0.0 & 5.87e+09 & 0.0 & 9288.1 \\ -3.05e+07 & 0.0 & 4053.8 & 0.0 & 5.87e+09 & 0.0 \\ 0.0 & 610.06 & 0.0 & 16903 & 0.0 & 5.46e+09 \end{bmatrix}$$

Using the equations explained in Section 5.2.1, the frequency-dependent added mass is calculated using the added mass at infinite frequency and the retardation function included in SIMO.

6.2.5 Linear Damping Matrix

When importing the WAMIT results into SIMO, SIMA calculates the retardation function using frequency-dependent radiation damping as given in Equation (5.4). This calculation produces a residual value which is included as a constant damping matrix. This is shown in the matrix below.

$$\begin{bmatrix} 1442.2 & 0.0 & 0.0 & 0.0 & 0.0 & 0.0 \\ 0.0 & 1442.2 & 0.0 & 0.0 & 0.0 & 0.0 \\ 0.0 & 0.0 & 1.5018e+06 & 0.0 & 0.0 & 0.0 \\ 0.0 & 0.0 & 0.0 & 7.0073e+08 & 0.0 & 0.0 \\ 0.0 & 0.0 & 0.0 & 0.0 & 7.0073e+08 & 0.0 \\ 0.0 & 0.0 & 0.0 & 0.0 & 0.0 & 2.61e+06 \end{bmatrix}$$

6.2.6 Hydrostatic Stiffness

The hydrostatic stiffness matrix contains the contribution due to volume variation caused by small motions around equilibrium positions. This is applicable for heave, roll and pitch DoFs. This is shown in the stiffness matrix given below.

$$\begin{bmatrix} 0.0 & 0.0 & 0.0 & 0.0 & 0.0 & 0.0 \\ 0.0 & 0.0 & 0.0 & 0.0 & 0.0 & 0.0 \\ 0.0 & 0.0 & 5.33 \cdot 10^6 & 0.0 & 0.0 & 0.0 \\ 0.0 & 0.0 & 0.0 & 3.38 \cdot 10^9 & 0.0 & 0.0 \\ 0.0 & 0.0 & 0.0 & 0.0 & 3.38 \cdot 10^9 & 0.0 \\ 0.0 & 0.0 & 0.0 & 0.0 & 0.0 & 0.0 \end{bmatrix}$$

6.2.7 Force Transfer Functions

The transfer functions for first-order wave and wave drift forces are calculated using a linear-diffraction analysis in WAMIT and are included in the SIMO model.

The first-order wave force transfer functions for surge, heave and pitch at 0° wave heading is shown in Figure 6.3.

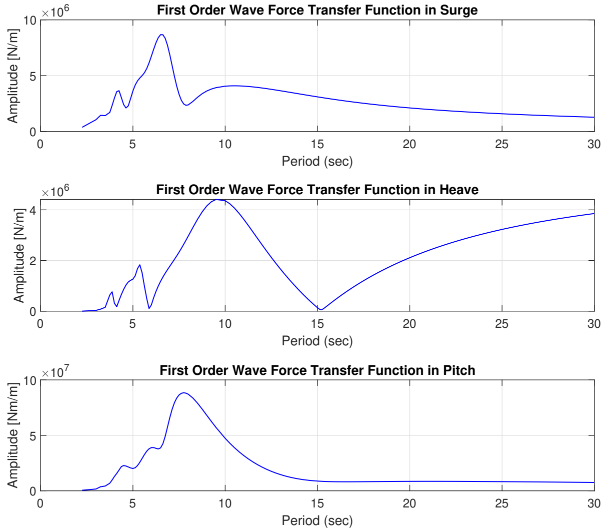

Figure 6.3: First-order wave force transfer function in Surge, Heave and Pitch

From Figure 6.3, we see that the resonance period in Surge is around 6.5 s. Similarly, we can see that the resonance period in heave and pitch are around 10 s and 8 s, respectively. The mean wave drift coefficient in surge is shown in Figure 6.4. The first-order wave force transfer function for all 6 DoFs and different wave headings is provided in Appendix A.

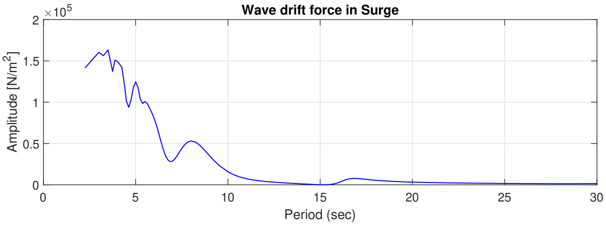

Figure 6.4: Wave drift force in Surge

6.2.8 Motion Transfer Functions

RAOs describe the response of a structure to wave frequency excitation. It provides the response of a structure in a given DoF due to unit wave amplitude in that DoF. The RAOs for the INO WINDMOOR turbine are calculated using WAMIT and included in the SIMA model. The RAOs in Surge, Heave and Pitch at 0° wave heading are shown in Figure 6.5.

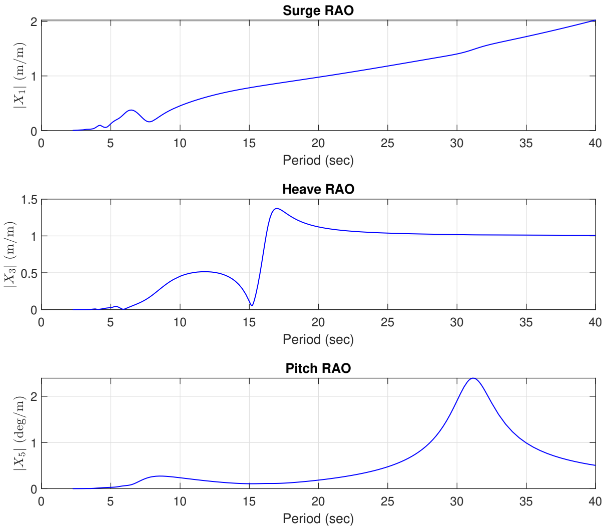

Figure 6.5: RAOs in Surge, Heave and Pitch at the waterplane for 0° wave heading

The RAO plots show that the heave natural period occurs at around 16 s and the pitch natural period occurs at around 31 s. The RAO plots for all 6 DoFs at different wave headings in provided in Appendix B.

6.2.9 Slender Elements

Slender elements were newly defined for the pontoons and columns in the SIMO model to account for the viscous forces and damping. The drag coefficients for the pontoons were calculated from Table E-1 given in Appendix E of DNV-RP-C205 Environmental conditions and environmental loads [18].

For the pontoons of the semi-submersible with rectangular cross section, the drag coefficient in y direction (CD_y) was obtained as 2.35 from case 2 defined in Table E-1 with T/D = 0 and L/D = 0.4. The drag coefficient in z direction (CD_z) has been calculated as 1.4 based on extrapolation of case 2 with T/D = 0 and L/D =

2.5. The dimensions are marked in Figure 6.6.

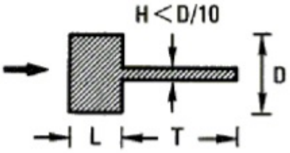

Figure 6.6: Rectangle with thin splitter plate - Case 2 in Table E-1 [18]

The quadratic drag in y and z directions for the pontoon is calculated as shown in Equations (6.1a) and (6.1b).

$$C2y = \frac{1}{2} \cdot \rho_{\text{sea water}} \cdot CD_y \cdot h = \frac{1025}{2} \cdot 2.35 \cdot 4 = 4817.5 Ns^2/m^3 \tag{6.1a}$$

$$C2z = \frac{1}{2} \cdot \rho_{\text{sea water}} \cdot CD_z \cdot w = \frac{1025}{2} \cdot 1.4 \cdot 10 = 7175.0 Ns^2/m^3 \tag{6.1b}$$

where $\rho_{\text{sea water}}$ is the density of sea water and h and w are the pontoon's height and width, respectively.

For the columns with circular cross section, the drag coefficient in y and z directions (CD_y & CD_z) were obtained as 1.00 from case 14 defined in Table E-1 with D/L = 1.00. The dimensions are marked in Figure 6.7.

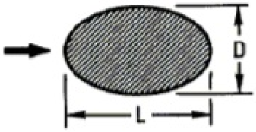

Figure 6.7: Ellipse - Case 14 in Table E-1 [18]

The quadratic drag in the y and z directions for the column is calculated as shown in Equations (6.2a) and (6.2b).

$$C2y = \frac{1}{2} \cdot \rho_{\text{sea water}} \cdot CD_y \cdot D = \frac{1025}{2} \cdot 1.0 \cdot 15 = 7687.5 Ns^2/m^3 \tag{6.2a}$$

$$C2z = \frac{1}{2} \cdot \rho_{\text{sea water}} \cdot CD_z \cdot D = \frac{1025}{2} \cdot 1.0 \cdot 15 = 7687.5 Ns^2/m^3 \tag{6.2b}$$

where D is the diameter of the column.

6.2.10 Mooring System

Existing Mooring System

The existing model had a mooring system provided by Inocean consisting of three catenary mooring lines with a combination of studless chains and polyester ropes with a pretension of 1050 kN and designed for a water depth of 150 m.

The fairlead and anchor point locations to which the mooring lines were connected are given in Table 6.3.

Table 6.3: Fairlead and Anchor Coordinates of existing Mooring System [5]

	Fairlead			Anchor			
Mooring Line	x (m)	y (m)	z (m)	x (m)	y (m)	z (m)	Azimuth (deg)
ML1	42.7	0.0	0.0	700.0	0.0	-150.0	180
ML2	-21.4	37.0	0.0	-350.0	606.2	-150.0	300
ML3	-21.4	-37.0	0.0	-350.0	-606.2	-150.0	60

The natural time period of the FWT in 6 DoFs is estimated using the free decay test for the existing model. This is given in Table 6.4.

Table 6.4: FWT rigid-body natural periods [5]

	Surge	Sway	Heave	Roll	Pitch	Yaw
Natural Period (s)	97.3	98.0	16.3	29.5	31.4	88.0

Determination of Base Case Mooring System

To establish a base case model, the existing mooring system was replaced with a catenary mooring system with three mooring lines consisting of only chain segments. The new mooring system was defined for a water depth of 100 m with a pretension of 1250 kN as shown in Figure 6.8.

Furthermore, different models were also defined with mooring systems using synthetic ropes and a hybrid mooring system with clump weights to study and compare different mooring system concepts. Different mooring concepts that have been studied are described in Chapter 7.

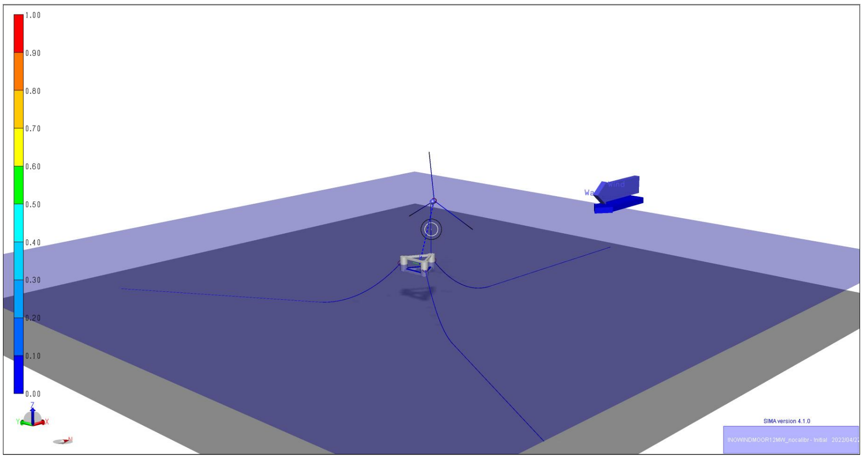

Figure 6.8: SIMO model with base case mooring system

6.2.11 Coupled SIMO-RIFLEX Model

SIMO model can perform only quasi-static analysis of the mooring lines. However, the dynamics could be important and to capture the dynamic effect of mooring lines, it has been modelled in RIFLEX, and a coupled analysis is performed. As mentioned in Section 5.3, RIFLEX implements a non-linear FEM for analysing the slender structures such as the mooring lines.

The coupled SIMO-RIFLEX model was provided by Professor Erin Bachynski-Polić of the Department of Marine Technology, NTNU, for the course project in TMR03 Integrated Dynamic Analysis of Wind Turbines in Autumn 2021. The same model has been used in this thesis.

The substructure and the nacelle are retained as a SIMO body, while the tower, blades, shaft and mooring lines are modelled as a slender system in RIFLEX. The wind turbine is also modelled as a slender system in RIFLEX as the same cannot be modelled as a SIMO body in a coupled SIMO-RIFLEX model.

Modelling Slender System in RIFLEX

Supernodes must be defined to model a slender system such as a mooring line in RIFLEX. A line can be modelled in RIFLEX only between two supernodes. Supernodes are locations with specified boundary conditions. The constraints at a supernode can be set either as free, fixed, or slaved. Any line defined in RIFLEX has to be of a specific line type. The line type contains information on different segments in a line and the number of elements in each segment. Multiple cross-sectional properties can be defined to include multiple segments in the same line type, and each segment shall be associated with a cross-section.

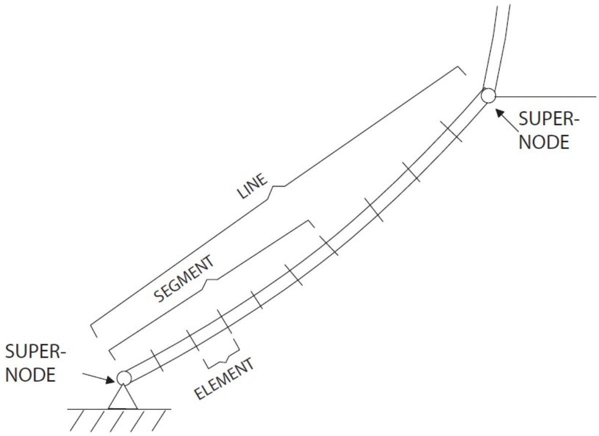
SUPER-
NODE
LINE
SEGMENT
SUPER-
NODE
ELEMENT

Figure 6.9: Modelling Slender System in RIFLEX [15]

The SIMO body and the RIFLEX slender system are coupled using a slender system connection at the nacelle. The resultant coupled model with the base case mooring system in its initial configuration before static equilibrium is shown in Figure 6.10.

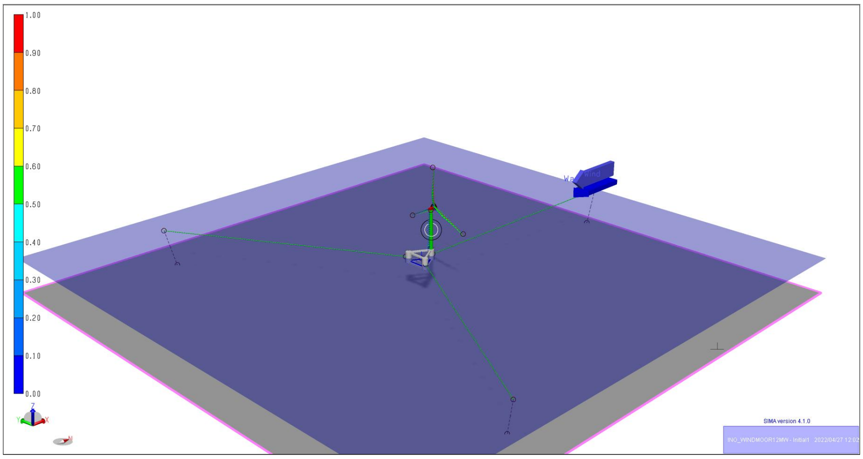
1.00
0.90
0.80
0.70
0.60
0.50
0.40
0.30
0.20
0.10
0.00
SIMA version 4.1.0
INO_WINDMOOR12MW - Initial1 2022/04/27 12:02

Figure 6.10: Coupled SIMO-RIFLEX model with base case mooring system

Chapter 7

Mooring Concepts

This chapter describes the various mooring concepts studied in this thesis. As mentioned in Section 6.2.10, a base case mooring system is defined using pure chain elements. To understand the effect of synthetic ropes, a hybrid mooring system with chain segments at the top and bottom end and polyester rope in between is considered. In addition to this, clump weights are also introduced into this hybrid system to study the effect of clump weights on line tension and platform offsets. Finally, the polyester segment is replaced with nylon, and the mooring concept is studied. The location of fairleads is the same as defined in Table 6.3 and remains constant for all the mooring concepts explained in the subsequent sections. Similarly, the mooring line length, the number of mooring lines, pretension and the water depth are treated as constant for all mooring system concepts. A top view of a typical mooring system is shown in Figure 7.1.

Table 7.1: Constant Parameters for all concepts

Parameter	Value
Mooring line length	700 m
Number of mooring lines	3
Water Depth	100 m
Pretension	≈ 1250 kN

7.1 Pure Chain System

This is the base case system defined for this thesis as explained in Section 6.2.10. This concept consists of a catenary mooring system using three mooring lines. The mooring lines consist of only chain segments of uniform cross-section throughout.

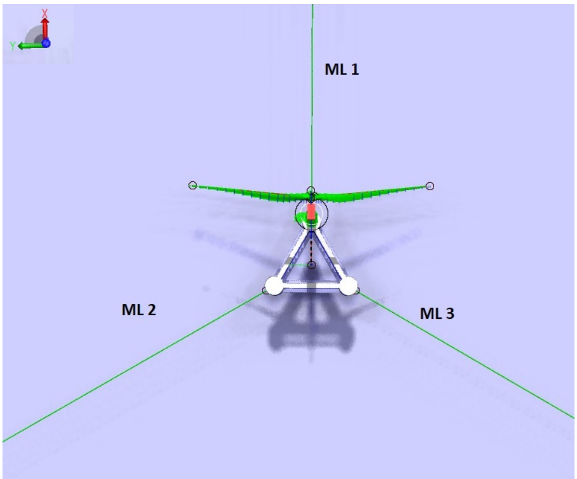

Figure 7.1: Top view of a typical mooring system in SIMO-RIFLEX Coupled model

The properties of the chain were obtained from the technical brochure issued by Ramnäs [45].

An R4 grade studless chain with a diameter of 157 mm and a Minimum Breaking Load (MBL) of 21234 kN is used for the mooring lines. The elastic modulus for the R4 grade studless chain is calculated as $5.0575 \cdot 10^{10}$ N/m^2 from Section 2.1.8 of DNV-OS-E301 Position Mooring [43]. The weight of the chain in the air is obtained as 493 kg/m. The submerged weight of the mooring chain is calculated as shown in Equation (7.1).

$$\begin{aligned}\text{Submerged Weight} &= \frac{\rho_{\text{Steel}} - \rho_{\text{Seawater}}}{\rho_{\text{Steel}}} \times \text{Weight of chain in air} \\ &= \frac{7850 - 1025}{7850} \times \text{Weight of chain in air} \\ &= 0.87 \times \text{Weight of chain in air}\end{aligned} \tag{7.1}$$

where ρ_{Steel} and ρ_{Seawater} are the densities of steel and sea water respectively. The mooring line length was considered 700 m for the base case and was assigned a pretension of 1250 kN. Marine growth is not accounted for in the base case. The studless chain's transverse and longitudinal drag coefficients were obtained as 2.4 and 1.15 respectively from Table 1-1 in Section 2.7 of DNV-OS-E301 Position Mooring [43]. The mooring chain properties are summarized in Table 7.2.

The static configuration of Mooring Line 1 (ML 1) in the X-Z plane is shown in

Table 7.2: Properties of Mooring Chain

Property	Value
Grade	R4
Diameter	157 mm
MBL	21234 kN
Weight in air	493 kg/m
Submerged Weight	428.91 kg/m
Axial Stiffness (EA)	1.96E+09 N
Transverse Drag Coefficient	2.4
Longitudinal Drag Coefficient	1.5

Figure 7.2.

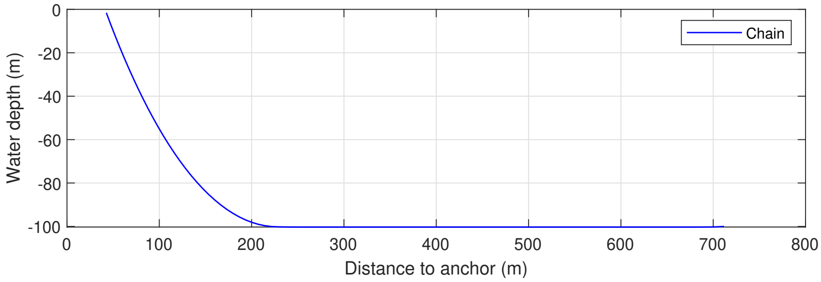

Figure 7.2: Static configuration of ML 1 in X-Z plane for Pure Chain System

7.2 Chain - Polyester - Chain System

The Chain-Polyester-Chain (CPC) concept has a hybrid mooring line consisting of 20 m of chain segments at the top and bottom and 660 m of polyester rope in between. The top and bottom end of a mooring line rub against the substructure and seabed and are subjected to wear and tear. As mentioned in Section 2.2.1, the chain has good abrasion characteristics compared to synthetic ropes and is provided at both ends. This hybrid mooring system with three mooring lines forms a taut moored system.

The chain used in this concept is the R4S grade chain with the same diameter and weight in air defined in Table 7.2. The MBL of the chain is 23559 kN. The polyester mooring line is modelled using the Superline Polyester used for permanent mooring developed by Bridon [46]. Based on the discussions with supervisor Kjell Larsen, the polyester line was chosen such that the MBL of this line was in the same order as that of the chain segments considered. Accordingly, a polyester segment with a nominal diameter of 291 mm and MBL of 23544 kN was considered. The drag coefficient for fibre rope was obtained from Table 1-1 in Section 2.7 of DNV-OS-E301 Position Mooring [43]. The properties of the chain and polyester segments are given in Table 7.3.

Table 7.3: Properties of Mooring Chain and Polyester Segments

Property	Chain	Polyester
Type	R4S Grade	Permanent Mooring
Diameter	157 mm	291 mm
MBL	23559 kN	23544 kN
Weight in air	493 kg/m	54.7 kg/m
Transverse Drag Coefficient	2.4	1.6
Longitudinal Drag Coefficient	1.5	-

The distance to anchor for the mooring line is found through an iterative process such that the pretension remains similar compared to the pure chain system described in Section 7.1. The static configuration of ML 1 in the X-Z plane is shown in Figure 7.3.

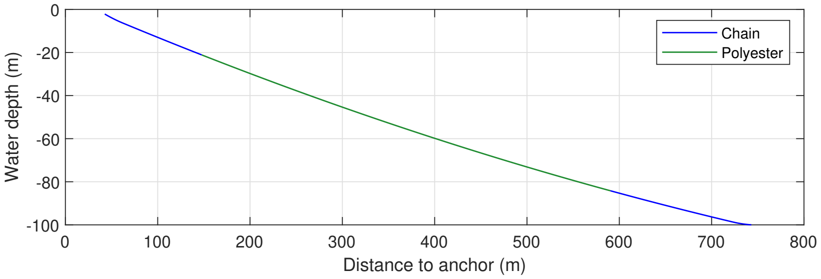

Figure 7.3: Static configuration of ML 1 in X-Z plane for CPC System

7.2.1 Non-Linear Stiffness model for Polyester Mooring Line

The non-linear stiffness model for synthetic ropes discussed in Section 2.5.1 is implemented for the polyester mooring line. The non-linear stiffness model can be represented through the working curve as given in Equation (2.15). Using the constants for the polyester mooring line given in Table 2.2, the equation can be re-written as follows:

$$\frac{T_{mean}}{MBL} = \frac{3}{0.6 \cdot 100} \cdot [exp(0.6 \cdot 100 \cdot \varepsilon_{mean}) - 1] = 0.05 \cdot [exp(60 \cdot \varepsilon_{mean}) - 1] \quad (7.2)$$

The working curve used for the static analysis of the chosen polyester line is shown below.

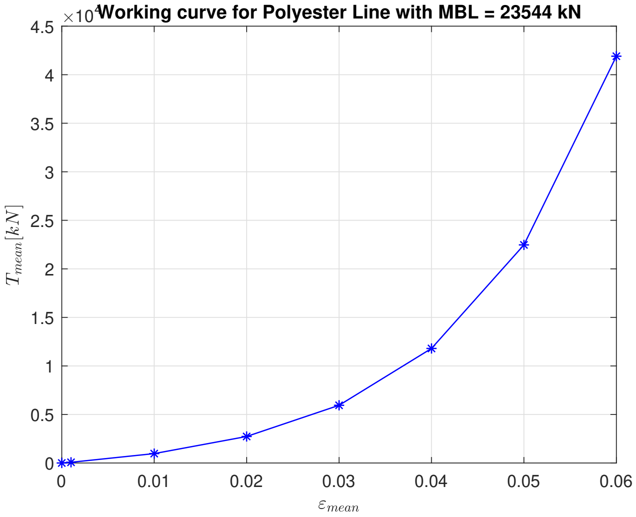

Figure 7.4: Working curve for polyester line with MBL 23544 kN

7.3 Chain - Polyester - Chain System with Clump Weights

Various studies have been conducted to understand the influence of additional elements such as buoys and clump weights on mooring lines. A numerical study conducted by Yuan, Z. et al. [47] on a hybrid mooring system with clump weights and buoys for a semi-submersible based oil and gas asset found that the line tension could be reduced by using the hybrid mooring lines. The motion responses were, however, hardly influenced. A recent study conducted by Bruschi, N. et al. [48] on the influence of clumps-weighted moorings on a spar type offshore wind turbine found that both the platform response and mooring line tension are affected by adding clump weights to the mooring lines. To understand this effect further on a semi-submersible substructure for an FWT, a CPC system with clump weight is studied.

This concept uses the same line configuration as defined in Section 7.2. Clump weights are added to the mooring lines so that system becomes a little software compared to the taut system. The total stiffness of the line will be a combination of elastic and geometric stiffness. During the discussions with supervisor Kjell Larsen, it was understood that there are different ways to design clump weights.

One method is to use mono-cast steel boxes that are attached to chain links. This is shown in Figure 2.9. Another method is to use short chain segments in parallel, connected with triplates at the ends.

The second method is used to model the clump weight system in SIMA. The clump weight is introduced at a length of 200 m from the top end of the mooring line. A chain length equivalent to a clump weight with 21.8 T submerged weight is introduced in the mooring system with a CPC configuration. The drag coefficient for the studless chain is obtained from DNV-OS-E301 Position Mooring [43]. The distance to anchor for the mooring line is found through an iterative process such that the pretension remains similar compared to the pure chain system described in Section 7.1. The static configuration of ML 1 in the X-Z plane is shown in Figure 7.5.

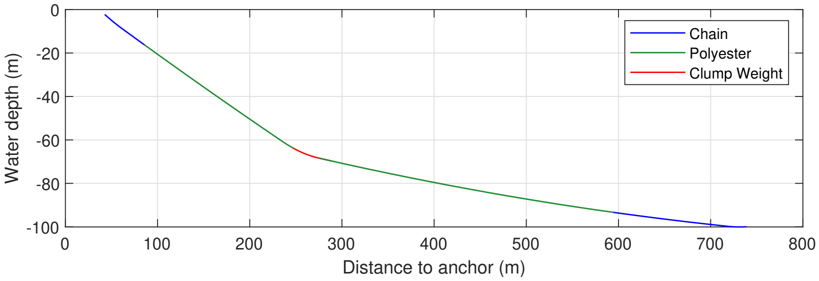

Figure 7.5: Static configuration of ML 1 in X-Z plane for CPC System with Clump Weight

7.4 Chain - Nylon - Chain System

The Chain-Nylon-Chain (CNC) concept also has a hybrid mooring system with 20 m of chain segments at the top and bottom ends and 660 m of nylon rope in between. This mooring system also forms a taut moored system with three mooring lines.

The chain used in this concept is the same as defined for the CPC system in Section 7.2. This nylon rope is modelled using Superline Nylon OCIMF 2000 developed by Bridon [46]. The analysis performed on this system determined that maintaining the MBL of the nylon segment in the same order as that of the chain is a highly conservative approach. Furthermore, based on the discussion with supervisor Kjell Larsen, it was understood that nylon was more expensive than polyester; hence, using an oversized nylon segment would have cost implications. Accordingly, the MBL of the nylon rope was selected as 16000 kN. The largest nylon mooring line developed by Bridon has an MBL of 11507 kN [46]. As this MBL was insufficient for this concept, the nylon rope is up-scaled to have a larger MBL. Figures 7.6 and 7.7 depicts how the MBL and weight per unit length are calculated from the Bridon nylon line [46].

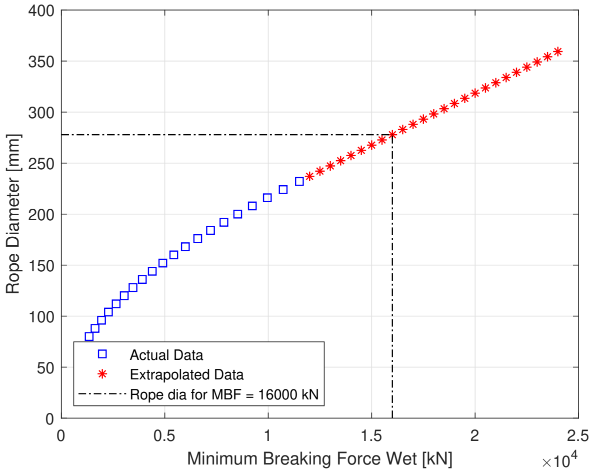

Figure 7.6: Extrapolation of rope diameter for required MBL

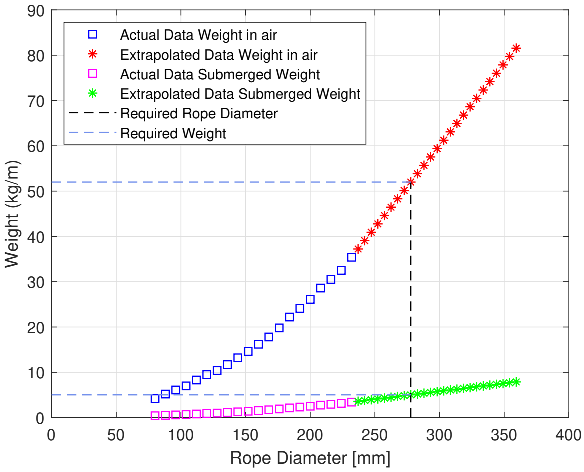

Figure 7.7: Extrapolation of weight per unit for calculated rope diameter

From Figure 7.6, it can be seen that for a required MBL of 16000 kN, the rope diameter can be extrapolated as 277.8 mm. Similarly, from Figure 7.7, it can be seen that for a rope diameter of 277.8 mm, the weight in air is 52 kg/m, and the submerged weight is 5.023 kg/m. The drag coefficient for fibre rope was obtained from Table 1-1 in Section 2.7 of DNV-OS-E301 Position Mooring [43]. The properties of the chain and nylon segments are given in Table 7.4.

Table 7.4: Properties of Mooring Chain and Nylon Segments

Property	Chain	Nylon
Type	R4S Grade	Permanent Mooring
Diameter	157 mm	277.8 mm
MBL	23559 kN	16000 kN
Weight in air	493 kg/m	52 kg/m
Transverse Drag Coefficient	2.4	1.6
Longitudinal Drag Coefficient	1.5	-

Similar to the previous concepts, the distance to anchor for the mooring line is found through an iterative process. The static configuration of ML 1 in the X-Z plane is shown in Figure 7.8

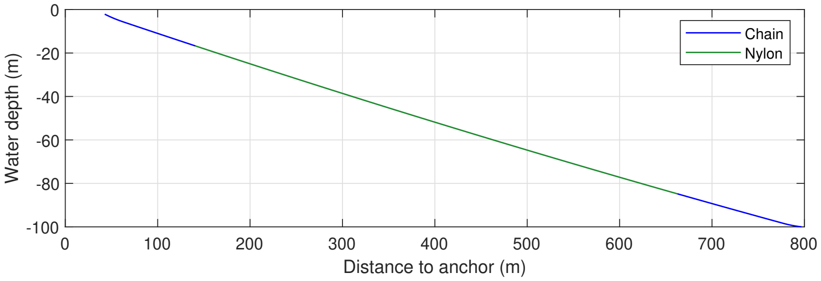

Figure 7.8: Static configuration of ML 1 in X-Z plane for CNC System

7.4.1 Non-Linear Stiffness model for Nylon Mooring Line

As explained in Section 7.2.1, similar to the polyester line, a non-linear stiffness model is implemented for the nylon line. Using the coefficients for nylon rope given in Table 2.2, the working curve for nylon rope shall be calculated as shown below.

$$\frac{T_{mean}}{MBL} = \frac{0.2}{0.26 \cdot 100} \cdot [exp(0.26 \cdot 100 \cdot \varepsilon_{mean}) - 1] = 0.0077 \cdot [exp(26 \cdot \varepsilon_{mean}) - 1] \tag{7.3}$$

The working curve used for static analysis of the nylon rope for the selected MBL is shown in Figure 7.9.

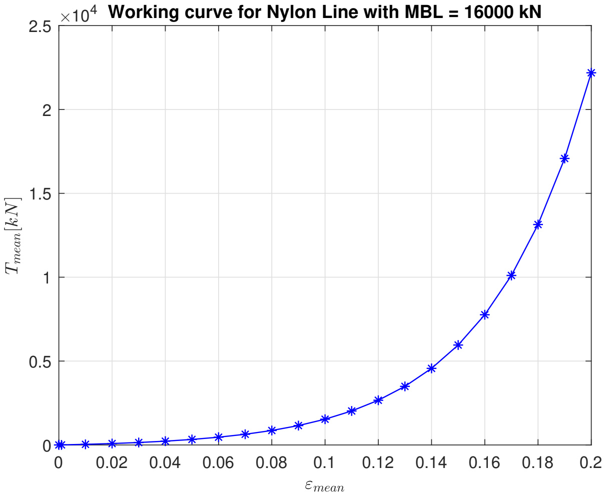

Figure 7.9: Working curve for nylon line with MBL 16000 kN

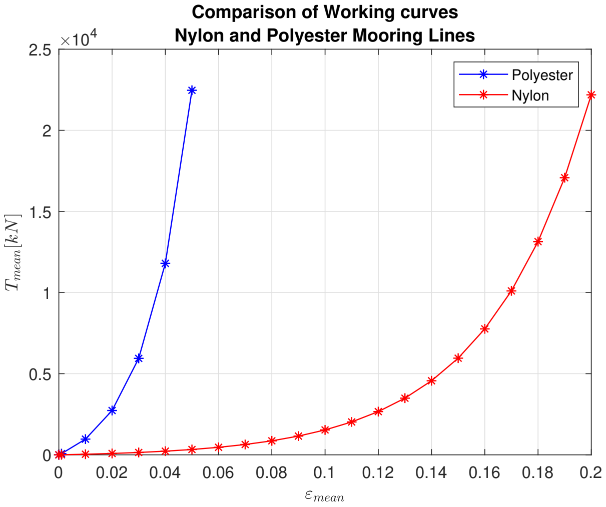

Figure 7.10: Comparison of working curves for polyester and nylon mooring lines

Figure 7.10 shows the comparison of working curves of polyester and nylon mooring lines. From the figure, it can be understood that the nylon mooring line is considerably softer than the polyester mooring line.

7.5 Summary of Mooring Concepts

The following table shows the summary of all the mooring concepts described above.

Table 7.5: Summary of all mooring concepts

Mooring Concept	Pretension	Line Length	Anchor Distance[1)]	Clump Weight
Pure chain system	1250.00 kN	700 m	668.97 m	No
CPC system	1228.75 kN	700 m	700.28 m	No
CPC system with Clump Weight	1217.65 kN	700 m	696.18 m	21.8 T
CNC system	1255.00 kN	700 m	754.24 m	No

[1)] Anchor distance of ML 1 from fairlead

Chapter 8

Numerical Simulations

This chapter explains the numerical simulations carried out in SIMA to check the model and validate the mooring system for the environmental conditions given in the metocean data for South Korea. The various QA checks include constant wind test, free decay test and regular wave test as explained in Section 8.1.

Different load cases must be evaluated to validate the mooring design of the FWT. As mentioned in Section 3.2.3, there are three load cases evaluated for the ULS design of the mooring system. DLC 1.1 and 1.6 consider the power production situations where DLC 1.1 is assessed at the cut-off wind speed, and DLC 1.6 is evaluated at the rated wind speed. Furthermore, DLC 6.1 is also checked, which corresponds to the idling condition of the wind turbine at a 50-year sea state. This is described in Section 8.3. All numerical simulations have been carried out in SIMA.

8.1 Identification Tests

System identification tests are the QA checks performed to gain some understanding of the model and document the behaviour of the dynamic system with new mooring lines. This is an important step to ensure that the behaviour of the model is correct before proceeding with a detailed analysis.

8.1.1 Constant Wind Test

Constant wind tests are performed to check the performance of the wind turbine, including the controller. This test is carried out for wind speeds ranging from 4 m/s to 24 m/s at 2 m/s intervals. The wind is treated as constant and uniform for one wind speed. Jonswap 3 parameter spectrum is used to define the sea state. No current is considered during this simulation.

The turbine takes longer to start up and achieve a steady state at lower wind speeds compared to relatively higher wind speeds. This can be seen from Figure 8.1 which shows the RPM of the INO WINDMOOR turbine at 4 m/s and 12 m/s wind speeds. Hence, the duration must be sufficiently long as the statistical analysis is performed after the turbine achieves a steady state. So the analysis was performed for a duration of 850 s for each wind speed.

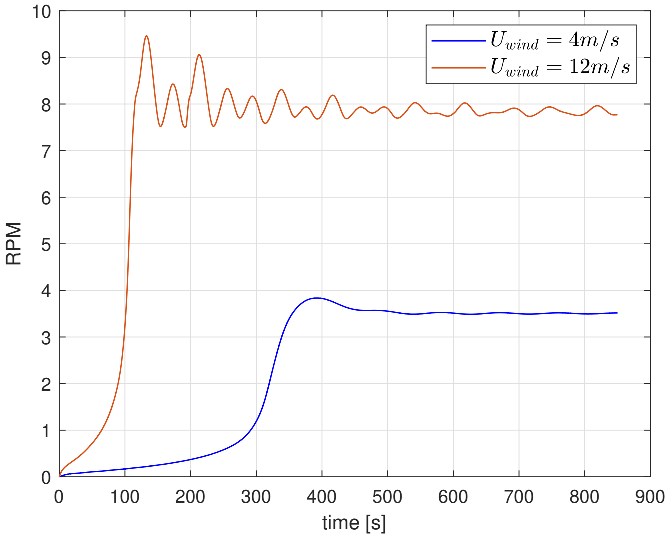

Figure 8.1: Comparison of RPM of the INO WINDMOOR turbine at 4 m/s and 12 m/s

Table 8.1: SIMA settings for constant wind test

SIMA Setting	Value
Simulation Length	850 s
Simulation Time Step	0.005 s
Time Increment in SIMA	0.01 s
Environmental Condition	H_s = 0.001 m, T_p = 20 s
Horizontal Wind Velocity	4 m/s to 24 m/s at 2 m/s interval

The SIMA settings for the constant wind test is given in Table 8.1. The result of this test is presented in Section 9.1.

8.1.2 Decay Test

Free decay tests are performed to document the natural period of the system in all 6 DoFs. For the decay test, the initial displacement in translational DoFs is achieved by applying a ramp force for a duration of 100 s in SIMO. The ramp force is followed by a constant force for another 100 s. The force is then removed, and the platform is let to oscillate freely in the selected DoF. The oscillation decays over a period of time. The ramp force and constant force are defined using the ‘specified force’ option in SIMO. An example of decay force with ramp duration of 100 s and constant force duration of 100 s is shown in Figure 8.2.

Similarly, for rotational DoFs, a ramp moment and constant moment are applied for 100 s each, and then the floater is released to oscillate. The ramp moment and constant moment are defined using the ‘specified moment’ option in SIMO.

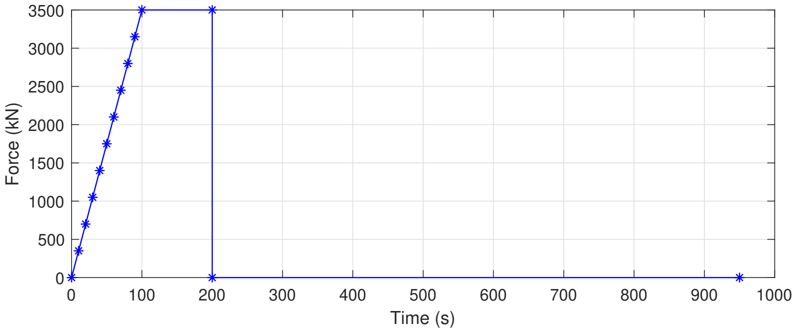

Figure 8.2: Example of decay force with ramp force and constant force in Surge

The SIMA settings and simulation parameters for the decay tests are given in Tables 8.2 and 8.3.

Table 8.2: SIMA settings for decay test

SIMA Setting	Value
Simulation Time Step	0.005s
Time Increment in SIMA	0.01s
Environmental Condition	No wind, wave or current
Turbine Status	Parked

Table 8.3: Simulation parameters for decay test

Motion	Force/Moment	Simulation Length (s)	Attack Point of Decay Force (Local Coordinates)
Surge	3500 kN	950	(0,0,0)
Sway	3500 kN	950	
Heave	5330 kN	800	
Roll	300000 kNm	800	
Pitch	300000 kNm	800	
Yaw	11000 kNm	950	

The results of the free decay test for various mooring concepts are presented in Section 9.2.

8.1.3 Regular Wave Test

Regular wave tests are performed to derive the RAO of the FWT in different DoFs at various wave headings. As explained in Section 6.2.8, RAO provides the response of a structure due to unit wave amplitude in a given DoF. Mathematically, it can be derived as shown below for heave only case.

The forced equation of motion in heave can be expressed as follows:

$$(M + A_{33}(\omega))\ddot{\eta_3} + B_{33}(\omega)\dot{\eta_3} + C_{33}\eta_3 = F_{3,exc}(\omega) \tag{8.1}$$

where M is the mass, $A_{33}(\omega)$ is the frequency dependent added mass, $B_{33}(\omega)$ is the frequency dependent potential damping, C_{33} is the restoring coefficient in heave, $F_{3,exc}(\omega)$ is the excitation force. $\ddot{\eta_3}$, $\dot{\eta_3}$ and η_3 are the acceleration, velocity and displacement in heave. In steady state condition, we can represent the heave motion and the excitation force as shown below.

$$\eta_3 = \eta_{3a}e^{i\omega t} \tag{8.2a}$$

$$F_{3,exc} = f_{3a}e^{i\omega t} \tag{8.2b}$$

where, η_{3a} and f_{3a} are the amplitude of heave motion and force respectively and are oscillating with the incident wave frequency ω. Substituting Equations (8.2a) and (8.2b) in Equation (8.1), the following expression can be derived.

$$\begin{aligned} &(-\omega^2(M + A_{33}(\omega)) + i\omega B_{33}(\omega) + C_{33})\eta_{3a} = f_{3a} \\ \Rightarrow\ &\frac{\eta_{3a}}{f_{3a}} = \frac{1}{(-\omega^2(M + A_{33}(\omega)) + i\omega B_{33}(\omega) + C_{33})} \end{aligned} \tag{8.3}$$

Multiply and divide the left-hand side of the above equation with wave amplitude ζ_a to derive the following expression.

$$\frac{\eta_{3a}}{\zeta_a} = \frac{f_{3a}}{\zeta_a} \cdot \frac{1}{(-\omega^2(M + A_{33}(\omega)) + i\omega B_{33}(\omega) + C_{33})} \tag{8.4}$$

Equation (8.4) shows the expression for heave RAO between wave amplitude and heave motion. The RAO for other DoFs can be similarly derived.

Regular wave tests were performed with the following SIMA settings and simulation parameters.

Table 8.4: SIMA settings for regular wave test

SIMA Setting	Value
Simulation Length	1100 s
Simulation Time Step	0.005 s
Time Increment in SIMA	0.01 s
Wave	Regular Wave
Wind	No Wind
Current	No current

Table 8.5: Simulation parameters for regular wave test

Hs	Tp	Wave Heading
1 m	5 s to 35 s at 2.5 s interval	45 deg., 90 deg. and 180 deg.

The RAOs are also compared with WAMIT output, and the results are presented in Section 9.4.

8.2 Convergence Study

This study is performed to decide the number of seeds required for the time-domain simulation of the mooring system. As per DNVGL-ST-0437 Loads and site conditions for wind turbines [4], the simulations for the estimation of extreme events using stochastic wind fields and/or irregular sea states require a simulation time of 1 hour where each simulation is to be carried out with a different seed, and the sum of different realisations shall be at least 5 hours. As explained in Section 5.5, the Gumbel parameter μ gives the MPM value which is equal to the characteristic dynamic tension, $T_{c,\,dyn}$ of the mooring line. To understand how many seeds are required for the convergence of the MPM value, an analysis with 17 seeds of 1-hour duration is run in SIMA for DLC 1.6. Similarly, for DLC 6.1, an analysis with 20 seeds is run. The wind files for the analysis are generated using

TurbSim Ver. 2.0. The Gumbel parameters corresponding to the different number of seeds are determined using MATLAB. The Gumbel parameters are plotted against the number of seeds to check the convergence. The results are presented in Section 9.5. The SIMA setting and simulation parameters are shown in the following tables.

Table 8.6: SIMA settings for convergence test

SIMA Setting	Value
Simulation Length	4000 s
Simulation Time Step	0.005 s
Time Increment in SIMA	0.05 s
Wave	Jonswap - 3 Parameters
Wind	TurbSim Fluctuating Three Component
Current	Regular current

Table 8.7: Simulation parameters for convergence test

DLC	Hs	Tp	Wave Dir.	Wind Dir.	Current Dir.	Current Vel.	Blade pitch	Wave & Wind Seed
1.6	2.65 m	11.76 s	180°	180°	180°	1 m/s	0°	101-117
6.1	11.8 m	13.3 s	180°	180°	180°	1 m/s	90°	101-120

8.3 Design Load Cases for Mooring System

The governing load cases for the ULS design of a mooring system is discussed in Section 3.2.3. As shown in Table 3.2, DLC 1.1 and 1.6 are checked during the power production stage of the wind turbine, while DLC 6.1 is evaluated when the turbine is parked or idling. The environmental conditions considered for these load cases are further discussed in the subsequent sections.

8.3.1 Environmental Conditions

The motion of the floating unit caused by environmental loads, as well as the response of the mooring lines to these motions, must be considered in the line tension analysis [43]. For stationary environmental states, the characteristic load effects are obtained, and each stationary environmental condition can be described using the following terms [43]:

- Significant wave height (H_s)
- Peak wave period (T_p)

- Wave spectrum (JONSWAP or double peaked)
- Main wave direction
- Mean wind speed
- Wind spectrum function
- Wind direction
- Surface current speed (V_c)
- Current profile over depth
- Current direction

JONSWAP wave spectrum and Kaimal wind spectrum are used for all the load cases in this thesis. As per DNV-OS-E301 Position Mooring [43], for all types of units, both in-line and in-between directions shall be analysed for all the load cases. The following two combinations of wave, wind and current relative to the unit are generally applied during the mooring analysis:

- **Collinear Environment**: The waves, wind and current are acting in the same direction. Figures 8.3(a) and 8.3(b) shows the collinear environment for an in-line and in-between case for an FWT.

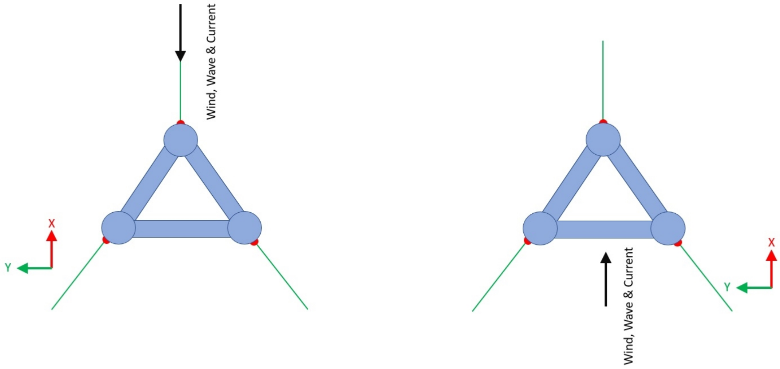

(a) In-line Collinear Condition

(b) In-between Collinear Condition

Figure 8.3: Collinear Environment

- **Non-Collinear or Spread Environment**: The waves act in-line to the unit, while wind shall be at 30° to the waves and current shall be at 45° w.r.t the waves. Figures 8.4(a) and 8.4(b) shows the spread environment for an in-line and in-between case for an FWT.

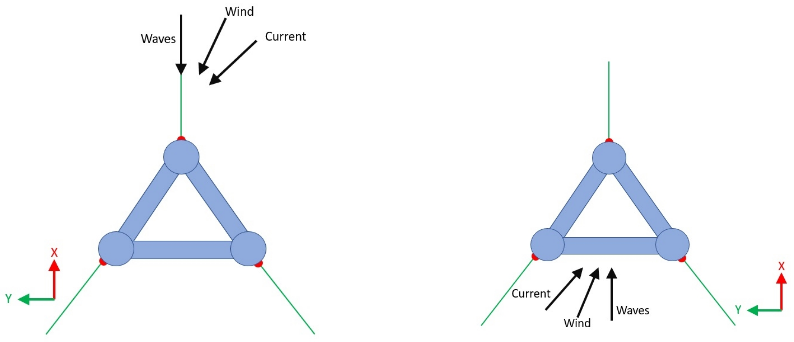

(a) In-line Spread Condition

(b) In-between Spread Condition

Figure 8.4: Non-Collinear (or) Spread Environment

8.3.2 Environmental Condition for DLC 1.1

As explained in Section 3.2.3, DLC 1.1 is evaluated when $V_{hub} = V_{cut-off}$. The cut-off wind speed for the INO WINDMOOR turbine is obtained as 25 m/s [5]. From Table 3.2, it can be seen that the significant wave height shall be taken equal to the expected value of H_s for the wind velocity $V_{hub} = V_{cut-off}$. Based on the P50 curve given in Figure 3.2, the expected value of H_s value shall be calculated as follows:

$$H_s = 0.5892 \cdot e^{(0.0857 \times V_{hub})} = 0.5892 \cdot e^{(0.0857 \times 25)} = 5.02 \text{ m} \tag{8.5}$$

From the metocean data [19], the peak period, T_p, corresponding to the calculated H_s is obtained as 10.11 s.

Determination of Current Velocity

The metocean data does not provide any information regarding the current. As per DNVGL-RP-C205 [18], the total current at a given location can be calculated as the vector sum of each current component present, such as wind-generated current, tidal current etc. The wind-generated current component shall be calculated as follows [18]:

$$v_{c,wind}(z) = v_{c,wind}(0) \cdot (\frac{d_0 + z}{d_0}) \tag{8.6}$$

where d_0 is the reference water depth and shall be taken as 50 m, z is the distance from still water level and shall be taken as positive upwards, $v_{c,wind}(0)$ is the wind generated current velocity at the still water level. When statistical data is not available, the $v_{c,wind}(0)$ shall be calculated as follows [18]:

$$v_{c,wind}(0) = k \cdot U_{1\text{ hour, }10\text{ m}} \quad \text{where } k = 0.015 \text{ to } 0.03 \tag{8.7}$$

From the metocean data [19], $U_{1\text{ hour, }10\text{ m}}$ for 50-year RP is obtained and the $v_{c,wind}(0)$ is calculated as shown below:

$$v_{c,wind}(0) = 0.015 \cdot 31.5 = 0.47 \text{ m/s} \tag{8.8}$$

As there is no information regarding the tidal current velocity at still water level, as per discussion with supervisor Kjell Larsen, the total current velocity is conservatively assumed as 1 m/s. The current profile is maintained constant throughout the water depth. The same current velocity is applied for other load cases in this thesis. The environmental conditions for DLC 1.1 are summarized in Table 8.8.

Table 8.8: Environmental parameters for DLC 1.1

Significant Wave Height	5.02 m
Peak Period	10.11 s
Wind Velocity	25 m/s
Current Velocity	1 m/s

8.3.3 Environmental Condition for DLC 1.6

As mentioned in Section 3.2.3, DLC 1.6 is checked for the rated wind speed, i.e., $V_{hub} = V_{hub}^*$. The rated wind speed for the INO WINDMOOR turbine is obtained as 10.6 m/s [5]. From Table 3.2, it can be seen that the significant wave height for DLC 1.6 shall be considered corresponding to that of the severe sea state. Therefore, based on the P90 curve given in Figure 3.2, the H_s shall be calculated as follows:

$$H_s = 1.2517 \cdot e^{0.0707 \times V_{hub}} = 1.2517 \cdot e^{0.0707 \times 10.6} = 2.65 \text{ m} \tag{8.9}$$

From the metocean data [19], the peak period, T_p, corresponding to the calculated H_s is obtained as 11.76 s. All the environmental parameters considered for DLC 1.6 are summarized in Table 8.9.

Table 8.9: Environmental parameters for DLC 1.6

Significant Wave Height	2.65 m
Peak Period	11.76 s
Wind Velocity	10.6 m/s
Current Velocity	1 m/s

8.3.4 Environmental Condition for DLC 6.1

As described in Section 3.2.3, DLC 6.1 corresponds to the case when the turbine is parked or idling with an extreme sea state and wind model corresponding to the 50-year RP condition.

The metocean data [19] shows that the wind speed corresponding to the 50-year RP at hub height is 41.5 m/s. As per DNV-OS-E301 Position Mooring [43], the wave conditions for the extreme sea state shall include a set of combinations of significant wave height and peak period along the 50-year contour. The contour plot for the Donghae location is given in Figure 8.5.

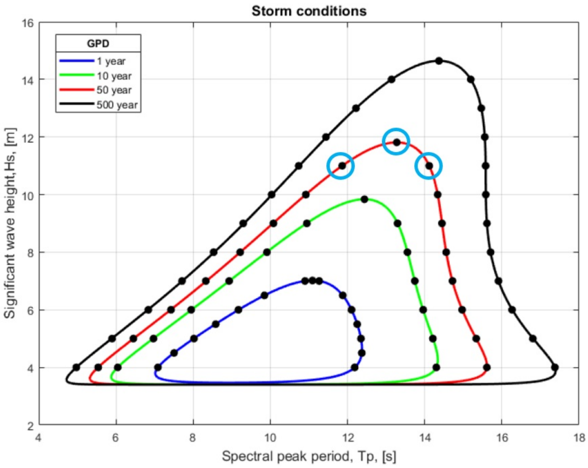

Figure 8.5: Contour lines of H_s and T_p for representative of the 1, 10, 50 and 500-year return periods for omni-directional waves at Donghae Location [19]

It is important to perform this calculation for several sea states to ensure that the mooring system is properly designed [43]. As a result, three points along the top of the 50-year contour line are evaluated for DLC 6.1. These are highlighted using blue circles in the Figure 8.5. The environmental conditions considered for DLC 6.1 are summarized in Table 8.10.

Table 8.10: Environmental parameters for DLC 6.1

	Load Cases	Waves (50-year RP)		Wind (50-year RP)	Current
		H_s	T_p		
Env 1	DLC 6.1.1	11.8 m	13.3 s	41.5 m/s	1 m/s
Env 2	DLC 6.1.2	11 m	11.98 s		
Env 3	DLC 6.1.3	11 m	14.2 s		

The results of all numerical simulations are presented in Section 9.6.

Chapter 9

Results and Discussion

This chapter presents the results of all numerical simulations explained in Chapter 8. All numerical simulations are performed in SIMA, and the results are post-processed using MATLAB.

9.1 Constant Wind Test

The constant wind test provides an understanding of the performance of the wind turbine with the controller. The result from the constant wind test is shown in Figure 9.1.

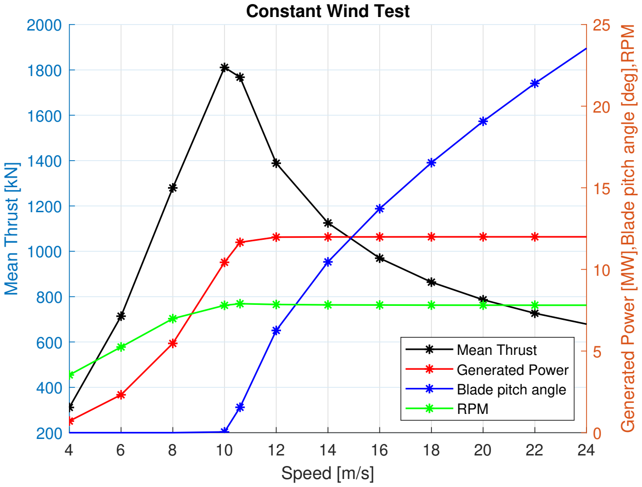

Figure 9.1: Results from constant wind test

Figure 9.1 shows the variation of mean thrust, generated power, blade pitch angle and rotor RPM w.r.t the mean wind speed, and it can be observed that till the rated wind speed of 10.6 m/s, these parameters increase w.r.t the mean wind speed. This helps the turbine to extract as much energy as possible from the wind in this regime [1]. The thrust force varies quadratically, and the power varies cubically w.r.t the wind speed as seen from Equations (4.13) and (4.14) and it can be observed that the curves follow the theoretical observation.

Beyond the rated wind speed, it can be observed that the blade pitch angle changes, and it increases w.r.t the mean wind speed. This assists the turbine in maintaining a steady RPM and a constant power output beyond the rated wind speed till cut-off, as shown in the figure. This also helps to reduce the thrust force on the FWT and protect the turbine and the substructure from increasing wind loads at higher wind speeds. From the figure, it can be seen that the maximum generated power is 12 MW. Therefore, it can be noted that the SIMA model behaves in line with the operating principle of a wind turbine. As an additional validation, the constant wind test result from the SIMA model was compared with the OpenFAST results provided by Professor Erin Bachynski-Polić of the Department of Marine Technology, NTNU, for the course project in TMR03 Integrated Dynamic Analysis of Wind Turbines in Autumn 2021. The comparison does not show any significant difference between these two models and is provided in Appendix C.

9.2 Decay Test

As described in Section 8.1.2, decay tests are performed in all 6 DoFs to determine the natural time period of the FWT. The decay test data from SIMA were transferred to MATLAB to estimate the natural time periods in 6 DoFs. Only the free decay after 200 s was considered for post-processing. Using the MATLAB toolbox for Wave Analysis for Fatigue and Oceanography (WAFO), the turning points from the time series were obtained, which were then used to calculate the natural time periods. Table 9.1 shows the result of decay test for all mooring concepts.

9.2.1 Pure Chain System in SIMO

The pure chain system in SIMO is the base case system considered in this thesis. The decay test for this system in the SIMO model was performed as a part of the project thesis in Autumn 2021, and the result from the same is presented in Table 9.1. The natural time periods of the base case system are compared with the values in INO WINDMOOR 12 MW Base Case Report [5]. It has been observed that the calculated values correspond reasonably well with the values provided in the report.

Table 9.1: Calculated rigid-body time periods for all mooring concepts

DoF	**Natural Period (s)**				
	Pure Chain SIMO	Pure Chain SIMO-RIFLEX	CPC	CPC with Clump weight	CNC
Surge	98.56	98.88	33.27	66.97	77.51
Sway	97.84	98.93	33.29	66.14	77.28
Heave	16.19	16.28	16.27	16.33	16.24
Roll	27.47	28.35	26.17	28.35	28.21
Pitch	32.44	30.72	30.47	30.77	30.67
Yaw	86.47	87.03	72.15	75.14	71.80

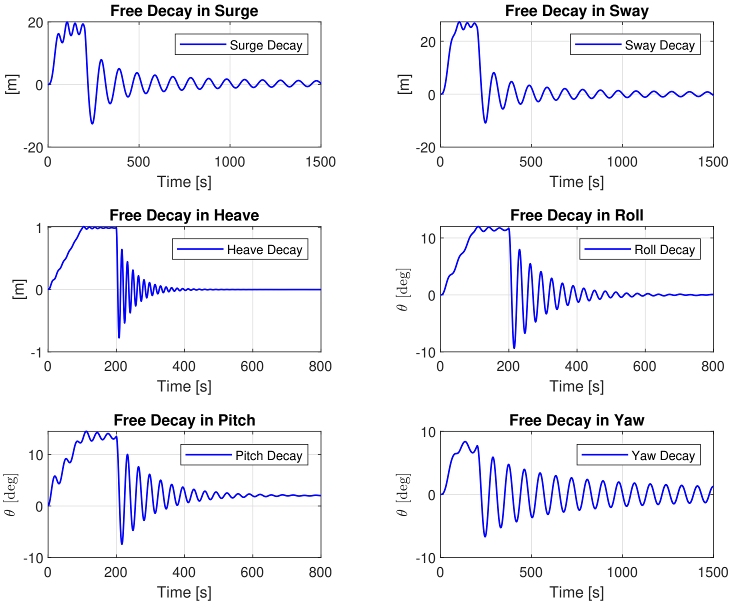

Figure 9.2: Decay test result from SIMO model for pure chain system [20]

9.2.2 Pure Chain System in SIMO-RIFLEX

The pure chain system was also defined in a SIMO-RIFLEX coupled model. The results from the decay test performed on the coupled model are presented below. The free decay time series with turning points obtained using the WAFO toolbox for this model are presented in Appendix D.

When comparing the values in Table 9.1, it can be seen that the natural time periods

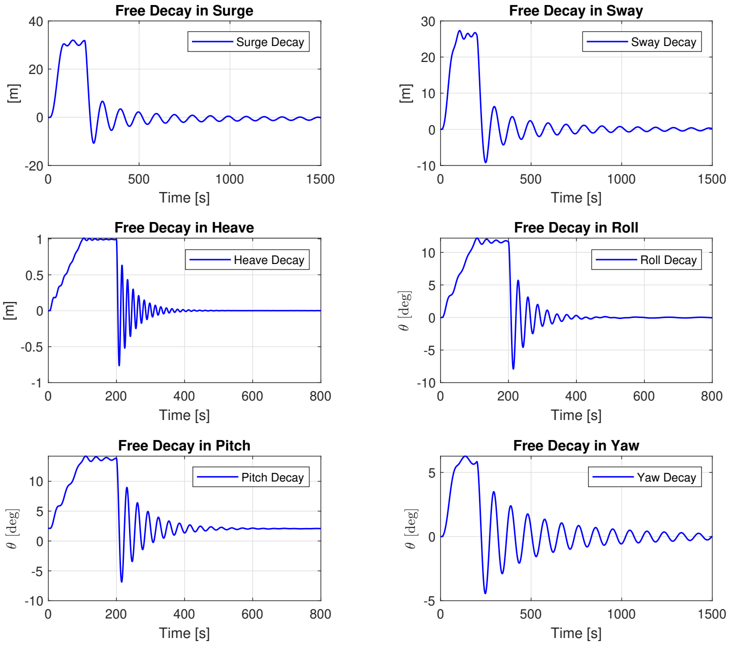

Figure 9.3: Decay test result from SIMO-RIFLEX coupled model for pure chain system

for both of these models are similar. Furthermore, the natural time periods for surge, sway, and yaw is in the range of 100 s, implying that these can only be excited by mean and LF loads. Heave natural period is in the wave period range and can be excited by first-order wave forces. Similarly, the natural periods of the roll and pitch DoFs are in the order of 30 s, and they can be triggered by first-order wave forces. Despite having the same hydrostatic stiffness as shown in Section 6.2.6, the natural period in pitch is somewhat higher than in roll. This is because the natural period is determined as follows:

$$T_n = 2\pi \cdot \sqrt{\frac{I + A}{K}} \quad \Rightarrow \quad T_n \propto \sqrt{I + A} \tag{9.1}$$

where I, A and K represent the moment of inertia, added mass and stiffness, respectively. The natural period can be considered proportional to the sum of the moment of inertia and added mass as stiffness is the same. Appendix A of INO WINDMOOR 12 MW Base Case Report [5] shows that the added mass is the same for both roll and pitch. Hence the variation arises due to the difference between the moment of inertia in roll, I_{xx}, and pitch, I_{yy}. From Table 6.2, it can be seen that $I_{yy} > I_{xx}$ and hence the pitch natural period will be higher than in roll. The calculated values correspond well with the theoretical observation.

9.2.3 Chain - Polyester - Chain System

Figure 9.4 shows the free decay plot for the CPC system. The free decay time series with turning point obtained using WAFO toolbox for this model is given in Appendix D.

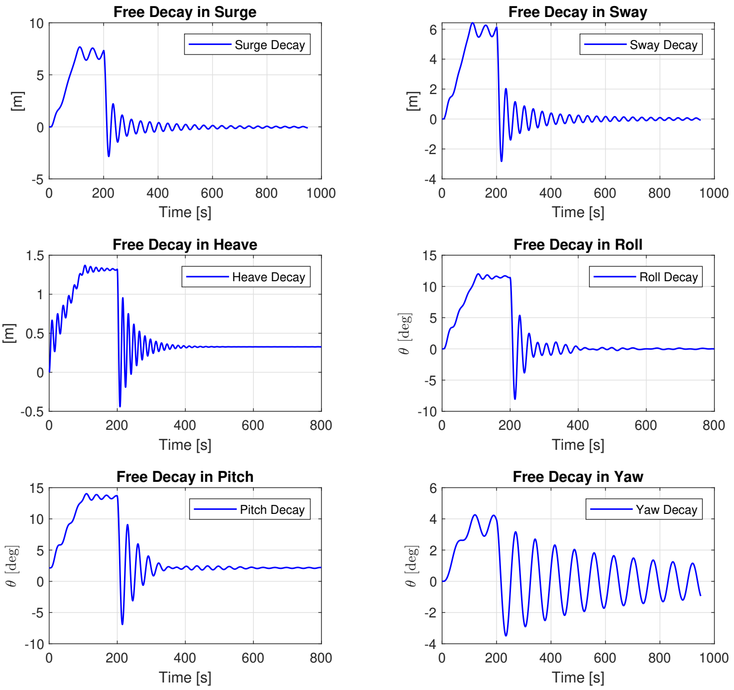

Figure 9.4: Decay test result from SIMO-RIFLEX coupled model for the CPC system

From Table 9.1 it can be seen that the natural time period in surge and sway is relatively less compared to the pure chain system indicating that the system is very stiff. Furthermore, it can be noted that the natural time periods differ in surge, sway, and yaw, but not in heave, roll, or pitch when compared to the pure chain system. This is due to the fact that the stiffness in the last three DoFs is controlled by hydrostatic stiffness, which is unaffected by the mooring system, whereas the stiffness in the first three DoFs is determined by the mooring lines. As a result, a difference is observed. Furthermore, from Figures 9.3 and 9.4 it can be seen that the maximum displacement in heave, roll, pitch and yaw are relatively unaffected by changing the mooring system. While in surge and sway, the maximum displacement decreases considerably for the CPC system suggesting that the system is relatively stiff in these DoFs compared to the pure chain system.

9.2.4 Chain - Polyester - Chain System with Clump Weight

Figure 9.5 shows the free decay plot for the CPC system with clump weight. The free decay time series with turning point obtained using WAFO toolbox for this model is given in Appendix D.

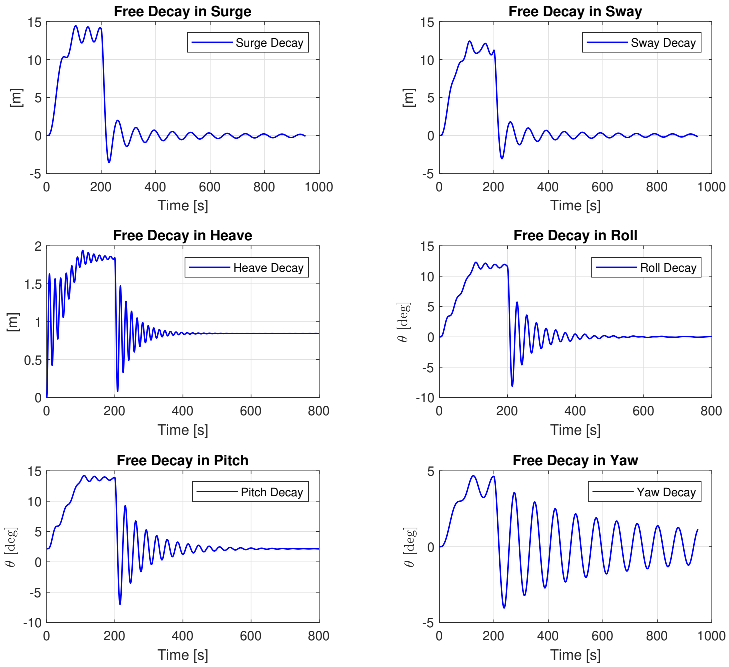

Figure 9.5: Decay test result from SIMO-RIFLEX coupled model for the CPC system with Clump weight

When the free decay plots of the CPC system with and without clump weights are compared, it can be seen that adding the clump weight to the mooring lines softens the system in surge and sway DoF. The natural time period has also increased in these two DoFs compared to the CPC system without clump weight.

9.2.5 Chain - Nylon - Chain System

Figure 9.6 shows the free decay plot for the CNC system. The free decay time series with turning point obtained using WAFO toolbox for this model is given in Appendix D.

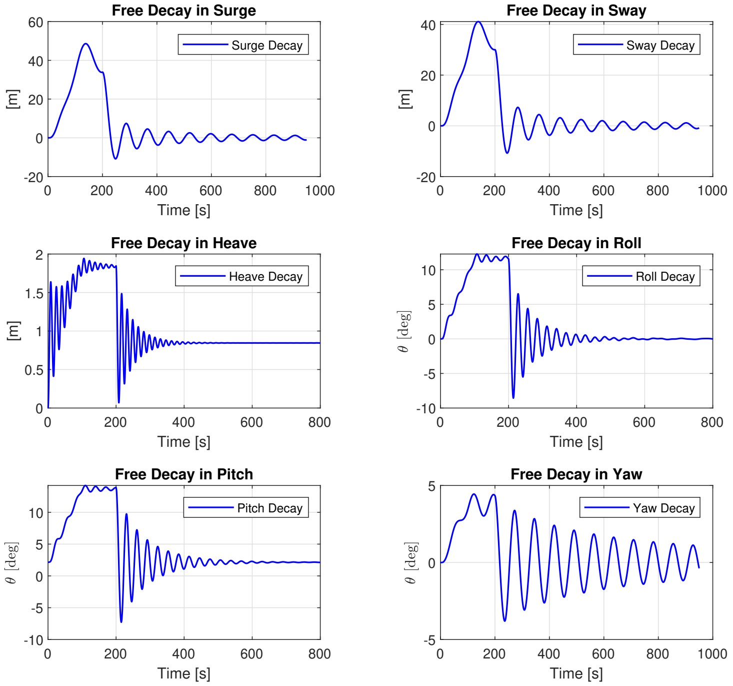

Figure 9.6: Decay test result from SIMO-RIFLEX coupled model for the CNC system

When comparing the free decay plots and natural time periods of the CNC system to the CPC system, it can be seen that the CNC system is softer. The natural time periods of this system in surge and sway are higher than the polyester system but lower than the pure chain system. The natural time period in the other four DoFs is quite comparable.

9.3 Pull Out Test

Pull out tests determine the system's total stiffness and restoring force. Pull out tests are performed for surge DoF in both in-line and in-between directions, as shown below.

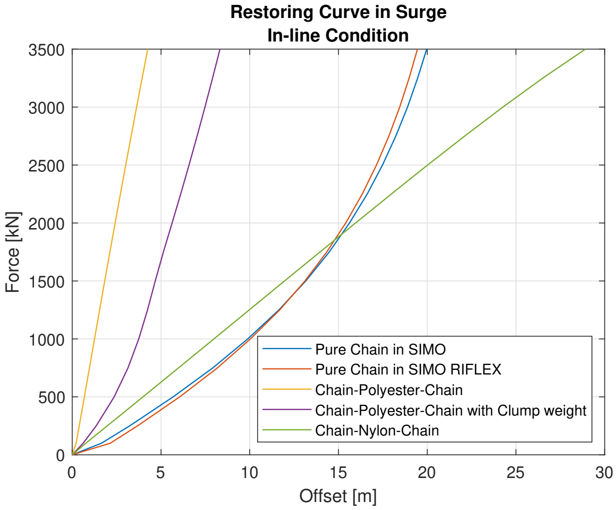

Figure 9.7: Pull out test result for in-line direction

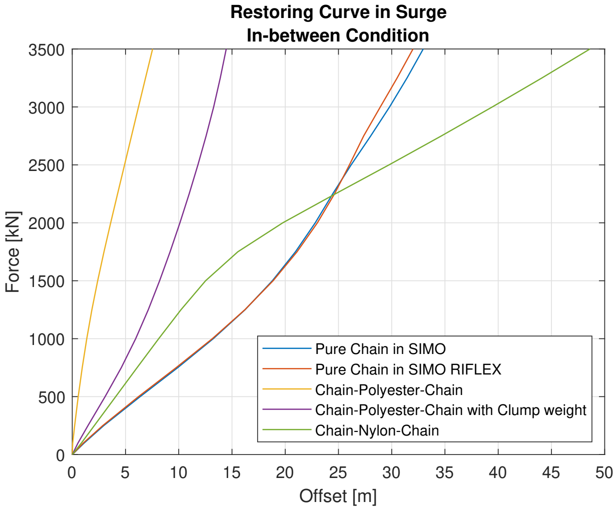

Figure 9.8: Pull out test result for in-between direction

From Figures 9.7 and 9.8 it can be observed that for a given force, the offset in the in-between direction is higher than the in-line direction indicating that mooring lines are stiffer in the in-line direction. The system's stiffness can be calculated as the slope of these restoring curves. From both these figures, it can be seen that the slope of the restoring curve around 0 m offset is quite similar. As a result, the time period will be the same in both these cases.

For the pure chain system, it can be observed that beyond an offset of 5 m in the in-line direction and 15 m in the in-between direction, the restoring curve exhibits a non-linear behaviour because as the platform is displaced, the shape of the mooring line changes and the total stiffness is dominated by geometric stiffness for this mooring line. Moreover, it can also be seen that the restoring curves in SIMO and SIMO-RIFLEX models correspond reasonably well with each other.

For the CPC and CNC systems, it can be seen that the restoring curve is linear in the in-line direction. This is because the elastic stiffness dominates the total stiffness of these mooring lines. The CNC system in the in-between direction also follows a linear trend. However, the restoring curve has a curvature for the CNC system in the in-between condition when the offset is around 15 m. This is because the total restoring force is calculated as the difference between horizontal tension of the windward and leeward at a given offset, as shown in Figure 2.18. In the in-between direction, the leeward lines may become slack after a specific offset, resulting in a curvature in the restoring curve.

For both in-line and in-between directions, the CPC system with clump weights shows a slightly non-linear behaviour than the CPC system without clump weight. This is due to the contribution of clump weight in providing geometric stiffness to the system. The system is also softer in surge when clump weight is introduced to the mooring line.

9.4 Regular Wave Test

As explained in Section 8.1.3, regular wave tests are carried out to determine the RAO of the FWT in a given DoF. This is calculated only for the base case mooring system in SIMO. Figures 9.9–9.11 shows the comparison of RAO in surge, heave and pitch for the wave period range of 5 s to 30 s determined from SIMA and WAMIT. These are determined for a wave heading, $\beta = 180°$.

Similarly, Figures 9.12–9.14 shows the comparison of RAO in sway, roll and yaw for the wave period range of 5 s to 30 s determined from SIMA and WAMIT. These are calculated for wave heading, $\beta = 90°$.

The figures show that RAOs calculated from SIMA correspond reasonably well to WAMIT results for surge, sway, heave, roll and pitch. The difference in the peak observed in heave could be due to the difference in damping between these two models. For example, in SIMA, the damping contribution from the mooring lines is taken into account, whereas as WAMIT results are provided as input, it is

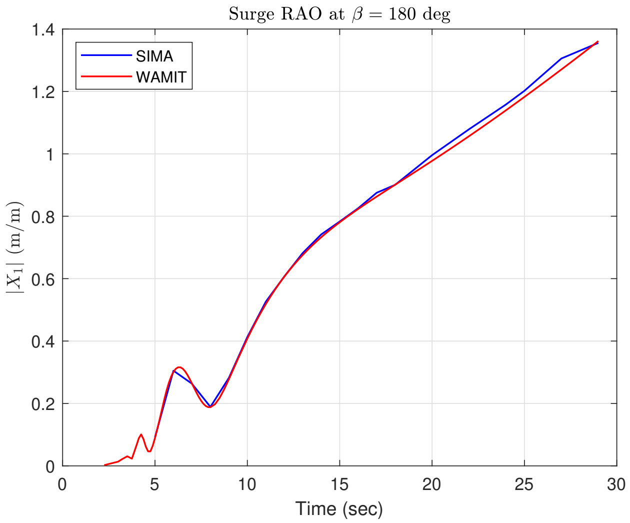

Figure 9.9: Surge RAO Comparison for $\beta = 180°$

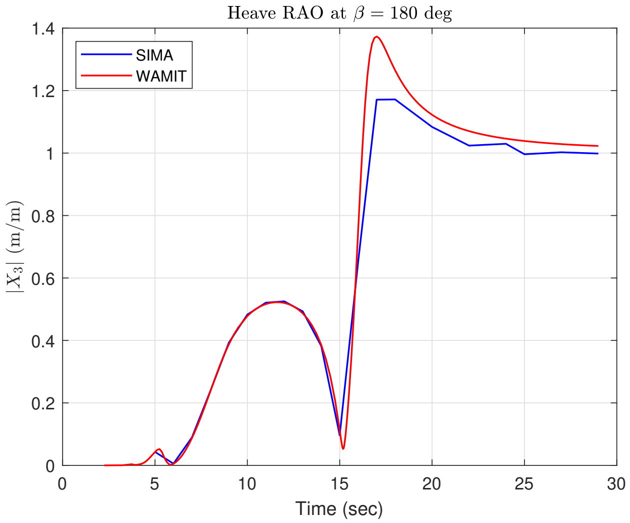

Figure 9.10: Heave RAO Comparison for $\beta = 180°$

unknown whether this contribution is considered in WAMIT analysis.

In yaw DoF, a significant deviation is observed between RAOs calculated from SIMA and WAMIT beyond 20 s. This is because, in the SIMA model, an iner-

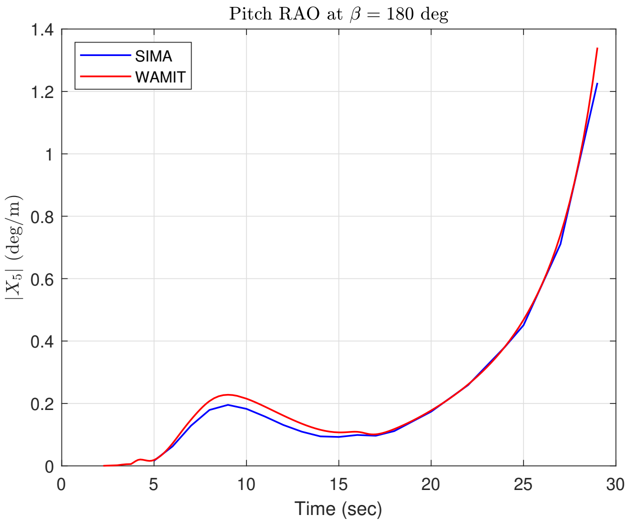

Figure 9.11: Pitch RAO Comparison for $\beta = 180°$

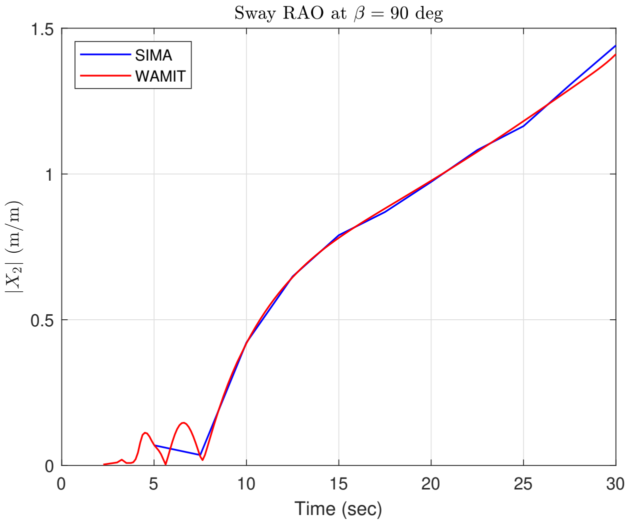

Figure 9.12: Sway RAO Comparison for $\beta = 90°$

tial coupling term I_{zx} exists between yaw and roll, resulting in a double peak in the yaw RAO determined from SIMA. It can also be observed from Figures 9.13 and 9.14 that beyond 20 s, the yaw RAO follows the same trend as the RAO in roll.

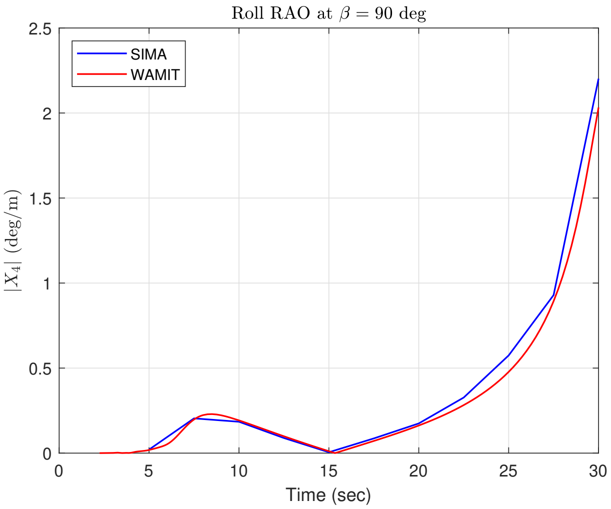

Figure 9.13: Roll RAO Comparison for $\beta = 90°$

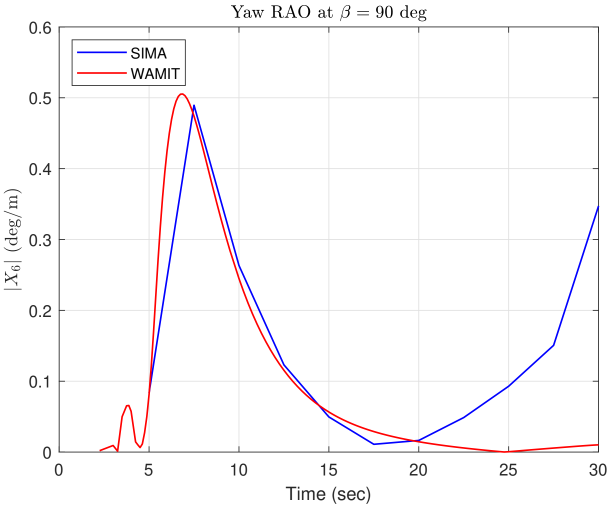

Figure 9.14: Yaw RAO Comparison for $\beta = 90°$

9.5 Convergence Study

A convergence study is carried out to determine the number of seeds required in the time-domain analysis. It is essential to determine the number of seeds because wave seed represents the randomness in the sea state in SIMA.

This study uses the base case mooring system in the SIMO model for two load cases; DLC 1.6 and DLC 6.1. The results of the study are presented below. Figures 9.15 and 9.16 shows the results for DLC 1.6.

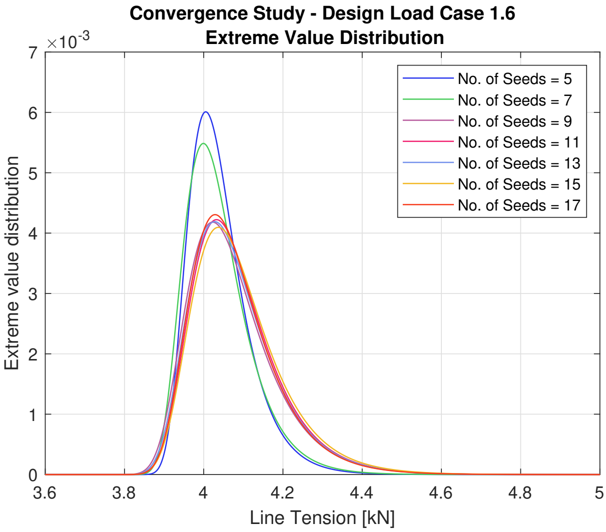

Figure 9.15: DLC 1.6 Extreme value distribution of various number of seeds

From Figure 9.15 it can be observed that when the number of seeds is greater than 7, the variation in MPM value is less. Figure 9.16 shows the variation of Gumbel parameters to the number of seeds.

From Figure 9.16 it can be noted that, in general, the variability along the y-axis is less. It can be further seen that the variation in μ is limited after 10 seeds. Therefore, based on this study, the number of seeds has been chosen as 12 for DLC 1.6. The same is used for DLC 1.1 also. The same number of seeds are used for all mooring concepts.

Figures 9.17 and 9.18 shows the results for DLC 6.1. From Figure 9.17 it can be observed that when the number of seeds is greater than 15, the variation in MPM value is less.

Figure 9.18 shows the variation of Gumbel parameters to the number of seeds. From Figure 9.18 it can be observed that the variation in μ value is limited when the number of seeds is greater than 15. Based on this study, the number of seeds has been chosen as 16 for DLC 6.1. The same number of seeds are used for all

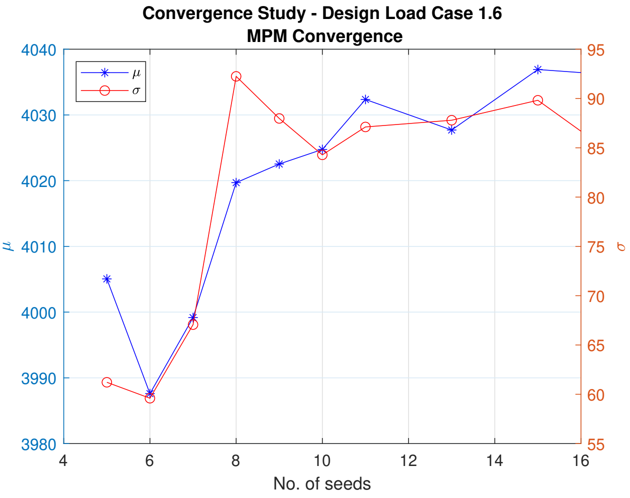

Figure 9.16: DLC 1.6 Convergence plot of MPM value

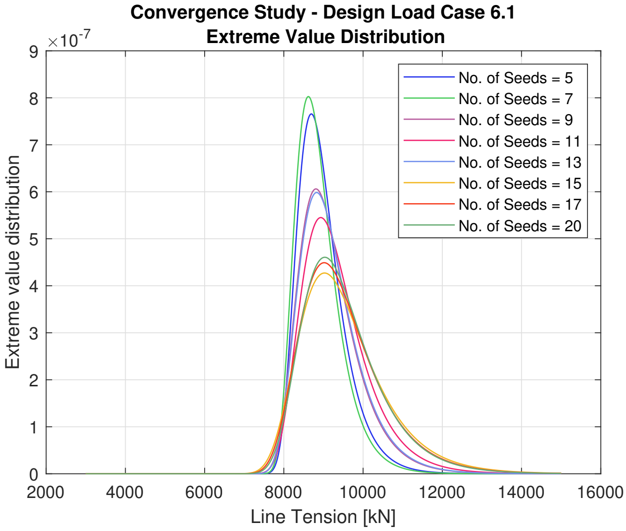

Figure 9.17: DLC 6.1 Extreme value distribution of various number of seeds

mooring concepts.

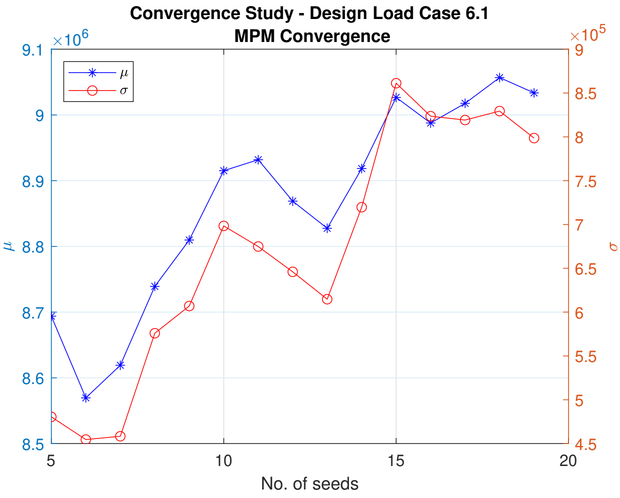

Figure 9.18: DLC 6.1 Convergence plot of MPM value

9.6 Time Domain Analysis

This section presents the results of the time-domain analysis evaluated for the different mooring concepts discussed in Chapter 7. All results are post-processed using MATLAB. The power spectra shown in the results are calculated using the WAFO toolbox, where the default frequency smoothing using a parzen window function on the estimated autocovariance function is used to smoothen the spectra [49].

9.6.1 Base Case Mooring System in SIMO

This section describes the result of the analysis performed to validate the base case mooring system for the FWT operating at 100 m water depth in Donghae location, South Korea.

Motions

Table 9.2 shows the mean offset, the MPM and standard deviation in surge, heave and pitch for various environments and load cases evaluated for the base case mooring system. The negative sign in surge indicates that the FWT is displaced along the negative x-axis and the negative sign in pitch indicates FWT is pitching by aft. From Table 9.2 it can be observed that the in-between condition is softer and results in a higher offset in surge for all load cases compared to the in-line condition. This is consistent with the restoring curves seen for the pure chain system in SIMO.

Table 9.2: Mean offset, MPM and standard deviation in Surge, Heave and Pitch for Base Case Mooring System

Load cases	**Environment**	**Surge (m)**			**Heave (m)**			**Pitch (deg)**		
		Mean offset	MPM	Std. Dev.	Mean offset	MPM	Std. Dev.	Mean offset	MPM	Std. Dev.
DLC 1.1	In-line Collinear	-11.46	-16.61	1.25	-0.05	1.65	0.50	-0.68	-4.31	1.17
	In-between Collinear	18.92	24.97	2.01	-0.08	1.55	0.49	0.70	4.59	1.20
	In-line Spread	-10.76	-15.76	1.25	-0.07	1.67	0.51	-0.34	-3.66	0.96
	In-between Spread	15.08	20.77	1.70	-0.06	1.64	0.49	1.30	4.81	1.09
DLC 1.6	In-line Collinear	-12.89	-15.59	1.34	-0.12	0.88	0.30	-3.61	-9.17	2.08
	In-between Collinear	22.23	25.41	2.23	-0.18	0.81	0.30	4.03	7.40	1.66
	In-line Spread	-12.28	-15.27	1.45	-0.16	0.89	0.30	-2.78	-7.09	1.55
	In-between Spread	15.76	18.58	1.72	-0.15	0.92	0.30	4.23	7.97	1.61
DLC 6.1.1	In-line Collinear	-11.64	-21.95	2.46	-0.11	4.49	1.36	2.61	5.11	0.84
	In-between Collinear	20.54	31.92	3.39	-0.01	4.79	1.40	-1.96	-4.52	0.66
	In-line Spread	-9.99	-21.33	2.47	-0.07	4.68	1.36	4.12	10.04	2.13
	In-between Spread	17.58	27.86	3.28	0.01	4.68	1.38	-1.25	-3.79	0.67
DLC 6.1.2	In-line Collinear	-12.01	-22.24	2.30	-0.10	4.02	1.23	2.62	5.28	0.88
	In-between Collinear	21.17	33.34	3.47	-0.01	4.34	1.25	-2.01	-4.58	0.68
	In-line Spread	-10.39	-21.19	2.30	-0.07	4.18	1.23	4.09	10.02	2.10
	In-between Spread	18.21	29.17	3.35	0.01	4.13	1.24	-1.30	-3.85	0.69
DLC 6.1.3	In-line Collinear	-11.07	-20.52	2.32	-0.11	4.46	1.31	2.58	4.89	0.79
	In-between Collinear	19.31	29.21	3.05	0.002	4.60	1.36	-1.88	-4.29	0.63
	In-line Spread	-9.37	-20.12	2.35	-0.07	4.50	1.32	4.15	10.32	2.22
	In-between Spread	16.42	25.75	2.96	0.02	4.51	1.34	-1.16	-3.51	0.64

Motions - Power Production Load Cases

DLC 1.6 and DLC 1.1 correspond to the power production load cases at rated and cut-off conditions, respectively. When the mean offset and the MPM values of the rated and cut-off conditions are compared, it can be observed that the mean offset is slightly higher for the rated condition, but the dynamic offset is slightly higher for the cut-off condition. This can also be seen from the time series for surge shown below.

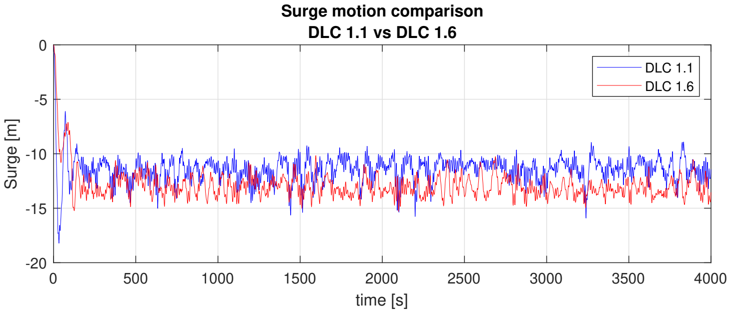

Figure 9.19: Comparison of surge time series for base case mooring system in DLC 1.1 and 1.6 in-line collinear case

The figure shows a WF component and a slowly varying LF component in the time series for both rated and cut-off conditions.

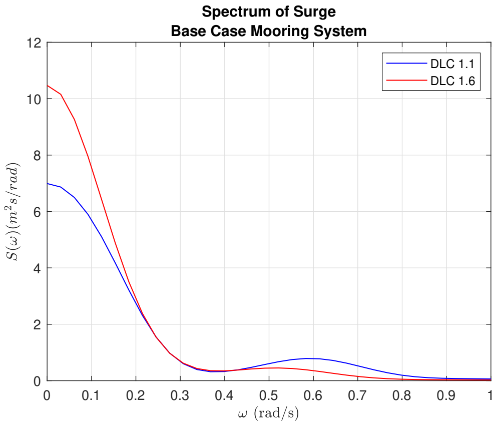

Figure 9.20: Comparison of power spectra in surge for base case mooring system in DLC 1.1 and 1.6 in-line collinear case

Figure 9.20 shows the power spectra corresponding to the time series shown in Figure 9.19. The power spectra show that the LF excitation from wind gusts is higher for DLC 1.6, while WF excitation is higher for DLC 1.1.

In the case of heave, it can be observed that the mean offset is around 0 m for both the load cases. The LF excitation does not affect heave and is only excited by WF motions as shown in Figure 9.21. DLC 1.1 has a higher H_s and T_p compared to DLC 1.6, so it has a higher MPM in heave.

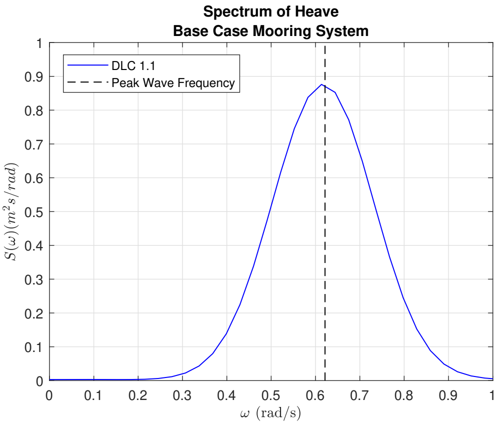

Figure 9.21: Power spectrum for heave in DLC 1.1 in-line collinear case

For pitch, it can be observed that the dynamic offset is higher for the rated condition compared to the cut-off condition. This is because the thrust force is maximum at the rated condition, and since there is a lever of 35.2 m between the platform centre and the RNA, this case will also have the highest pitching moment than the cut-off condition.

Motions - Idling Load Cases

DLC 6.1.1, 6.1.2 and 6.1.3 correspond to the load cases when the turbine is in the idling condition. The dynamic offset is particularly significant for load cases corresponding to the idling condition, as seen from the MPM values for surge reported in Table 9.2.

Figure 9.22 shows the comparison of power spectra in surge for DLC 1.1 and DLC 6.1.1. The figure shows that, as in DLC 1.1, the surge motion in DLC 6.1.1 is excited by both LF wind gusts and WF motions. However, because the wind speed, Hs, and Tp are higher at 50-year RP, the surge motion during idling is significantly higher than in the power production load case.

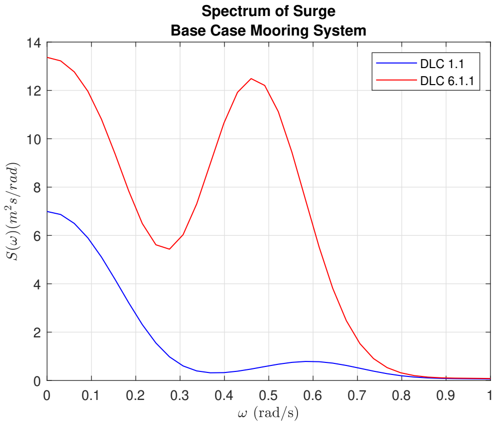

Figure 9.22: Comparison of power spectra in surge for base case mooring system in DLC 1.1 and 6.1.1 in-line collinear case

The mean offsets for heave motion of the substructure during idling conditions are also close to 0 m, as in the power production load cases. The MPM values, on the other hand, are significantly higher than the power production conditions. This is also due to higher Hs and Tp during this load case as the heave motion is only influenced by WF motion. This is also shown in Figure 9.23.

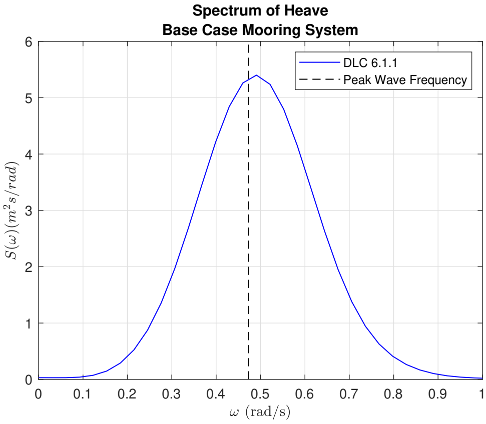

Figure 9.23: Power spectra in heave for base case mooring system in DLC 6.1.1 in-line collinear case

In the case of pitch motion of the FWT, it can be seen that there is a change of sign in pitch in the in-line and in-between directions for power production load cases and idling load cases. As previously stated, the turbine generates thrust force during the power production stage that is not present when the turbine is idling. As a result, the pitching moment is also zero. As a result, the pitch direction changes when the turbine is idling.

It is also worth noting that the idling condition also resulted in a very high yaw angle of the FWT, as shown in Figure 9.24.

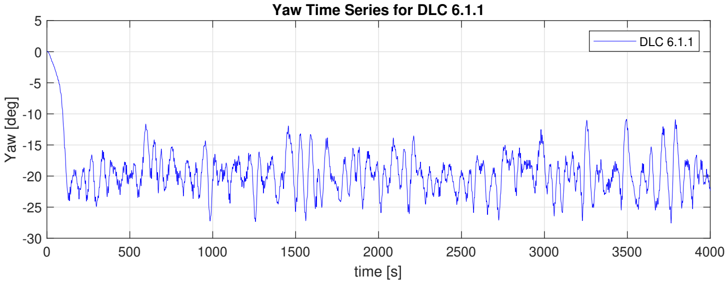

Figure 9.24: Yaw time series for DLC 6.1.1 Inline Collinear Case

This was identified as one of the dynamic instabilities of the FWT as discussed in Section 4.3. The yaw misalignment at extreme sea state is caused to the difference in stiffness of the mooring system, RNA and tower. Following additional discussion with supervisor Kjell Larsen, it became clear that this is a real problem for FWTs, and it could be reduced to some extent by increasing the pretension of the mooring lines. Hence to understand this effect, the pretension of this system was increased to 1500 kN, which resulted in approximately a 30% reduction in yaw angle.

Mooring Line Tension

Table 9.3 shows the calculated mean, dynamic and design tension of the mooring line. The design is compared against the characteristic capacity of the mooring line as per Equation (3.1) to check if the ULS design criterion is satisfied.

As it can be seen from Table 9.2, the maximum offset occurs for the collinear load cases. ML 1 will be the most heavily loaded windward line in the in-line direction and the most heavily loaded leeward line in the in-between direction. Hence, the design tension calculation and ULS check are performed for ML 1. The characteristic capacity, S_c, is calculated as per Equation (3.3), where the minimum breaking strength of the component is considered as the MBL of the chain element

Environment	DLC 1.1				
	$T_{c,mean}$ (kN)	$T_{c,dyn}$ (kN)	T_d (kN)	S_c (kN)	Status
In-line Collinear	2648.71	4780.61	11809.38	20172.30	OK
In-between Collinear	670.47	748.88	2182.15	20172.30	OK
In-line Spread	2518.20	4667.99	11442.65	20172.30	OK
In-between Spread	724.40	807.32	2354.53	20172.30	OK

(a) DLC 1.1 line tension for ML 1 for the base case mooring system

Environment	DLC 1.6				
	$T_{c,mean}$ (kN)	$T_{c,dyn}$ (kN)	T_d (kN)	S_c (kN)	Status
In-line Collinear	3143.20	4288.14	11590.41	20172.30	OK
In-between Collinear	590.96	670.99	1942.48	20172.30	OK
In-line Spread	3124.40	4142.25	11310.66	20172.30	OK
In-between Spread	684.11	770.04	2236.91	20172.30	OK

(b) DLC 1.6 line tension for ML 1 for the base case mooring system

Environment	DLC 6.1.1				
	$T_{c,mean}$ (kN)	$T_{c,dyn}$ (kN)	T_d (kN)	S_c (kN)	Status
In-line Collinear	3342.57	9047.03	20177.64	20172.30	NOT OK
In-between Collinear	677.49	817.73	2311.76	20172.30	OK
In-line Spread	2710.87	7088.45	15928.92	20172.30	OK
In-between Spread	716.02	894.17	2495.62	20172.30	OK

(c) DLC 6.1.1 line tension for ML 1 for the base case mooring system

Environment	DLC 6.1.2				
	$T_{c,mean}$ (kN)	$T_{c,dyn}$ (kN)	T_d (kN)	S_c (kN)	Status
In-line Collinear	3413.81	8765.07	19776.81	20172.30	OK
In-between Collinear	669.34	779.40	2269.08	20172.30	OK
In-line Spread	2775.78	7137.72	16099.53	20172.30	OK
In-between Spread	706.37	875.82	2450.96	20172.30	OK

(d) DLC 6.1.2 line tension for ML 1 for the base case mooring system

Environment	DLC 6.1.3				
	$T_{c,mean}$ (kN)	$T_{c,dyn}$ (kN)	T_d (kN)	S_c (kN)	Status
In-line Collinear	3203.87	8091.22	18324.67	20172.30	OK
In-between Collinear	693.64	833.38	2360.14	20172.30	OK
In-line Spread	2586.71	6117.31	14068.01	20172.30	OK
In-between Spread	734.30	907.54	2542.79	20172.30	OK

(e) DLC 6.1.3 line tension for ML 1 for the base case mooring system

Table 9.3: Line tension for ML 1 in base case mooring system

as given in Table 7.2. The load factors as per consequence class 1 are considered for determining the design tension.

Mooring Line Tension - Power Production Load Cases

From Table 9.3 it can be observed that the in-line collinear condition results in the maximum design tension in the mooring lines. It is known that the top end motions of the substructure influence the line tension [10]. In the case of surge, the mean value was higher at the rated condition, while the MPM was higher at the cut-off condition. It can be seen from Tables 9.3(a) and 9.3(b) that mean tension is higher at the rated condition while the dynamic tension is slightly higher during the cut-off condition, indicating that line tension is strongly correlated to the surge motion.

Furthermore, from Tables 9.3(a) and 9.3(b) it can also be noted that there is a sufficient margin between the design tension and the characteristic capacity of the mooring line for the rated condition and cut-off condition. The mooring line uses 57.4 % of its total capacity at the rated condition and 58.5 % at the cut-off condition, indicating that the power production cases are not critical for the mooring design.

Mooring Line Tension - Idling Load Cases

For DLC 6.1.1, 6.1.2 and 6.1.3, it can be seen that the design tensions are higher than the power production load cases. This is also because the surge motion is higher when the turbine is idling, as seen above. It can be noted that DLC 6.1.1 marginally exceeds the characteristic capacity of the windward mooring line for environment 1 at a 50-year sea state in the in-line collinear condition. Figures 9.25 and 9.26 shows the time series and power spectrum for DLC 6.1.1 windward mooring line.

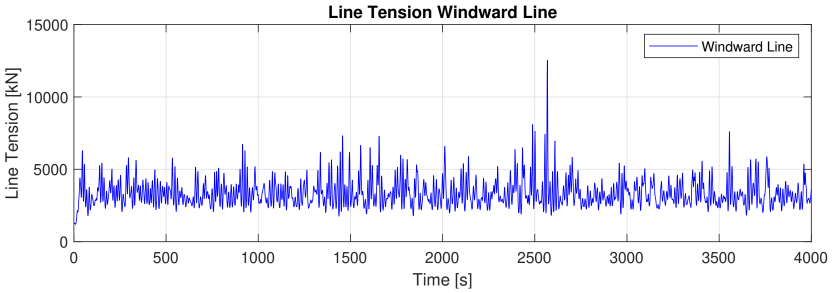

Figure 9.25: Time series of line tension of windward line for DLC 6.1.1 base case mooring system

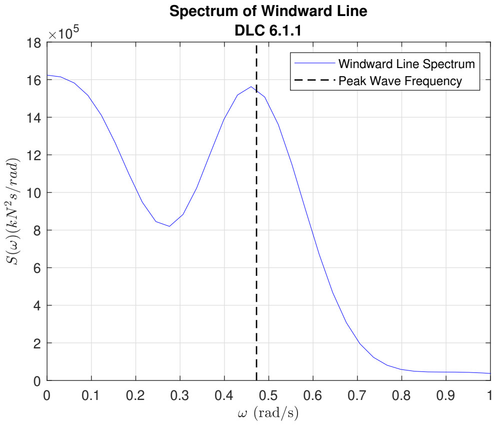

Figure 9.26: Power spectrum of line tension of windward line for DLC 6.1.1 base case mooring system

From the time series and power spectrum it can be observed that both LF and WF excitation affect the line tension of the windward mooring line.

Hence, to satisfy the ULS criteria for the base case mooring system, the chain MBL has to be increased. Accordingly, the chain grade was increased to R4S, maintaining the same diameter and weight for the chain. The new MBL was 23559 kN which gives a characteristic capacity of $S_c = 22381.05$ kN. This gives the utilisation factor of 90% for the mooring line, thereby satisfying the design criteria for the base case mooring system. In addition to the ULS check, it was verified whether the leeward mooring lines were going slack for DLC 6.1. From the time series, it was observed that the line tension did not go to zero, as shown in Figure 9.27.

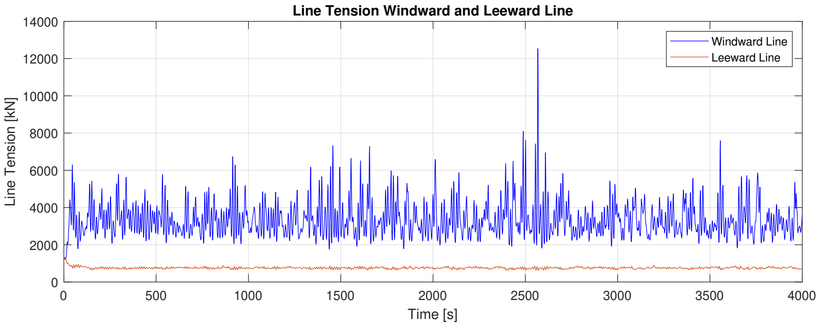

Figure 9.27: Time series of line tension for DLC 6.1.1 base case mooring system

9.6.2 Comparison of Base Case Mooring System in SIMO and SIMO-RIFLEX Coupled Model

As explained in Section 6.1, SIMO can only estimate the quasi-static line tension and underestimates the dynamic effects. Hence to understand the dynamic amplification in the mooring line tension, the base case mooring system is also analyzed using a SIMO-RIFLEX coupled model.

Based on the discussion in Section 9.6.1, it can be understood that the load cases during the idling condition are more critical than the load cases during power production in determining the maximum offset of the FWT and the line tension. Hence, the comparative study is performed for DLC 6.1.1 in-line collinear condition, and the results are presented below.

From Figure 9.28, it can be observed that no significant difference is present in the mean offset or MPM in both these models.

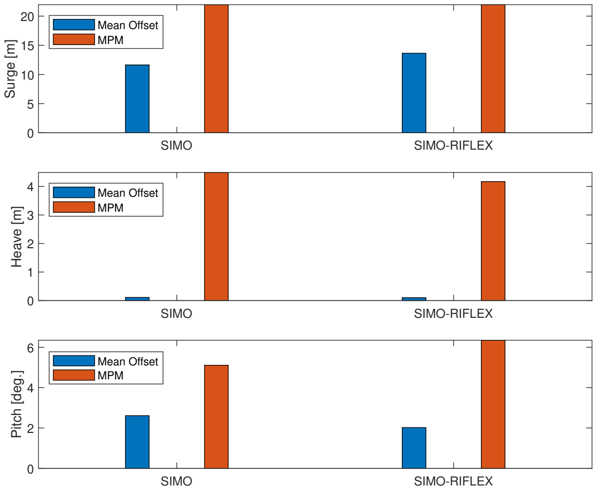

Figure 9.28: Comparison of mean offset and MPM for surge, heave and pitch in SIMO and SIMO-RIFLEX Coupled model

Similarly, from Figure 9.29 it can be seen that the mean tension is the same for both these models. On the other hand, the dynamic tension is amplified by about 20% in the SIMO-RIFLEX coupled model. This implies that a coupled SIMO-RIFLEX model is required to capture dynamic effects such as mooring line drag forces.

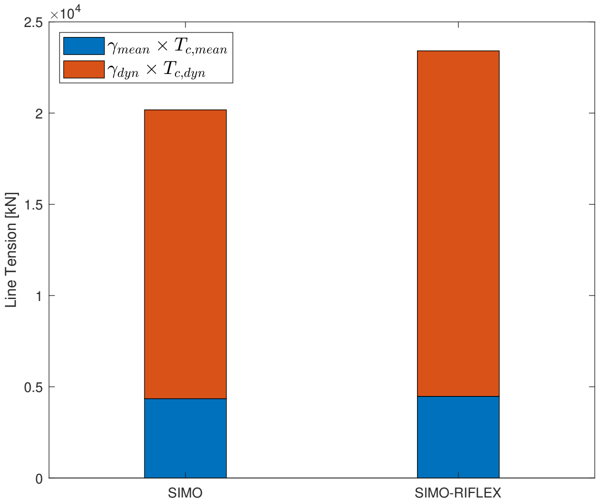

Figure 9.29: Comparison of line tension for SIMO and SIMO-RIFLEX Coupled model

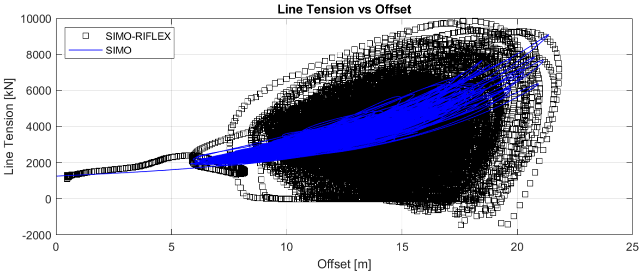

Figure 9.30: Line tension vs Offset in SIMO and SIMO-RIFLEX Coupled model

Figure 9.30 shows the comparison of line tension against the offset of the FWT in both SIMO and SIMO-RIFLEX coupled models. SIMO uses catenary equations to estimate the line tension, and it can be seen that the curve follows a catenary shape as well. A disadvantage of this method is that it underestimates the slack criterion. From the line tension estimated using the coupled SIMO-RIFLEX model, it can be seen that the tension is higher than in the SIMO model, and the dynamic amplification can also be seen in the figure. Furthermore, as the offset increases, the rate at which the line tension falls to zero and goes into a slack condition also increases in the coupled SIMO-RIFLEX model. The minimum value of line tension is essential to calculate the fatigue cycles and to estimate the slack criterion. It can also be seen that the tension goes to a negative value in SIMO-RIFLEX coupled model. This is because of the constant stiffness assumed in the model and is not a physical effect.

9.6.3 Comparison Study of Various Mooring Concepts

This section summarizes the results and compares several mooring concepts, with an emphasis on line tension and the platform response in surge. As seen from Section 9.6.1, the maximum response is observed for in-line collinear environment with 50-year RP condition. Hence, the results of load case DLC 6.1.1 in in-line collinear condition are presented in detail for the comparative study. The result of DLC 6.1.1 in the in-between collinear condition is presented in Appendix E. Similarly, the results for the rated and cut-off conditions are presented in Appendices F and G respectively.

Motions

Figure 9.31 shows the mean offset and MPM of the critical responses for the FWT for all mooring concepts. The results from the SIMO model are presented for the pure chain mooring system.

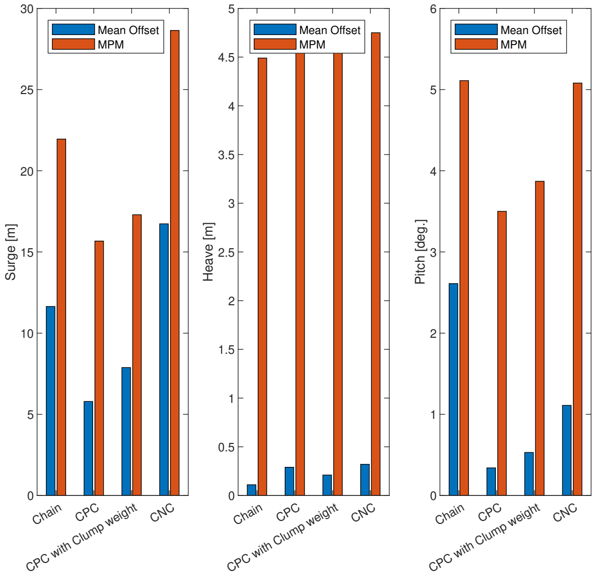

Figure 9.31: Comparison of platform motions for all mooring concepts

From the Figure 9.31 it can be observed that the mean offset and MPM in heave do not change w.r.t the mooring concept. The heave motion is only affected by WF loads, as shown in Figure 9.32. As the mooring system can only control the mean offset and LF motion, heave is not affected by changing the mooring concepts.

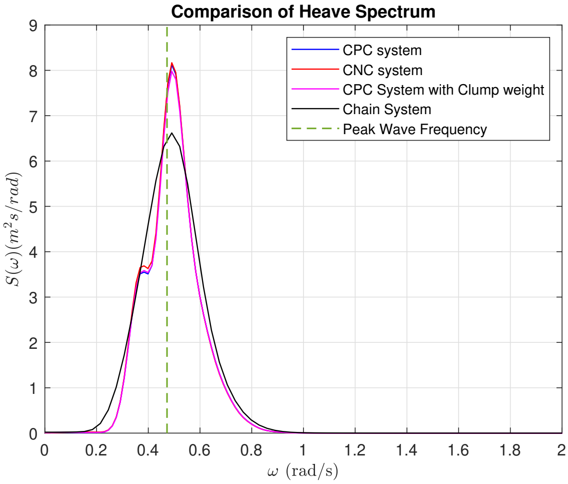

Figure 9.32: Power spectra of heave for all mooring systems

However, a difference is observed in surge and pitch motions. When the surge and pitch motions are compared, it can be seen that the CPC concept is the stiffest system compared to all four mooring concepts. This is followed by the CPC concept with clump weight, Chain system and CNC system.

The CNC concept results in a very high dynamic offset compared to all four mooring concepts. It was also observed that increasing the pretension of the mooring lines hardly affected the MPM in surge for this concept. As a result, the power cables should be designed to absorb this motion in surge for the CNC mooring system. As it can be seen from Figure 9.31, the MPM was reduced by 40% and 45% for CPC systems with and without clump weight respectively compared to the CNC system, suggesting that these systems are favourable when the aim is to minimize offset to avoid power cable rupture. Figures 9.33 and 9.34 compares the time series and power spectra for the CPC and CNC concepts.

From Figure 9.33 it can be observed that the CPC system has only a WF component while the CNC system has both WF and LF components present in the time series. This can be further understood from the power spectra comparison. In the CNC system, the surge motion is excited by LF forces from wind and wave drift

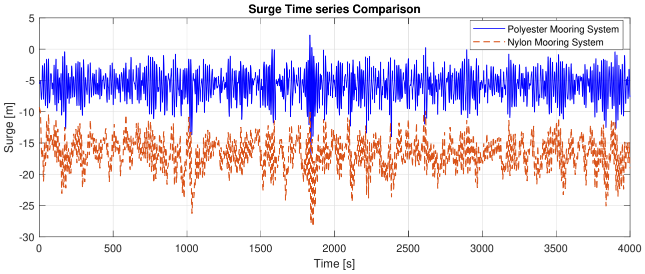

Figure 9.33: Time series of surge for CPC and CNC systems

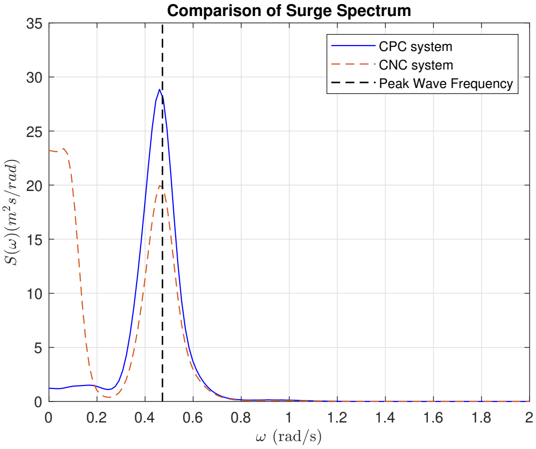

Figure 9.34: Power spectra of surge for CPC and CNC systems

compared to the CPC system. However, it can be seen that the WF excitation in surge is higher for the CPC system compared to the CNC system. This is because the CPC system is very stiff compared to the CNC system, attracting more wave frequency loads.

However, when a clump weight is introduced into the CPC system, it can be seen that the CPC system becomes softer, and the mean offset and MPM in surge are slightly higher. The period in surge increases from 33.3 s to 66.9 s when clump weights are introduced. Comparing the time series for CPC systems with and without clump weights, it can be seen that only the WF component is present in the time series for the system with clump weight. From the spectrum comparison for both these systems it can be observed that WF excitation in surge becomes less when clump weights are introduced into the system, as shown in Figure 9.35.

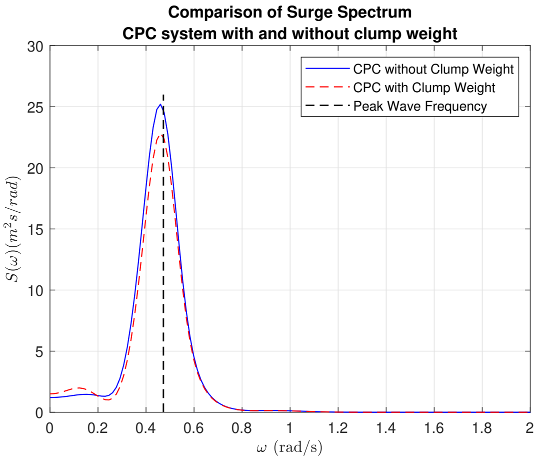

Figure 9.35: Power spectra of surge for CPC system with and without clump weights

From Figure 9.31, it can be seen that for pitch motion, the CNC system and chain system resulted in approximately the same MPM. The MPM of the CPC system with and without clump weight is lower compared to the other two systems. However, it can be seen that the variability along the y-axis is less for pitch, indicating that pitch is not highly influenced by changing the mooring system. Another important observation for pitch is shown in Figure 9.36.

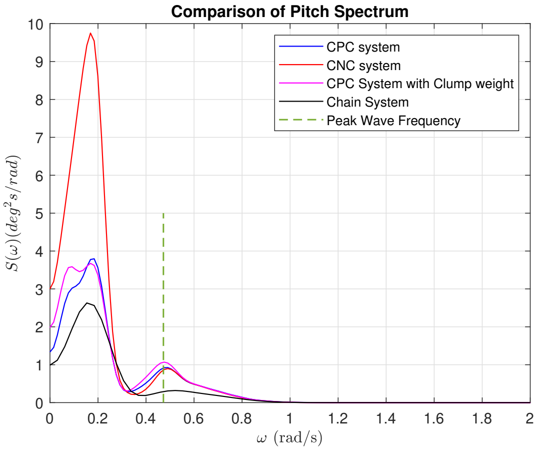

Figure 9.36: Power spectra of pitch for all mooring systems

From the figure, it can be observed that none of these mooring systems is excited by WF loads in pitch. However, from the spectra, it can be observed that the peak occurs at 0.19-0.2 rad/s for all the systems, which is close to the pitch natural frequency. Hence, irrespective of the mooring system, resonance in pitch DoF has to be expected for the FWT. This becomes a critical consideration while performing the FLS study.

Yaw Misalignment in Extreme Sea State

Figure 9.37 shows the yaw time series for the different mooring concepts in DLC 6.1.1 in-line collinear condition. The figure shows that irrespective of the mooring concept, the yaw misalignment is to be expected for FWT in an extreme sea state. The direction is random and could be either positive or negative, as explained in Section 4.3. However, looking at the absolute values, it can be observed that the pure chain system results in maximum yaw angle followed by the CNC system. CPC systems with and without clump weights are stiffer than the other two concepts, and hence the magnitude is less for these systems. It may also be noted that when the weather direction is in-between two mooring lines, this misalignment is not predominant as shown in Figure E.1.

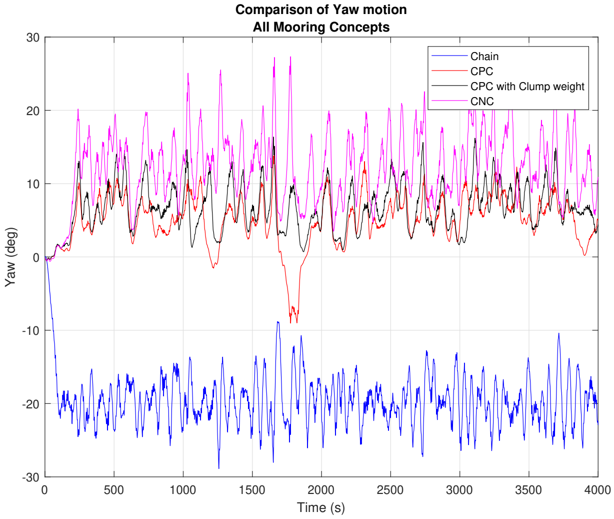

Figure 9.37: Comparison of yaw motion for all mooring concepts

Mooring Line Tension

Figure 9.38 shows the characteristic mean and dynamic tension multiplied with their respective safety factors for the different mooring systems. Table 9.4 shows the ULS criteria evaluation and the results for these concepts. The minimum MBL of the component in the mooring line is considered to determine the characteristic capacity for hybrid mooring systems.

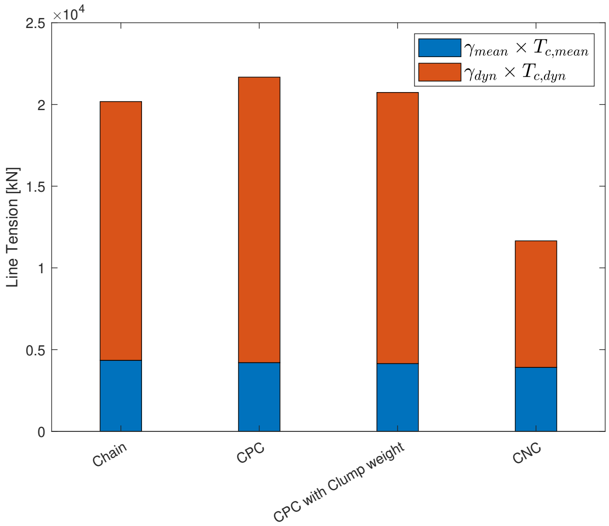

Figure 9.38: Comparison of line tension in the windward line for all mooring concepts

Table 9.4: ULS check of windward line for DLC 6.1.1 in-line collinear condition for all mooring concepts

Concept	DLC 6.1.1				
	$T_{c,mean}$ (kN)	$T_{c,dyn}$ (kN)	T_d (kN)	S_c (kN)	Status
Chain System	3342.57	9047.03	20177.64	22381.05	OK
CPC System	3234.17	9981.73	21672.45	22366.80	OK
CPC System with Clump weight	3189.36	9479.59	20735.45	22366.80	OK
CNC System	3010.20	4423.55	11654.47	15200.00	OK

From the Figure 9.38 it can be understood that the mean tension is unaffected by changing the mooring concepts. However, the dynamic tension varies. This is because the static forces acting on the FWT do not change w.r.t the mooring system, resulting in the same mean tension for all mooring concepts.

For the pure chain mooring concept, the stiffness of the mooring line is dominated by geometric stiffness. As the floating substructure offsets, the shape of the chain changes. As the floating substructure moves, the chain lifts off and settles down at the seabed, attracting large transverse drag loads resulting in dynamic tension in the mooring line. As shown in the power spectrum for the windward line in Figure 9.26 both LF wind gusts and WF loads significantly affect the line tension in the pure chain system.

From the Table 9.4 it can be seen that the dynamic tension increases by 10% for the CPC system compared to the pure chain system. This is because of two factors. First, the chain system studied in SIMO only provides quasi-static line tension. Therefore the dynamics are limited. Second, the CPC system includes stiff mooring lines, which attract larger WF loads and has higher dynamics and response than a pure chain system. This can also be seen from the time series and spectrum comparison shown in Figures 9.39 and 9.40.

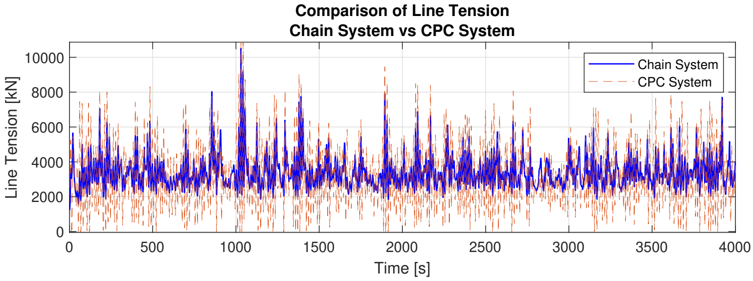

Figure 9.39: Time series comparison of line tension in the windward line for pure chain and CPC systems

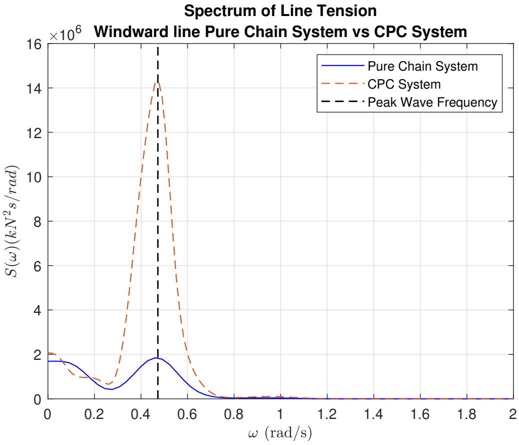

Figure 9.40: Comparison of the power spectrum of line tension in the windward line for pure chain and CPC systems

It can be observed from the spectrum comparison that for the CPC system, the LF contribution to line tension is in the same order as the pure chain system. However, it is not significant compared to WF contribution. The WF contribution is significantly higher for the CPC system, resulting in higher dynamic and design tension. As discussed in Section 4.2.1, WF motions can create cyclic tensions and fatigue damage accumulation in the mooring lines. Therefore, it is also necessary to perform the FLS study for the CPC system to understand its fatigue strength.

However, when the clump weights are introduced into the mooring lines of the CPC system, it can be observed that the dynamic tension reduces. Figures 9.41 and 9.42 shows the time series and power spectrum comparison of line tension in the windward line for the CPC system with and without clump weights.

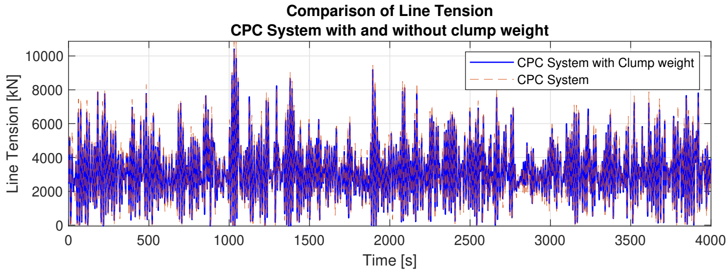

Figure 9.41: Time series comparison of line tension in the windward line for CPC systems with and without clump weights

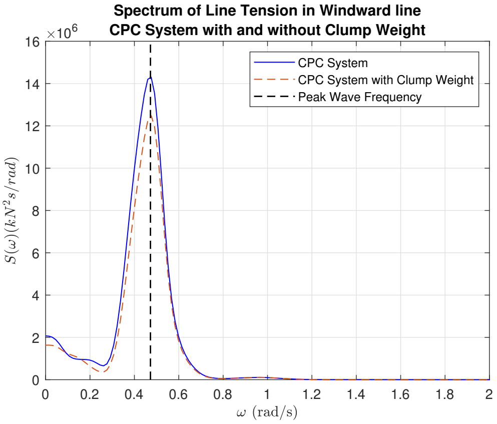

Figure 9.42: Power spectra comparison of line tension in the windward line for CPC systems with and without clump weights

From the above figures, it can be seen that by introducing clump weights into the mooring lines of the CPC system, the maximum tension can be reduced as the chain's geometric stiffness helps absorb the WF motion. Furthermore, when clump weights are introduced into the mooring system, the line characteristics of the mooring line is modified. Similar to the restoring curve shown in Figure 9.7, the typical line characteristic curve, which is linear, for a polyester line will have a slight catenary shape due to the clump weight. As a result, the horizontal tension in the mooring line for the CPC system with clump weights will be lower with the same dynamic offset.

When the CPC system with or without clump weight is compared to the CNC system, it can be seen that the dynamic tension is reduced by more than 50% for the CNC system. Figure 9.43 shows the time series comparison of the CPC system and CNC system.

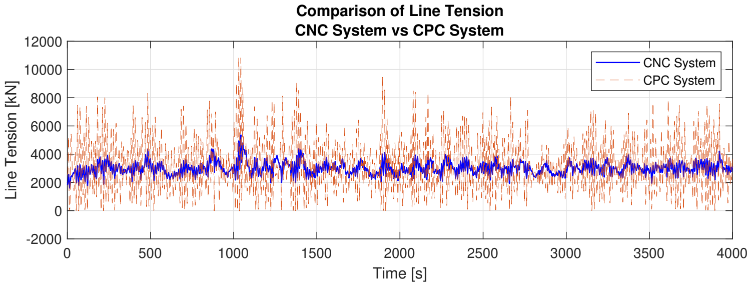

Figure 9.43: Time series comparison of line tension in the windward line for CPC and CNC systems

This reduction can be explained by treating the mooring lines as a spring. The elastic stiffness of the mooring line can then be estimated as EA/L, and the dynamic tension can then be calculated as follows:

$$T_{dyn} = \frac{EA}{L} \cdot x_{dyn} \quad \Rightarrow \quad T_{dyn} \propto EA$$

where x_{dyn} is the dynamic offset. The dynamic offset is due to the WF motion and will remain the same for all mooring concepts. As the mooring line length is constant, the dynamic tension is affected by axial stiffness, EA. The typical EA of nylon is lower than polyester [10]. Hence CNC system results in the lowest dynamic tension and, in turn, the lowest design tension compared to other concepts.

Slack Condition

In addition to the ULS check, it is also necessary to ensure that the mooring lines do not go into slack condition. This is especially relevant for hybrid mooring lines as the synthetic ropes have lower abrasion resistance, and if the lines go slack, they will rub against the seabed. The power production load cases are not critical as the offset is less, and from the time series it was observed that the mooring lines did not go into slack condition. However, the risk of lines becoming slack is higher for idling conditions. Figure 9.27 shows that for the pure chain system, mooring lines do not become slack during extreme sea states. Figures 9.44–9.46 shows the time series of windward and leeward line for other concepts in extreme sea state.

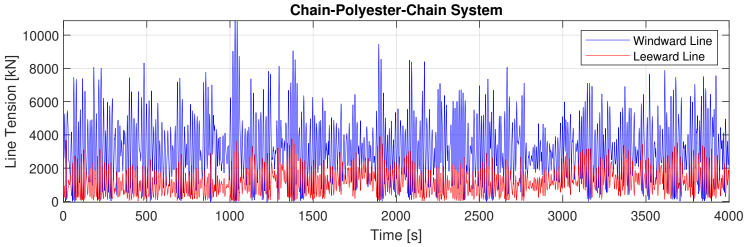

Figure 9.44: Time series comparison of line tension in the windward and leeward line for the CPC system

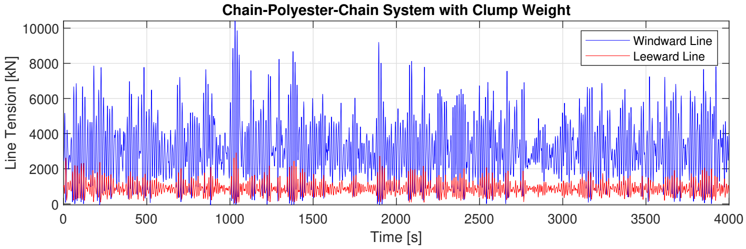

Figure 9.45: Time series comparison of line tension in the windward and leeward line for CPC system with Clump Weight

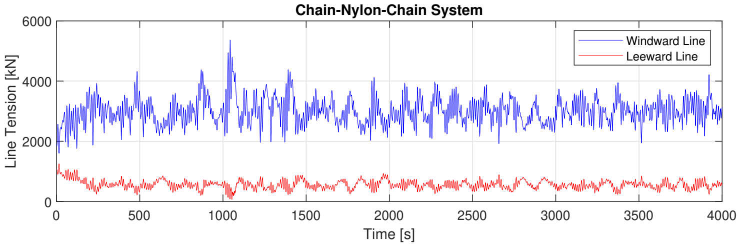

Figure 9.46: Time series comparison of line tension in the windward and leeward line for CNC system

From the figures, it can be seen that none of the mooring systems become fully slack in extreme sea states.

Chapter 10

Conclusion and Recommendations for Future Work

10.1 Summary and Conclusion

Deep-sea FWTs are gaining popularity as a viable option for generating sustainable energy, in line with the UN's goal of achieving a sustainable future. From the literature review, it has been seen that various types of FWT concepts are being developed for commercial deployment all around the world. Semi-submersibles, Tension Leg Platforms, Barges, and Spar buoys are examples of FWT designs with different substructures. Mainly two types of mooring systems are used to maintain the position of these FWTs. These are catenary and taut mooring systems, with the former being preferred more in shallower water depths and the latter being used more in deeper waters.

In this thesis, four different mooring concepts were analyzed for the 12MW INO WINDMOOR FWT concept with a semi-submersible substructure to be deployed off the coast of South Korea. These include a pure chain catenary mooring system and a hybrid mooring system consisting of chain and polyester segments with and without clump weights. Finally, the polyester segment was replaced with nylon without clump weights in the hybrid mooring system. ULS analysis of the intact mooring system was performed using different load cases. These include load cases corresponding to the rated condition of the turbine, cut-off condition of the turbine and idling condition at sea state corresponding to 50-year RP.

All numerical simulations were carried out in the SIMA software. The pure chain catenary mooring system was the base case in this thesis. It was analyzed using a SIMO model, and based on the results, a chain of R4S grade with 157 mm diameter was finalized for the base case mooring system. Furthermore, the pure chain catenary mooring system was also analyzed using a SIMO-RIFLEX coupled model to understand the effect of dynamic amplification. From the analysis, it was observed that the SIMO model underestimates the dynamics. The design tension was increased by 20% when analyzed using the coupled SIMO-RIFLEX model. From this, it shall be concluded that a quasi-static analysis is not sufficient as it underestimates mooring line dynamics and does not fully capture the effect due to drag on the mooring lines.

For the CPC mooring system, it was seen that as the system was very stiff compared to the pure chain catenary mooring system, the offsets were limited. The MPM in surge was reduced by 28%, indicating that this system is favourable when the aim is to reduce the offset to avoid power cable rupture. However, as the system was very stiff, the mooring line tensions were very high, and it was seen to be dominated by WF motions. As WF motions can cause cyclic tension and fatigue damage accumulation in mooring lines, an FLS study has to be performed for this system. A slightly longer mooring line can also be used to decrease the elastic stiffness and thereby the dynamic tension for the CPC system.

The CPC system with clump weights showed a positive effect on the design tension of the mooring line. The clump weight contributed to the geometric stiffness of the mooring line and helped to absorb the WF motion. As a result, design tension was reduced by approximately 5% compared to the system without clump weight. However, the offset of the platform was moderately increased as the system was softer than the CPC system without clump weight. Nevertheless, this was lesser than the base case mooring system, indicating that this system can be implemented for the FWT.

A significant advantage of replacing the polyester segment with nylon in the hybrid mooring system was that the design tension was reduced by more than 50%. This was due to nylon's property, which has a lower axial stiffness than polyester. However, the downside of the CNC system was that the offsets increased considerably. It was seen that the MPM in surge was more than the base case mooring system. Hence, the risk of power cable rupture or collision with a nearby wind turbine in an FWT farm is high for this system.

Furthermore, if the extent of yaw misalignment in extreme sea state is considered, it has been observed that the CPC system with and without clump weight resulted in the lowest yaw angle compared to all four systems. Therefore, considering all these aspects, it can be stated that either the CPC system with clump weight or the CPC system with a slightly longer mooring line and no clump weight can be considered a viable alternative for the FWT mooring system in deep waters off the coast of South Korea.

10.2 Recommendations for Future Work

The primary focus of this thesis work was to understand the concepts of station-keeping principles and evaluate various mooring concepts through a time-domain analysis for 100 m water depth off the coast of South Korea. Based on the ULS analysis, a hybrid mooring line with chain and polyester segments, either with or without clump weights, can be considered a feasible option. However, it is also necessary to perform the FLS study to understand the fatigue capacity of the mooring lines fully. This is important because the CPC system is dominated by WF motion which can cause cyclic tension and fatigue accumulation in the mooring lines. Furthermore, as seen in Chapter 9, irrespective of the mooring system, a pitch resonance is observed for the FWT. Therefore, it is critical to understand the effect of pitch resonance on the FLS capacity of the mooring lines.

To use nylon instead of polyester in a hybrid mooring system, further study has to be performed to design the power cables such that they can absorb the excessive surge motion of the platform. Similarly, the fatigue capacity of nylon is not fully known and further studies shall be performed to understand the same.

Furthermore, when performing the detailed analysis for mooring system, the effect of marine growth on the mooring lines shall also be considered. In the ULS analysis consequence class 1 is considered for the mooring system. This implies that the structure shall not drift away even if there is a mooring line failure. Therefore, it is also essential that an ALS analysis be performed to validate this assumption.

The ULS analysis for the synthetic rope systems is carried out using the simulation set-up and procedure for the fibre rope model provided by supervisor Kjell Larsen. Based on this procedure, the initial static offset and mean dynamic offset should correspond well with each other. However, it was observed that a significant difference was present, especially for the CNC system. As a result, the mean non-linear static tension determined from the static analysis will be slightly underestimated. Therefore, it is important to develop this simulation procedure further for future analysis.

Bibliography

[1] Bachynski-Polić E, Gao Z. *TMR03 Integrated dynamic analysis of wind turbines. Lecture Notes - Introduction to offshore wind power and technology*. NTNU, 2019.

[2] Equinor. *Axial Stiffness of Synthetic Mooring Lines - Engineering Models*. Equinor, June, 2021.

[3] DNVGL. *DNVGL-ST-0119 Floating Wind Turbine Structures*. DNVGL, July, 2018.

[4] DNVGL. *DNVGL-ST-0437 Loads and site conditions for wind turbines*. DNVGL, November, 2016.

[5] Souza, C E et al. *Definition of the INO WINDMOOR 12 MW base case floating wind turbine*. 2021, doi:10.13140/RG.2.2.32947.25121.

[6] DNV. Energy transition outlook 2021. *Technical Report*, DNV 2021.

[7] Wind EUROPE. *Offshore Wind in Europe - Key Trends and Statistics 2019*. windeurope.org, 2020.

[8] James R, Ros MC. Floating offshore wind: Market and technology review. prepared for the scottish government. *Technical Report*, Carbon Trust 2015.

[9] Wind EUROPE. *Ports: a key enabler for the floating offshore wind sector*. windeurope.org, 2020.

[10] Larsen K. *TMR4225 Marine Operations. Lecture Notes #8 - Station Keeping and Mooring of Floating Structures*. NTNU, 2020.

[11] Ma, K T et al. *Mooring system engineering for offshore structures*. 2 edn., Eslevier : Gulf Professional Publishing: Cambridge, Massachusetts, 2019.

[12] Greco M. *TMR 4215: Sea Loads Lecture Notes*. NTNU, 2019.

[13] Bachynski-Polić E. *TMR03 Integrated dynamic analysis of wind turbines. Lecture Notes - Basic Aerodynamics for Wind Turbines*. NTNU, 2021.

[14] SINTEF Ocean. *SIMO 4.20.2 User Guide*. SINTEF Ocean, 2021.

[15] SINTEF Ocean. *RIFLEX 4.20.2 User Guide*. SINTEF Ocean, 2021.

[16] Equinor. *Time Domain Analysis Overview*. Equinor, 2021.

[17] Statoil. *Characteristic value of «Design Limit»*. Statoil, 2016.

[18] DNVGL. *DNVGL-RP-C205 Environmental conditions and environmental loads*. DNVGL, December, 2019.

[19] Equinor. *DONGHAE South Korea – Metocean data summary*. Equinor, 2020.

[20] Ramakrishnan, K S M. *TMR4520 Specialization Project. Design and Numerical Analysis of Mooring Systems for Floating Wind Turbine*. Norwegian University of Science and Technology (NTNU), 2021.

[21] UN Sustainable Development Goals. `https://www.un.org/sustainabledevelopment/energy/`. Accessed: 2021-09-02.

[22] Stewart G, Muskulus M. A review and comparison of floating offshore wind turbine model experiments. *Energy Procedia* 09 2016; **94**:227–231, doi:10.1016/j.egypro.2016.09.228.

[23] Huera-Huarte F. *Deep Water: The next step for offshore wind energy. A report by the European Wind Energy Association*. 2013.

[24] Chakrabarti SK. *Handbook of offshore engineering*, vol. II. Elsevier, 2005.

[25] Nadim, F et al. Reliability-based design of suction anchor foundation for floating platforms. 2017.

[26] Windfloat atlantic floating wind turbine moorings. `https://www.lankhorstoffshore.com/about-us/news-events/windfloat-atlantic-floating-wind-turbine-moorings`. Accessed: 2022-01-18.

[27] Faltinsen OM. *Sea Loads on Ships and Offshore Structures*. Cambridge University Press, 1990.

[28] Weller, S et al. Synthetic mooring ropes for marine renewable energy applications. *Renewable Energy* 11 2015; **83**:1268–1278, doi:10.1016/j.renene.2015.03.058.

[29] DNVGL. *SYROPE JIP. Best practice for analysis of mooring systems with polyester ropes*. DNV GL AS Oil & Gas, 2015.

[30] IEC 61400. `https://en.wikipedia.org/wiki/IEC_61400`. Accessed: 2022-03-19.

[31] DNV. *DNV-ST-0119 Floating Wind Turbine Structures*. DNV, June, 2021.

[32] Larsen, C M et al. *TMR4182 Marine Dynamics Compendium*. NTNU, 2019.

[33] Feizolahzadeh, M et al. Wind load response of offshore wind turbine towers with fixed monopile platform. *Journal of Wind Engineering and Industrial Aerodynamics* 11 2016; **158**:122–138, doi:10.1016/j.jweia.2016.09.007.

[34] Dev A. Viscous effects in drift forces on semi-submersibles. PhD Thesis 10 1996.

[35] Larsen T, Hanson T. A method to avoid negative damped low frequent tower vibrations for a floating, pitch controlled wind turbine. *Journal of Physics: Conference Series* 08 2007; **75**:012 073, doi:10.1088/1742-6596/75/1/012073.

[36] Haslum HA, Faltinsen OM. Alternative Shape of Spar Platforms for Use in Hostile Areas. 05 1999; doi:10.4043/10953-MS. URL `https://doi.org/10.4043/10953-MS`, oTC-10953-MS.

[37] Koo B, Kim M, Randall R. Mathieu instability of a spar platform with mooring and risers. *Ocean Engineering* 2004; **31**(17):2175–2208, doi:https://doi.org/10.1016/j.oceaneng.2004.04.005. URL `https://www.sciencedirect.com/science/article/pii/S0029801804000964`.

[38] Haslum, H et al. Aerodynamic roll-yaw instabilities of floating offshore wind turbines. 2020, doi:10.1115/OMAE2020-18273.

[39] SIMA. `https://www.sintef.no/en/software/sima/`. Accessed: 2022-04-18.

[40] Gao Z. *TMR03 Integrated Dynamic Analysis of Wind Turbines. Additional lecture notes – Time domain equations of motions*. NTNU, 2021.

[41] SINTEF Ocean. *SIMO 4.20.2 Theory Manual*. SINTEF Ocean, 2021.

[42] SINTEF Ocean. *RIFLEX 4.20.2 Theory Manual*. SINTEF Ocean, 2021.

[43] DNV. *Offshore Standard DNV-OS-E301 Position Mooring*. DNV, October, 2013.

[44] Advanced wave and wind load models for floating wind turbine mooring system design. `https://www.sintef.no/projectweb/windmoor/`. Accessed: 2021-12-03.

[45] Top quality mooring products for harsh offshore conditions. `https://ramnas.com/wp-content/uploads/2012/11/Ramnas-Technical-Broschure.pdf`. Accessed: 2021-12-03.

[46] Bridon. *Oil and Gas. Wire and fibre rope solutions for the world's most demanding applications*. 6 edn., Bridon, 2013.

[47] Yuan Z, Incecik A, Ji C. Numerical study on a hybrid mooring system with clump weights and buoys. *Ocean Engineering* 09 2014; **88**:1–11, doi:10.1016/j.oceaneng.2014.06.002.

[48] Bruschi, N et al. Influence of clumps-weighted moorings on a spar buoy offshore wind turbine. *Energies* 12 2020; **13**:6407, doi:10.3390/en13236407.

[49] wafo-project. `https://github.com/wafo-project/wafo/blob/master/wafo/onedim/dat2spec.m`. Accessed: 2022-05-27.

Appendices

Appendix A

First-Order Wave Force Transfer Functions

The first-order wave force transfer function in the 6 DoFs for different wave headings are estimated in WAMIT and is included in the SIMA model. The transfer functions for Surge, Sway, Heave, Roll, Pitch and Yaw at wave headings, $\beta = 0°$, $45°$, $90°$ are shown in Figures A.1–A.6 respectively.

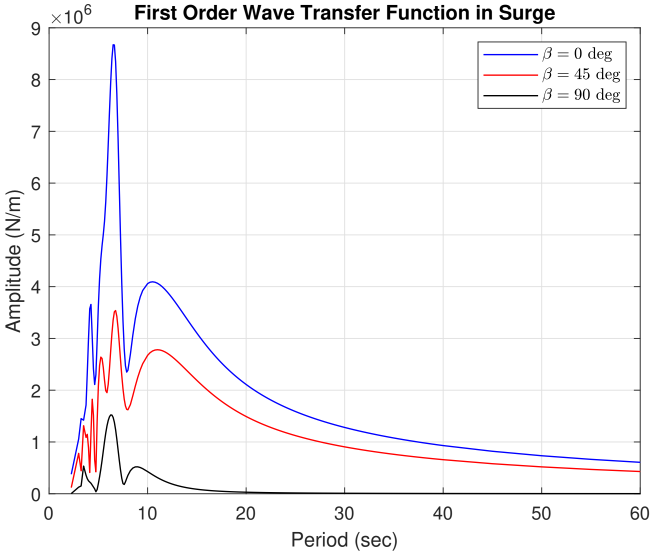

Figure A.1: First-order wave force transfer function in Surge

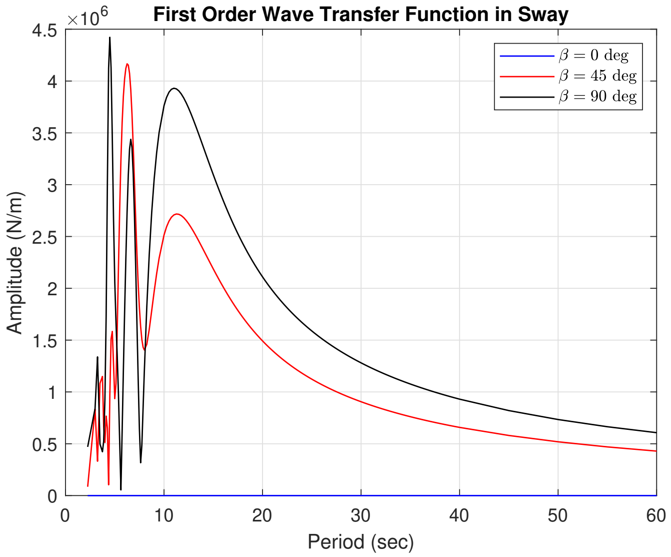

Figure A.2: First-order wave force transfer function in Sway

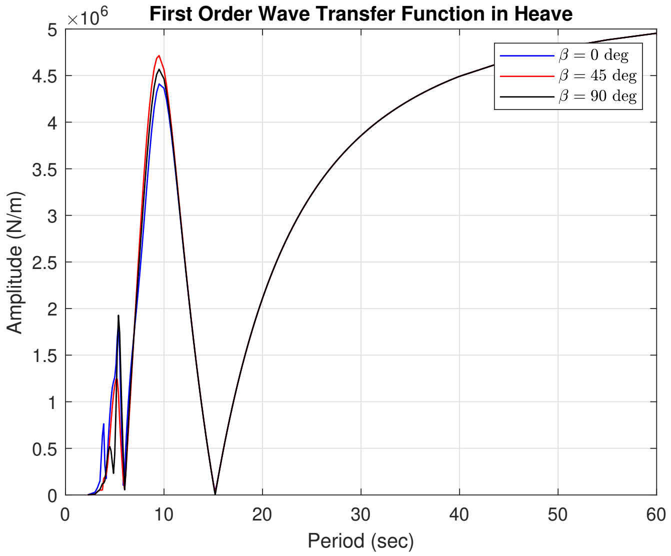

Figure A.3: First-order wave force transfer function in Heave

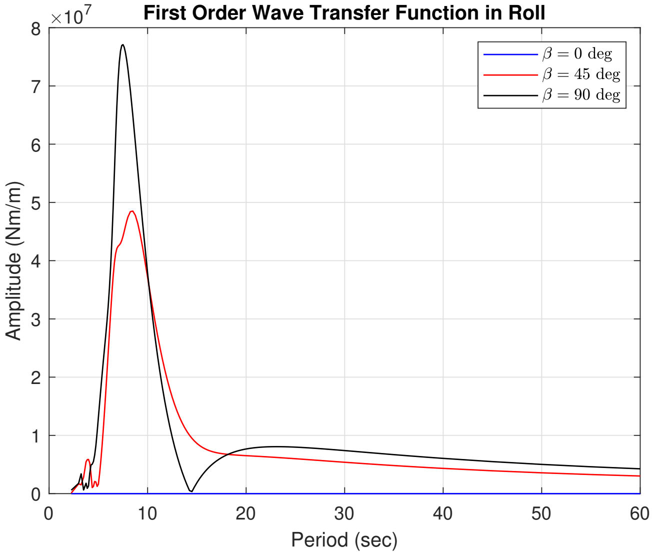

Figure A.4: First-order wave force transfer function in Roll

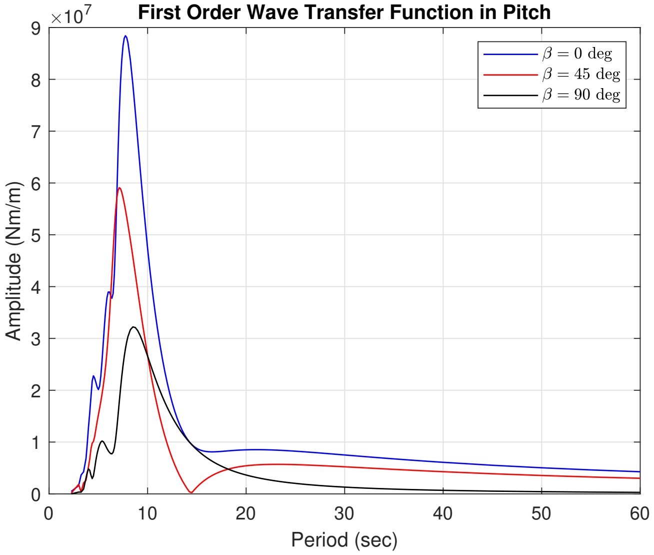

Figure A.5: First-order wave force transfer function in Pitch

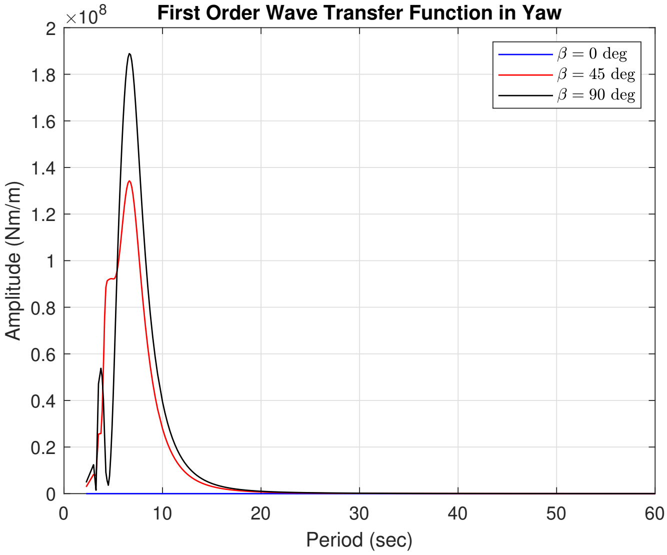

Figure A.6: First-order wave force transfer function in Yaw

From Figures A.1 and A.5, it can be observed that the maximum force in surge will be experienced by the structure in head sea condition with 0° wave heading. For quartering sea and beam sea conditions at wave headings 45° and 90° respectively, the amplitude of force decreases.

Similarly from Figures A.2, A.4 and A.6, it can be observed that for Sway, Roll and Yaw DoF, the maximum force will be experienced by the structure in beam sea condition with 90° wave heading. In head sea condition, the structure will not experience any force in these DoFs.

In Heave, the maximum force will be experienced during the head sea condition and will reduce as the wave heading changes and goes to beam sea condition. However, the extent of change is less compared to Surge or Pitch DoFs.

Appendix B

Response Amplitude Operators

The RAO in the 6 DoFs for different wave headings are estimated in WAMIT and is included in the SIMA model. The motion transfer functions for Surge, Sway, Heave, Roll, Pitch and Yaw at wave headings, $\beta = 0°, 45°, 90°$ are shown in Figures B.1–B.6 respectively.

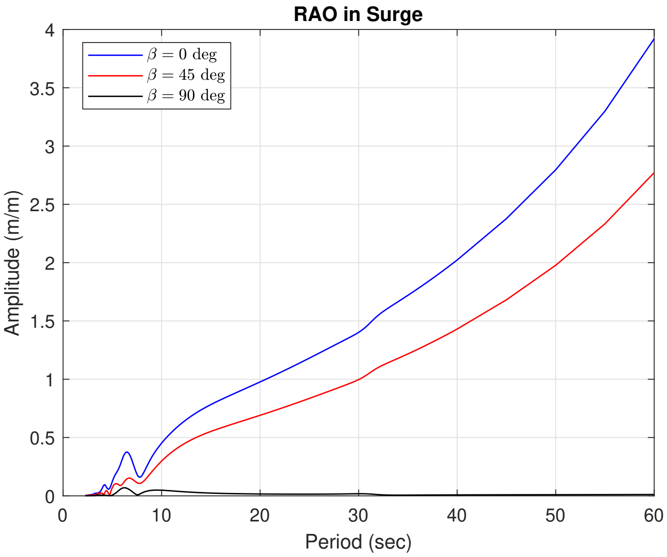

Figure B.1: RAO in Surge

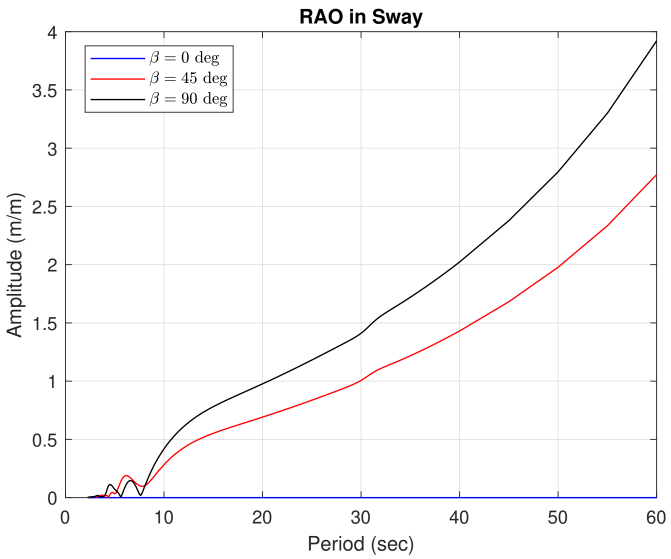

Figure B.2: RAO in Sway

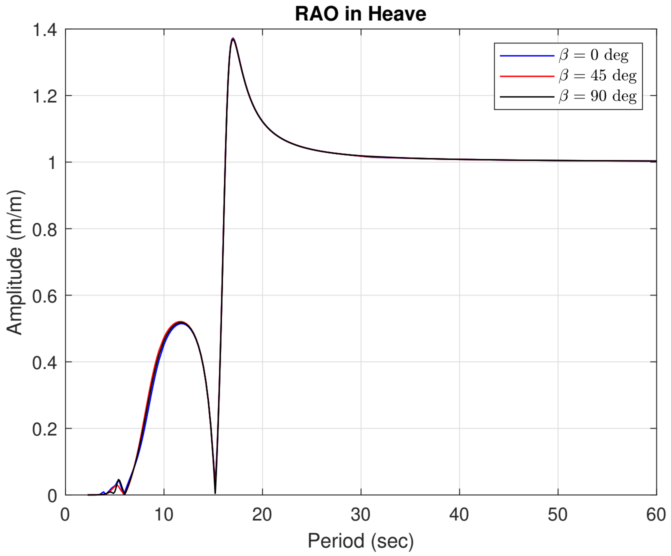

Figure B.3: RAO in Heave

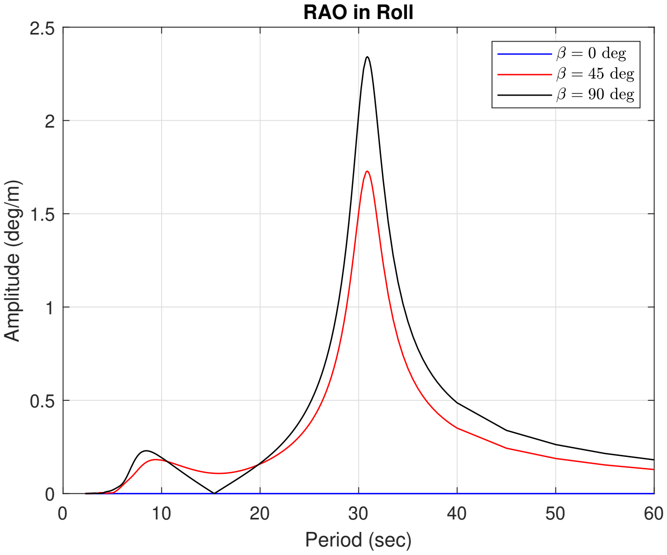

Figure B.4: RAO in Roll

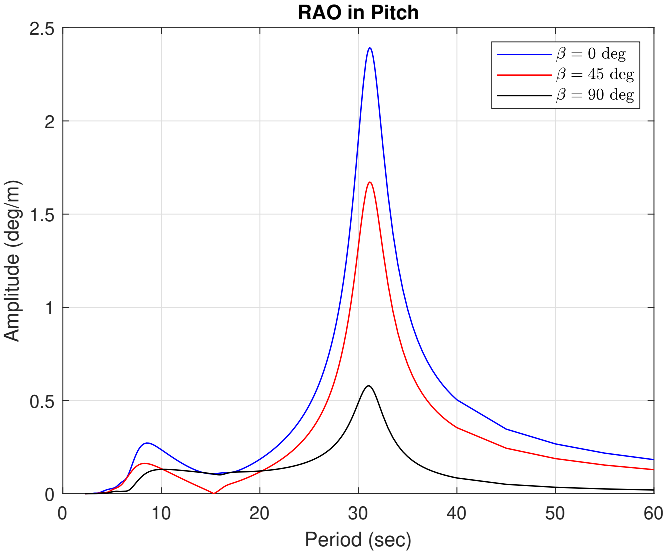

Figure B.5: RAO in Pitch

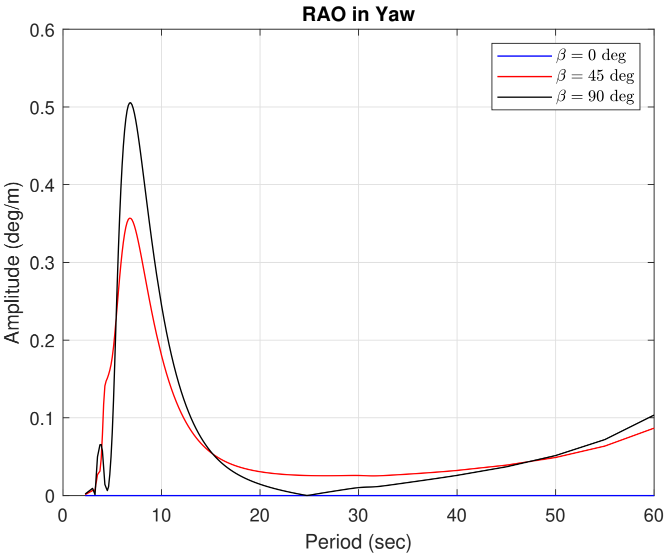

Figure B.6: RAO in Yaw

Appendix C

Comparison of Constant Wind Test from SIMA and OpenFAST

Figure C.1 shows the comparison of constant wind test results obtained from SIMA with results obtained in OpenFAST.

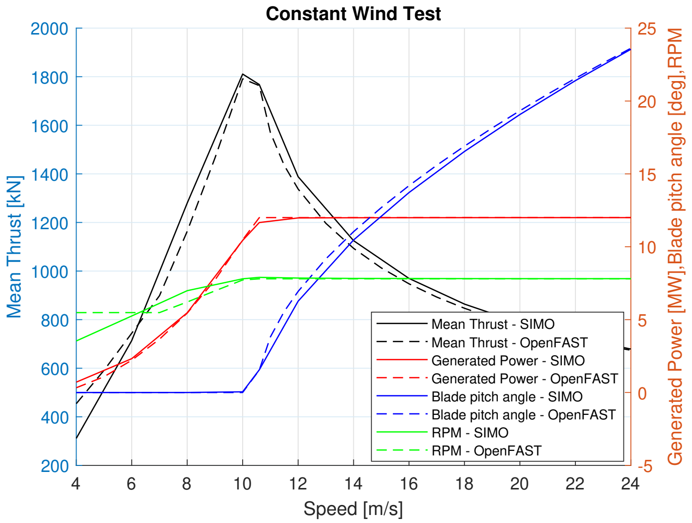

Figure C.1: Constant wind test result comparison with OpenFAST result for INO WINDMOOR 12 MW turbine

Appendix D

Decay Test Plots

The free decay plot in all 6 DoFs with turning points for various mooring systems are shown in Figures D.1–D.6.

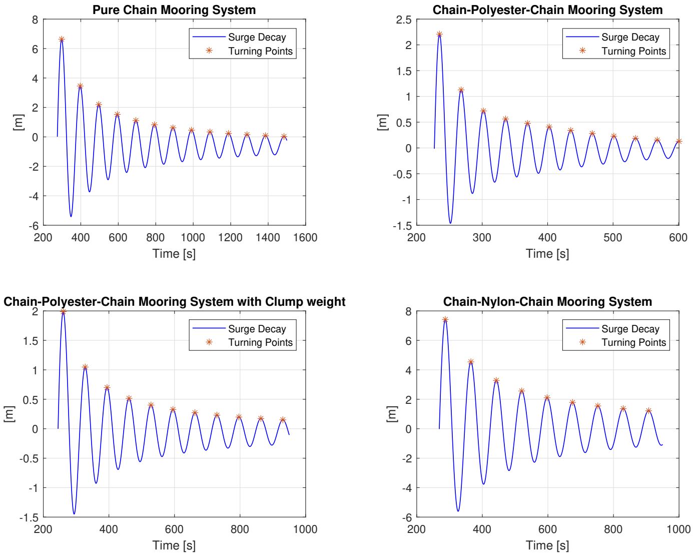

Figure D.1: Surge Decay with Turning Points

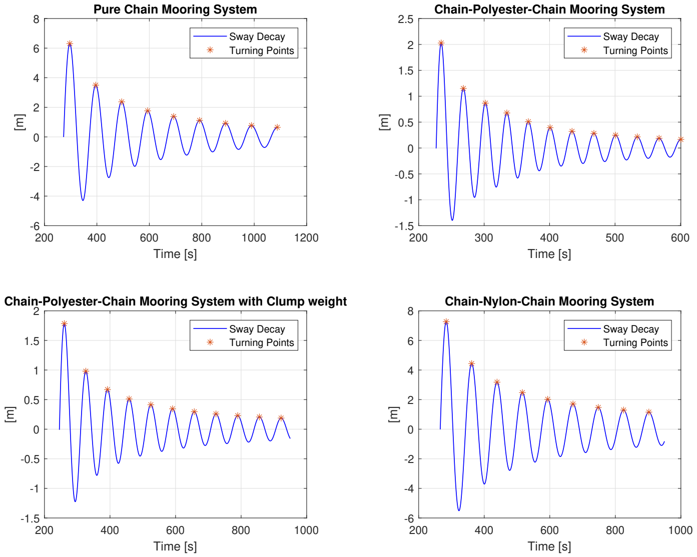

Figure D.2: Sway Decay with Turning Points

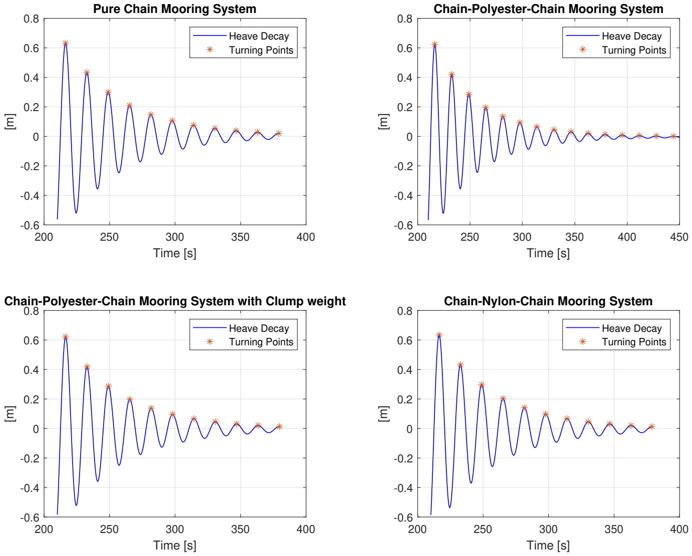

Figure D.3: Heave Decay with Turning Points

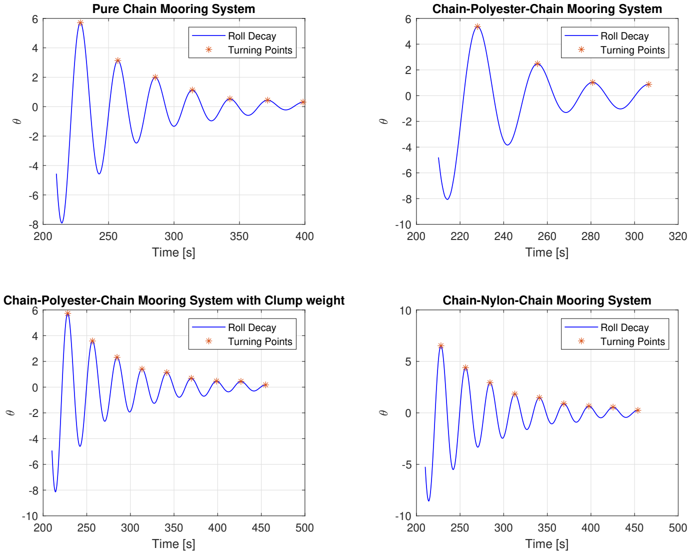

Figure D.4: Roll Decay with Turning Points

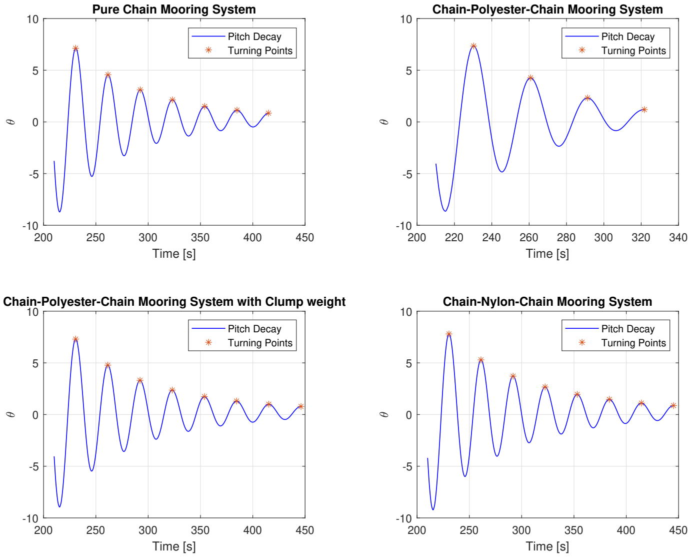

Figure D.5: Pitch Decay with Turning Points

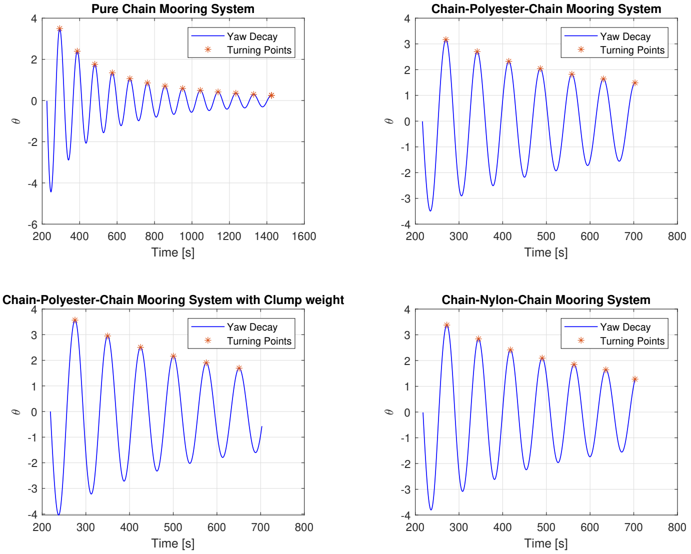

Figure D.6: Yaw Decay with Turning Points

Appendix E

Results for DLC 6.1.1 in In-between Collinear Condition

Table E.1 shows the line tension in the leeward line for DLC 6.1.1 in the in-between collinear condition.

Table E.1: ULS check of leeward line for DLC 6.1.1 in-between collinear condition for all mooring concepts

Concept	DLC 1.6				
	$T_{c,mean}$ (kN)	$T_{c,dyn}$ (kN)	T_d (kN)	S_c (kN)	Status
Chain System	677.49	817.73	2311.76	22381.05	OK
CPC System	570.02	3813.13	7414.00	22366.80	OK
CPC System with Clump weight	696.89	2435.46	5168.00	22366.80	OK
CNC System	196.22	685.05	1453.92	15200.00	OK

From Table E.1, it can be observed that dynamic tension and thus the design tension is the highest for the CPC system, similar to the in-line collinear condition. The CNC system has the lowest dynamic and design tension among all the concepts.

Furthermore, when the mean and MPM in surge is compared in the in-line and in-between condition, it is seen that the values are higher in the in-between direction compared to in-line direction, similar to the restoring curves shown in Figures 9.7 and 9.8. However, it is observed that when the weather is acting in the in-between direction, the yaw misalignment is not predominant as shown in the below figure.

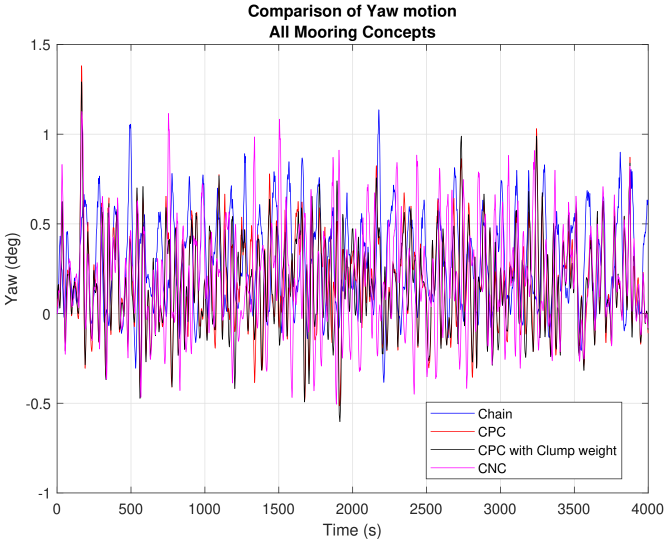

Figure E.1: Yaw Time Series Comparison DLC 6.1.1 In-between collinear Condition

From the figure it can be seen that the mean offset is around 0 m for all mooring concepts.

Appendix F

Results for DLC 1.6

The response of the FWT in surge, heave and pitch and the line tension in ML 1 for DLC 1.6 is presented below.

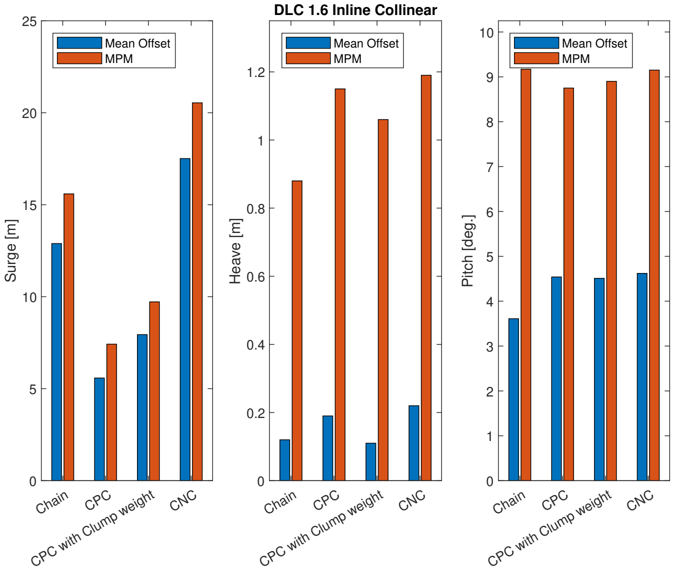

Figure F.1: DLC 1.6 In-line collinear motions

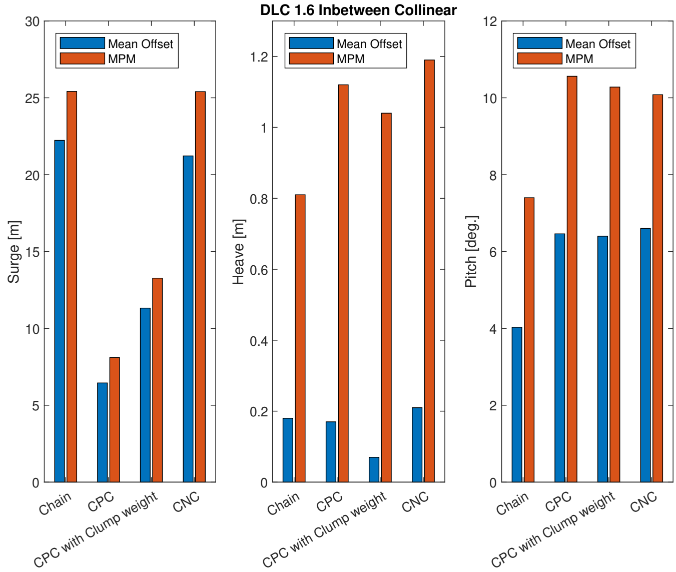

Figure F.2: DLC 1.6 In-between collinear motions

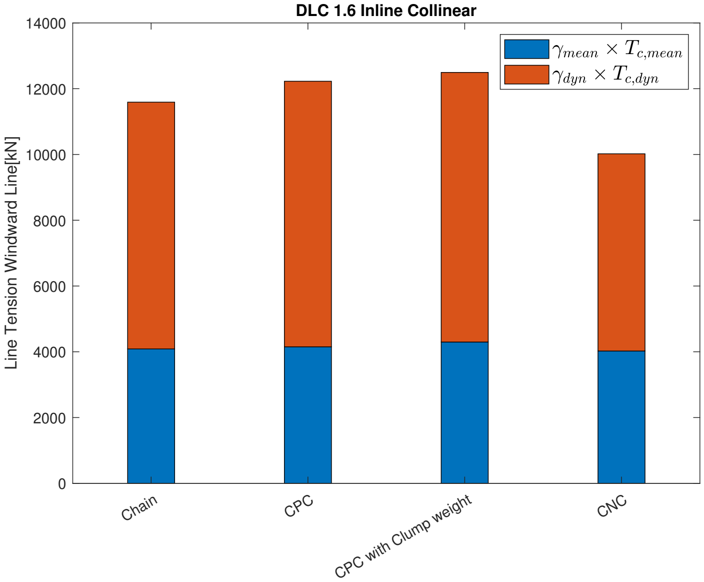

Figure F.3: DLC 1.6 In-line collinear tension

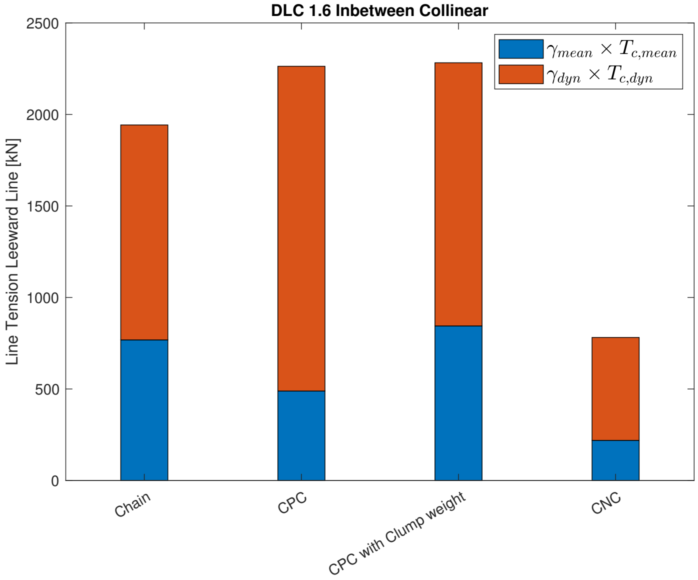

Figure F.4: DLC 1.6 In-between collinear tension

Table F.1: ULS check of windward line for DLC 1.6 in-line collinear condition for all mooring concepts

Concept	DLC 1.6 In-line Collinear				
	$T_{c,mean}$ (kN)	$T_{c,dyn}$ (kN)	T_d (kN)	S_c (kN)	Status
Chain System	3143.24	4288.14	11590.41	22381.05	OK
CPC System	3192.29	4614.92	12226.09	22366.80	OK
CPC System with Clump weight	3305.21	4684.07	12493.90	22366.80	OK
CNC System	3095.16	3426.41	10019.25	15200.00	OK

Table F.2: ULS check of leeward line for DLC 1.6 in-between collinear condition for all mooring concepts

Concept	DLC 1.6 In-between Collinear				
	$T_{c,mean}$ (kN)	$T_{c,dyn}$ (kN)	T_d (kN)	S_c (kN)	Status
Chain System	590.96	670.99	1942.48	22381.05	OK
CPC System	376.09	1013.80	2263.07	22366.80	OK
CPC System with Clump weight	649.69	821.50	2282.22	22366.80	OK
CNC System	168.70	321.21	781.42	15200.00	OK

Appendix G

Results for DLC 1.1

The response of the FWT in surge, heave and pitch and the line tension in ML 1 for DLC 1.1 is presented below.

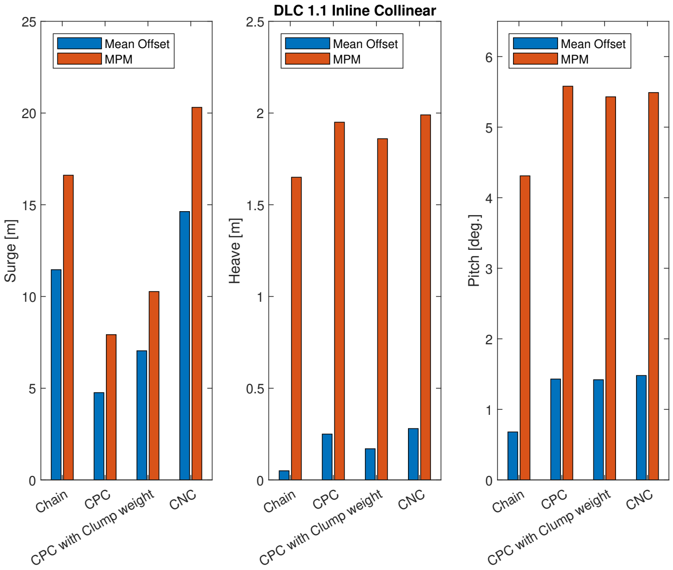

Figure G.1: DLC 1.1 In-line collinear motions

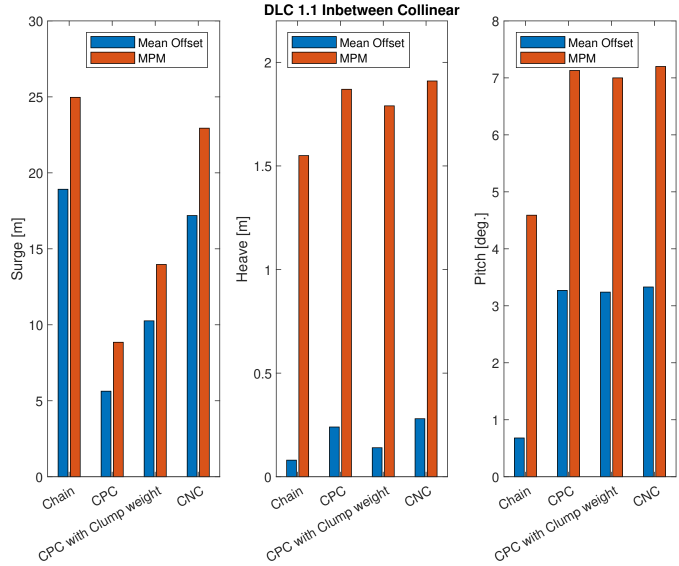

Figure G.2: DLC 1.1 In-between collinear motions

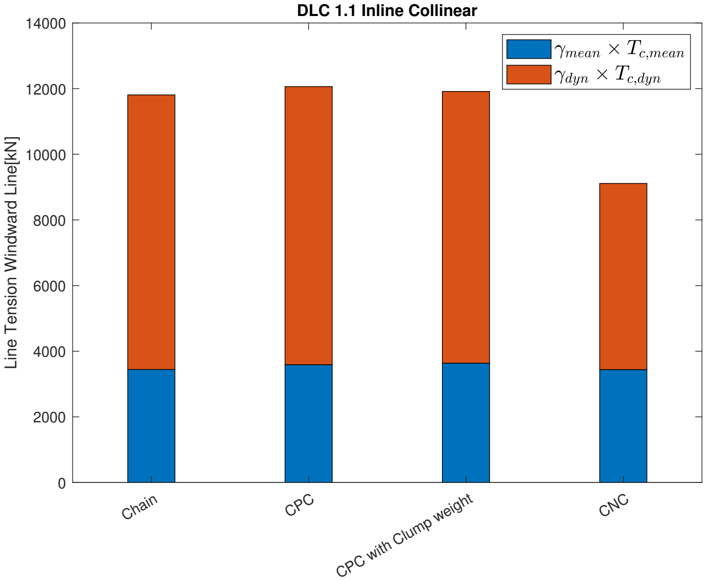

Figure G.3: DLC 1.1 In-line collinear tension

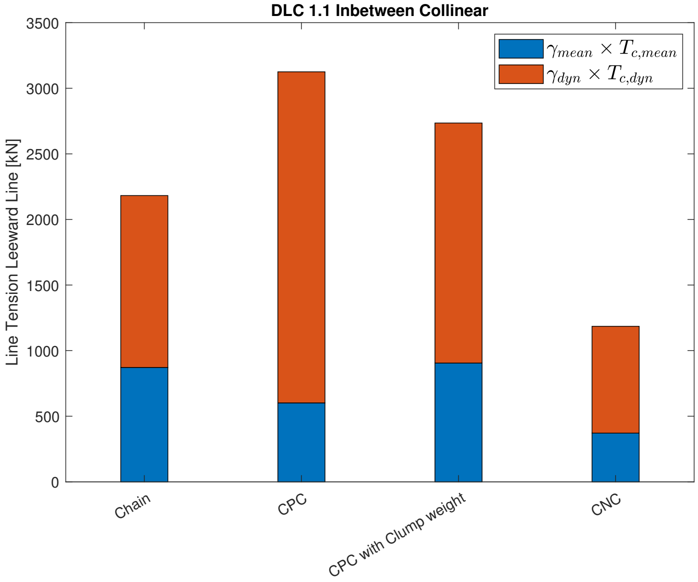

Figure G.4: DLC 1.1 In-between collinear tension

Table G.1: ULS check of windward line for DLC 1.1 in-line collinear condition for all mooring concepts

Concept	DLC 1.1 In-line Collinear				
	$T_{c,mean}$ (kN)	$T_{c,dyn}$ (kN)	T_d (kN)	S_c (kN)	Status
Chain System	2648.70	4780.61	11809.38	22381.05	OK
CPC System	2671.42	4841.33	12062.18	22366.80	OK
CPC System with Clump weight	2797.53	4729.76	11913.88	22366.80	OK
CNC System	2645.68	3241.38	9111.80	15200.00	OK

Table G.2: ULS check of leeward line for DLC 1.1 in-between collinear condition for all mooring concepts

Concept	DLC 1.1 In-between Collinear				
	$T_{c,mean}$ (kN)	$T_{c,dyn}$ (kN)	T_d (kN)	S_c (kN)	Status
Chain System	670.47	748.88	2182.15	22381.05	OK
CPC System	462.84	1442.20	3125.54	22366.80	OK
CPC System with Clump weight	696.41	1045.54	2735.04	22366.80	OK
CNC System	285.52	465.32	1185.49	15200.00	OK

Kaushik Shiva Manjeri Ramakrishnan

Numerical Analysis of Mooring Systems for Floating Wind Turbines

NTNU
Norwegian University of
Science and Technology